



NTNU – Trondheim
Norwegian University of
Science and Technology

Cross-linking oxidized cellulose nanofibrils for the formation of stable hydrogel structures

Sigurd Rolland Pettersen

Nanotechnology

Submission date: June 2013

Supervisor: Kristin Syverud, IKP

Co-supervisor: Gary Chinga Carrasco, Papir- og fiberinstituttet AS (PFI)

Norwegian University of Science and Technology
Department of Chemical Engineering

Acknowledgements

The work in this master's thesis has been carried out over a total period of 21 weeks; from January 20 to June 16, 2013. It has been a laborious period, with many hours spent in the lab and in front of the computer. For me, this has been rewarded with many interesting experiences and a deeper understanding of many of the topics dealt with in this thesis.

I wish to express my gratitude to my supervisor Professor Il Kristin Syverud (Department of Chemical Engineering, NTNU/PFI) for giving me much freedom to choose the means of approaching the various problems that had to be investigated and overcome during this project, while still being there with good advice and much patience when needed. I also wish to thank my co-supervisor Gary Chinga-Carrasco (PFI) for sharing his knowledge on a range of characterization techniques, and for conducting the residual fiber measurement. Professor Kurt Ingar Draget and PhD Magnus Nergård Hattrem at the Department of Biotechnology, NTNU, is acknowledged for making available both their expertise on rheology and the equipment needed for carrying out large parts of this project. The engineers and staff at PFI is recognized for conducting the TEMPO-mediated oxidation and fibrillation of the MFC used in this project, and for being very pleasant and helpful with training and questions on the daily lab routine. NTNU NanoLab is acknowledged for providing training on and making available the AFM and S(T)EM used in this study. At last, I wish to thank Silje Nedland Molnes for all the love she has given me, and for interesting discussions and feedback on many of the topics in this thesis.

I declare that this is an independent work according to the exam regulations of the Norwegian University of Science and Technology (NTNU).

Sigurd Rolland Pettersen
MTNANO

Sammendrag

Hovedmålet med denne oppgaven var å undersøke om de elastiske egenskapene til suspensjoner av mikrofibrillert cellulose (MFC) forbehandlet med TEMPO-mediert oksidering kunne kontrolleres ved å indusere kryssbindinger av korte diaminer mellom nanofibrillene. Det totale karboksylsyre- og aldehydinnholdet i MFC-prøven ble målt til henholdsvis 0,810 mmol/g MFC og 0,181 mmol/g MFC gjennom konduktimetrisk titrering.

De viskoelastiske egenskapene til MFC-prøven ble undersøkt med dynamiske reologiske målinger. MFC-prøven viste en viskoelastisk respons for deformasjoner $< 0,04$, og gel-aktig oppførsel ($G' > G''$, δ konstant og $< 45^\circ$) for frekvenser fra 0.01 – 10 Hz. Lagringsmodulen for 0,80% MFC var ca. 125 Pa, og lagringsmodulen viste en eksponensiell avhengighet av konsentrasjon med en potens på omtrent tre. Viskositetsmålinger viste at MFC utviser skjærtynnende egenskaper. Viskositeten fulgte ikke Cox-Merz regelen, da den dynamiske viskositeten var omtrent ti ganger høyere enn den vanlige viskositeten når $\omega = \dot{\gamma}$. Når heksametylendiamin (HMDA) ble tilsatt systemet uten oppvarming, sank både lagringsmodulen og viskositeten. Når temperaturen ble økt til 80° C, økte lagringsmodulen 11 ganger i en prøve med 0,80% MFC og 3,05 mmol HMDA/g MFC.

Små, sylindrerformede geler ble støpt med en konsentrasjon på 0,80% MFC med varierende konsentrasjoner av HMDA og etylendiamin (EDA) ved 80° C. Youngs modul ble målt med kompresjonsmålinger, og korrellerte godt med økende konsentrasjon av kryssbindere fram til en platåverdi ble oppnådd ved omtrent tretti ganger mer amin enn aldehyd. Gelene med HMDA var omtrent dobbelt så sterke som gelene med EDA. Høyest Youngs modul (ca. 3220 Pa) ble målt for gelene med 3,05 mmol HMDA/g MFC. Det var en tydelig fargeforandring fra den gråaktige utgangsfargen til en gul-brun farge. Denne korrellerte godt med både stigende kryssbinderkonsentrasjon og den målte Youngs modulen. Når det atoksiske reduksjonsmiddelet 2-picoline-borane ble tilsatt gelene før støpingen, oppstod den ingen fargeforandring, men Youngs modul oppnådde nesten de samme verdiene.

Noen av de støpte gelene ble frysetørket, og en flakete porestruktur ble observert i disse ved skanningelektronmikroskop (SEM) avbildning. De frysetørkede gelene viste vannabsorpsjonsverdier på omtrent 8000% for de rene MFC-gelene og omtrent 4000% for gelene med HMDA.

Filmer ble også tillaget, både av ren MFC og med kryssbinderkonsentrasjoner tilsvarende gelene. Disse filmene ble avbildet med laser profilometer (LP) og atomært kraftmikroskop (AFM), og bildene ble analysert for en korrelasjon mellom overflateruhet og kryssbinderkonsentrasjon. Ingen signifikant korrelasjon kunne observeres fra AFM-bildene, men LP-bildene viste høyere overflateruhet ved de høyeste kryssbinderkonsentrasjonene.

Abstract

The main goal of this project was to investigate whether the elastic properties of microfibrillated cellulose (MFC) suspensions pre-treated by TEMPO-mediated oxidation could be controlled by inducing crosslinks between the nanofibrils with short diamines. Using conductometric titration, the total carboxylate and aldehyde content in the MFC was measured as 0.810 mmol/g MFC and 0.181 mmol/g MFC, respectively.

The viscoelastic properties of the MFC were investigated by dynamic measurements. The MFC showed a viscoelastic response for strains approximately < 0.04 , and gel-like behavior ($G' > G''$, δ constant and $< 45^\circ$) for frequencies from 0.01 – 10 Hz. The storage modulus for 0.80% MFC was approximately 125 Pa, and the storage modulus showed a power law dependence on concentration with a power of approximately three. Viscosity measurements showed that the MFC exhibited pseudoplastic (shear-thinning) behavior. The viscosity did not follow the Cox-Merz rule, with the dynamic viscosity being approximately ten times higher than the steady state viscosity when $\omega = \dot{\gamma}$. Upon addition of hexamethylenediamine (HMDA) without heating the sample, both viscosity and storage modulus decreased. When the temperature was increased to 80° C, the storage modulus increased rapidly to a plateau of approximately 1375 Pa in a sample with 0.80% MFC and 3.05 mmol HMDA/g MFC.

Small, cylindrical gels were successfully cast at a concentration of 0.80% MFC with different concentrations of HMDA and ethylenediamine (EDA) at 80° C. Young's modulus was measured by longitudinal compression, and correlated well with increasing crosslinker concentrations before reaching plateau values at approximately thirty times more amine than aldehyde. The gels with HMDA were almost twice as strong as the gels with EDA. Young's modulus was largest (approximately 3220 Pa) at HMDA concentrations of 3.05 mmol/g MFC. There was a clear color change from the grey color of the regular MFC to a yellow-brown color, correlating with both crosslinker concentration and measured Young's modulus. When the non-toxic reduction agent 2-picoline-borane was added to the gels prior to casting, no color change was visible, but the gels reached almost equal Young's moduli.

Some of the cast gels were freeze-dried, and revealed a sheet-like pore structure under scanning electron microscope (SEM) imaging. The freeze dried gels showed water absorption values of approximately 8000% for pure MFC gels and 4000% for gels with HMDA.

Films were also prepared with only MFC and with concentrations of crosslinkers equal to those in the cast gels. These were imaged with laser profilometry (LP) and atomic force microscopy (AFM), and the images were analyzed for a correlation between surface roughness and crosslinker concentration. No significant correlation was observed in the AFM images, but the LP images showed a higher surface roughness at the highest crosslinker concentrations.

List of abbreviations and symbols

A	Area	Sq	Root-mean-square deviation
AFM	Atomic force microscopy		surface roughness
BNC	Bacterial nanocellulose	TA	Texture analyzer
CV	Coefficient of variation	TEMPO	2,2,6,6-tetramethylpiperidine-1-oxyl
δ	Phase angle/Phase shift		radical
DP	Degree of polymerization		
E	Young's modulus	VLR	Viscoelastic region
η	Viscosity		
EDA	Ethylenediamine		
F	Force		
G	Shear modulus		
G'	Storage Modulus		
G''	Loss modulus		
γ	Strain (relative deformation)		
$\dot{\gamma}$	Shear rate (rate of strain)		
H-bonds	Hydrogen bonds		
HMDA	Hexamethylenediamine		
LP	Laser profilometry		
μ	Poisson's ratio		
MFC	Microfibrillated cellulose		
NCC	Nanocrystalline cellulose		
ω	Angular frequency		
σ	Stress (deformation force per area)		
SD	Standard deviation		
SEM	Scanning electron microscopy		

Table of Contents

Acknowledgements	i
Sammendrag	ii
Abstract	iii
List of abbreviations and symbols	iv
1 Introduction and theory	1
1.1 Background and aim of thesis	1
1.2 On the nature of cellulose	2
1.3 Fibrillation of cellulose	5
1.4 TEMPO-mediated oxidation	7
1.5 Crosslinking	10
1.6 Biomedical applications of cellulose and other hydrogels	14
1.7 Rheology	16
1.7.1 Solids	16
1.7.2 Liquids	18
1.7.3 Viscoelastic materials	19
1.7.4 Dynamic measurements	20
1.8 Other characterization methods	23
1.8.1 Conductometric titration for determination of total carboxylate and aldehyde content ..	23
1.8.2 Macroscale characterization	25
1.8.3 Atomic force microscopy	27
1.8.4 Scanning electron microscope	29
2 Experimental	31
2.1 Reagents	31
2.2 Preparation of MFC	31
2.3 Oxidation of remaining aldehyde groups using sodium chlorite	32
2.4 Measuring carboxylate and aldehyde content	32
2.5 Qualitative gelling experiment	33
2.6 Film preparation	35

2.7	Gel casting	35
2.8	Dynamic measurements by rheometer.....	37
2.8.1	Amplitude sweep.....	37
2.8.2	Frequency sweep.....	37
2.8.3	Steady state viscosity	37
2.8.4	Small strain oscillatory measurements (temperature sweep)	38
2.9	Longitudinal measurements by texture analyzer.....	39
2.10	Micro-topographical characterization by laser profilometry.....	39
2.11	Nano-topographical characterization by atomic force microscopy.....	40
2.12	Fiber and fibril size distribution (FiberMaster).....	40
2.13	Freeze drying of gels.....	41
2.14	Scanning Electron Microscopy (SEM)	41
2.15	Water reabsorption	42
2.16	pH measurements	43
3	Results	43
3.1	Conductometric titration.....	43
3.2	Qualitative gelling experiment	47
3.3	Dynamic measurements.....	48
3.3.1	Amplitude (strain) sweeps.....	48
3.3.2	Frequency sweeps	49
3.3.3	Viscosity measurements.....	50
3.3.4	Temperature sweeps and crosslinking	51
3.4	Longitudinal compression and Young's modulus.....	55
3.5	pH measurements	61
3.6	Water absorption	62
3.7	SEM images of freeze-dried gels	65
3.8	Residual fibers and micro-topographical characterization	69
3.9	Nano-topographical characterization	71
3.10	SEM images of MFC films	74
4	Discussion.....	76
4.1	Aldehyde and carboxylate content	76

4.1.1	Conductometric titration.....	76
4.1.2	Surface carboxylate and aldehyde content.....	76
4.2	On the nature of MFC gels	78
4.2.1	Concentration dependence.....	78
4.2.2	Cox-Merz rule and nature of interactions	79
4.2.3	Dependence on pH.....	79
4.3	Crosslinking.....	80
4.3.1	Ionic or covalent crosslinks.....	80
4.3.2	Crosslinker length and concentration	81
4.3.3	Time dependence	82
4.3.4	Temperature dependence.....	84
4.4	Residual fibers	84
4.5	Biomedical applications.....	86
4.5.1	Controlling elastic modulus	86
4.5.2	Removing surplus crosslinkers	86
4.5.3	Toxicity.....	87
4.5.4	Covalent vs. weaker interactions	87
4.5.5	Water absorbance	88
5	Conclusion.....	89
	References.....	91
	List of Appendices	95

1 Introduction and theory

1.1 Background and aim of thesis

One of the main consumers of wood biomass is the paper industry, but in the later years the Norwegian paper industry have been facing large economic problems [1]. This has forced several long-established production plants to close down, most recently Peterson Paper in Moss and Södra Cell in Tofte. Because of this, along with other reasons, the development of new materials and products based on wood biomass is a focus area at many research institutions working with biomaterials, such as the Paper and Fibre Research Institute (PFI). Researchers at PFI are currently leading the NanoHeal research project, which has a goal of developing biocompatible wood-based nanostructures for advanced wound healing applications [2]. This master's thesis is the result of a collaboration between PFI through the NanoHeal project, and the Department of Chemical Engineering at NTNU.

Bacterial nanocellulose (BNC) has for a long time been used in biomedical applications such as wound dressings, temporary skin and connective tissue replacements [3]. A problem with BNC is that the nanofibrils are produced by bottom-up synthesis by bacteria, and cost-efficient mass production methods for BNC are lacking [4]. Microfibrillated cellulose (MFC) can be produced in large quantities by the fibrillation of cellulose pulp fibers from wood biomass using high-energy mechanical processing [5]. In 2006, Saito et al. introduced 2,2,6,6-tetramethylpiperidine-1-oxyl radical (TEMPO)-mediated oxidation as a method for regioselectively introducing negatively charged carboxylate groups on the surface of cellulose nanofibrils, allowing the fibrillation of cellulose fibers down to these structures at much milder mechanical treatment than before [6]. TEMPO-mediated oxidation also introduces aldehyde groups in the C6 position as an intermediate between hydroxyl and carboxylate groups [7]. Recently, Alexandrescu et al. investigated the cytotoxicity of several structures made from cellulose nanofibrils pre-treated by TEMPO-mediated oxidation [4]. They found that the nanofibrils exerted no acute toxic phenomena on tested fibroblast cells.

MFC pre-treated with TEMPO-mediated oxidation is thus a promising candidate as a material for biomedical applications. The main goal of this master's thesis was to investigate whether the elastic properties of MFC suspensions pre-treated with TEMPO-mediated oxidation could be controlled by introducing crosslinks between the nanofibrils using small diamines. The hypothesis was that amine groups on the diamines would form Schiff bases with aldehyde groups, thus yielding a covalently crosslinked hydrogel. It was hypothesized that the amount of crosslinks formed would depend on the concentration of crosslinkers added.

1.2 On the nature of cellulose

Cellulose is a naturally occurring biopolymer, and probably the most abundant macromolecule on earth. With an estimation of more than 10^{11} tons synthesized each year on our planet, it is an almost inexhaustible, sustainable raw material [8]. It is the dominant, reinforcing phase in almost all plant structures (e.g. wood, cotton and hemp), but it is also secreted by a range of bacteria (e.g. *Gluconacetobacter*), cyanobacteria, certain fungi and amoeba, and even some animals, the tunicates [5, 8, 9]. Although the description in this project will focus on the characteristic structure of cellulose from plant fibers, the most basic structure of cellulose is independent of the source of the material. On the chemical level, cellulose is an unbranched, linear polymer of repeating β -(1 \rightarrow 4)-D-glucopyranose units [10]. Two β -(1 \rightarrow 4)-D-glucopyranose units make up a cellobiose unit, which is the physically repeating unit in a cellulose polymer chain. Each glucopyranose residue is rotated close to 180° relative to its neighboring residues, and the cellulose polymer chain is stabilized in the chain direction by two hydrogen bonds (H-bonds), as can be seen in Figure 1.2.1 [11]. The polymerization occurs in the cellulose-synthesizing complex (the so-called rosette complex) of the cellulose-producing cells, from which 30-40 cellulose polymer chains are polymerized and extruded simultaneously [5, 7]. The many dipoles on glucopyranose units make the monomers very soluble in water, but as the degree of polymerization (DP) reaches about 8 or higher, the inter-chain affinity will be higher than that for water, and the cellulose polymer chains will aggregate [8]. Besides the two intramolecular H-bonds, there are intermolecular H-bonds between the polymer chains. Cellulose is divided into crystal classes based on the number and start and end points of these H-bonds. Native, naturally occurring cellulose almost solely exist as Cellulose I [8]. The cellulose

chains in Cellulose I are parallel, with H-bonds between the OH-groups on C3 on one chain and C6 on the other chain, as seen in Figure 1.2.2 [11]. The 30-40 cellulose polymer chains synthesized from the rosette complex will thus form the nanofibrils, also called elementary cellulose microfibrils, approximately 3-4 nm in diameter and several microns long, as can be seen in Figure 1.2.3 [7].

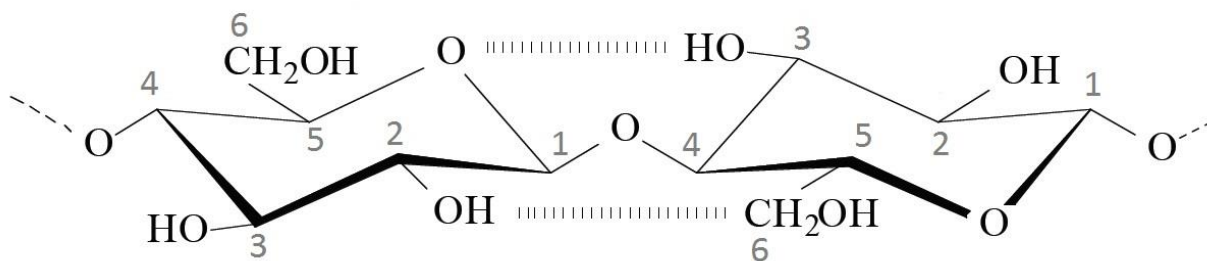
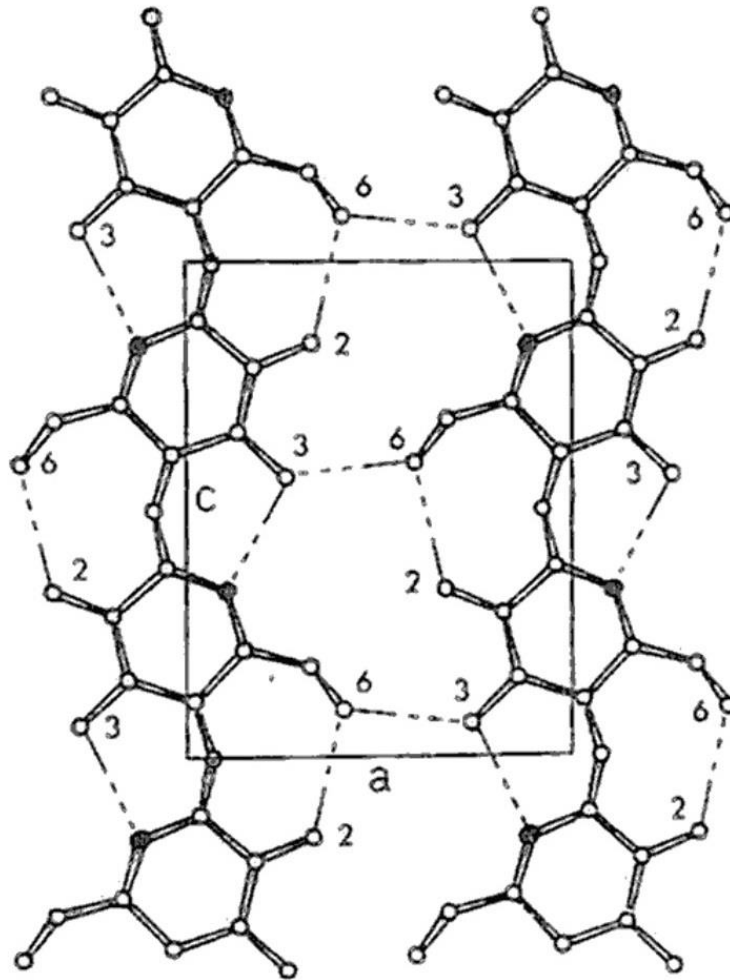


Figure 1.2.1: Cellobiose, the physically repeating unit in a cellulose polymer chain. The cellobiose is comprised of two β -(1 \rightarrow 4)-linked D-glucopyranose units. The cellulose polymer is stabilized in the chain direction by two hydrogen bonds (broad dotted lines) between: i) the H-atom in the OH-group on C3 to the ring oxygen and ii) the H-atom in the OH-group on C2 to the O-atom in the OH-group on C6. (Adapted from [11].)

Because of the finite lateral dimension of the nanofibrils, not all of the polymer chains will be crystallized, as the polymer chains belonging to the surface of the fibrils are considered non-crystalline [10]. Another factor contributing to the amount of non-crystalline polymer chains is localized distortions along the transverse direction of the fibrils, which form “weak spots” with an increased susceptibility for chemical reactions, e.g. hydrolysis. Depending on the source of the material, nanofibrils therefore show a crystallinity of 70-90% [7]. After biosynthesis, nanofibrils aggregate into nanofibril/microfibril bundles of widths >15 nm [5, 7]. In these bundles the nanofibrils are embedded in a matrix of hemicelluloses reinforced by lignin, thus from the fibril level and up, wood is a composite material [12]. As seen in Figure 1.2.3, these bundles make up the cell wall/surface of cellulose fibers. These fibers are macroscopic, hollow structures about 20 – 30 μm wide and 1 – 3 mm long, and they are the constituents of wood tissue.

i)



ii)

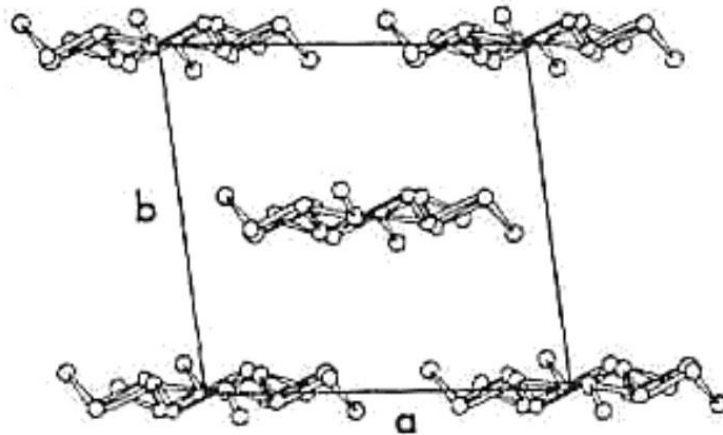


Figure 1.2.2: The structure of Cellulose I. i) Normal to the crystal plane: The cellulose polymer chains are parallel and held together by H-bonds between the OH-groups on C3 and C6. The rectangle shows the unit cell of the crystal structure. ii) Cross-section of the crystal planes: The chains are organized in a sheet-like structure. The stabilizing H-bonds are within, and not between the layers. The rhomboid shows the unit cell of the crystal structure. (Adapted from [11].)

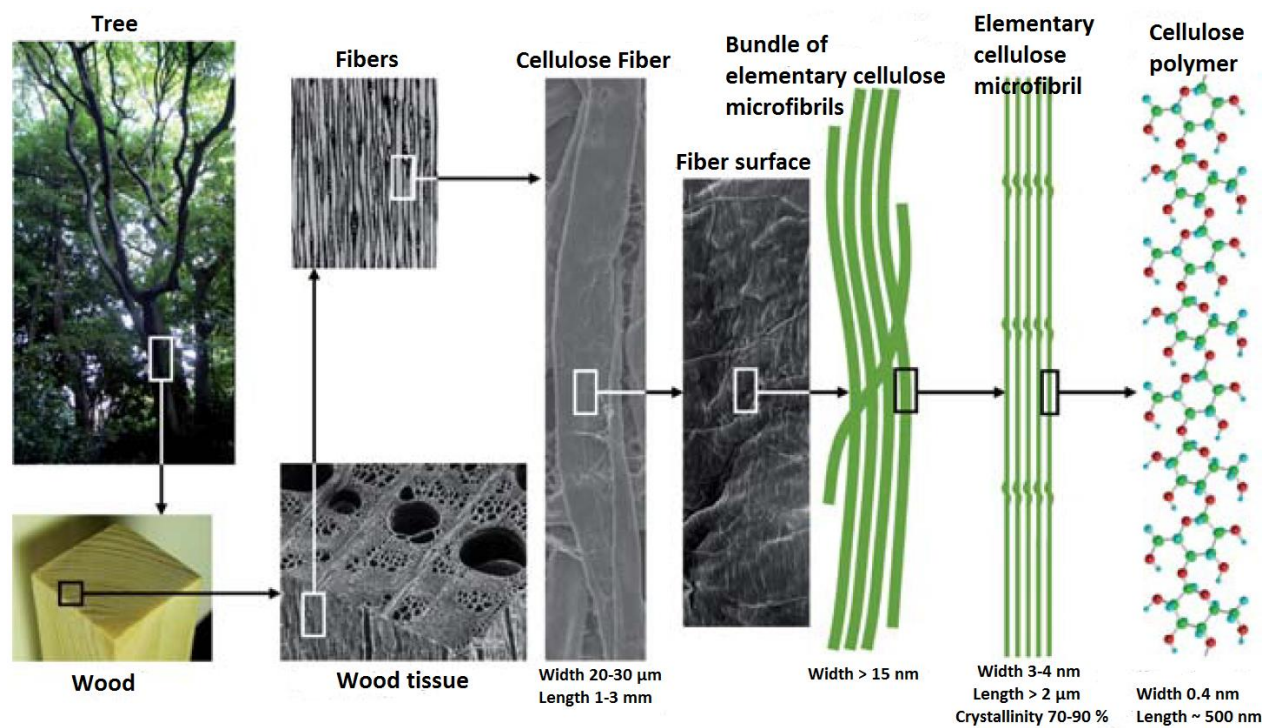


Figure 1.2.3: The hierarchical structure of wood biomass, top-down: tree \rightarrow wood \rightarrow wood tissue \rightarrow fibers \rightarrow cellulose fiber \rightarrow bundles of fibrils with different orientations make up the cell walls/surface of cellulose fibers \rightarrow elementary cellulose microfibrils/nanofibrils bundle together and are embedded in a matrix of hemicelluloses and lignin (matrix not shown in figure) \rightarrow 30-40 polymer chains make up one elementary cellulose microfibril/nanofibril, with 70-90% Cellulose I crystal structure \rightarrow a cellulose polymer chain is made up of repeating β -(1 \rightarrow 4)-D-glucopyranose units. (Adapted from [7].)

1.3 Fibrillation of cellulose

Humans have always been surrounded by cellulose, and novel ways of using this versatile material still emerges as researchers explore its capabilities further. In the form of wood and plant fibers, cellulose has been used as an energy source, for building materials, clothing and paper for millennia. In the middle of the 19th century, cellulose and cellulose derivatives began being used as a chemical raw material. Since then, novel types of materials such as celluloid and rayon and a whole range of other cellulose-based products have been developed [5]. The reduction of cellulose fibers to particles of nanometer dimensions has been known since 1949, when it was described by Rånby [13]. In this process, strong mineral acids dissolve the hemicellulose matrix and cleave and destroy the more readily accessible amorphous regions of the nanofibrils [5]. When the desired level of glucopyranose depolymerization is achieved, the sample is excessively cleaned. The remaining nanocrystalline cellulose (NCC) is dispersed as a

uniform stable suspension by sonication. NCC has also been referred to as cellulose nanocrystals or whiskers, among some synonyms. Besides from the reaction conditions, the crystallinity of the cellulose material is the main factor determining the final size of the nanocrystals. NCC from plant celluloses has lengths from 100 – 250 nm and diameters from 5 – 70 nm [5]. Suspended in water, NCC has some interesting properties such as self-ordering into liquid-crystalline chiral nematic (tread-like) phases [5]. The mechanical strength of NCC suspensions is relatively small, as the structure is only held together by a weak network of H-bonds between the rodlike, low aspect ratio crystals [10].

In the early 1980s, Sandberg et al. at ITT Rayonnier, USA, discovered that forcing suspensions of wood-based cellulose fibers (i.e. pulps) through mechanical devices such as high-pressure homogenizers (see Figure 1.3.1) delaminated the fibers and liberated (bundles of) nanofibrils [14, 15]. The most commonly used term for these nanofibrils is perhaps microfibrillated cellulose (MFC), although other names such as nanofibrillated cellulose (NFC), nanofibrils and microfibrils have been used [5]. Although nanofibrils can be comprised of fibrils as small as the elementary nanofibrils, they usually show a size distribution which can range from 5 – 100 nm, depending on the source of the material, the pre-treatment, and pressure and number of passes through the mechanical device [9]. The ISO-standard for a nano-object is that the object must have at least one dimension in the nanoscale (1 – 100 nm), and nanofibrils is thus a suitable name for the fibrils even though the lengths of the fibrils can be several microns [16]. Even so, a fibrillated material will usually contain larger fiber fragments with widths that can range up to that of cellulose fibers [17]. Hence, even though the main component in the material is the nanofibrils, MFC can be a suitable nomination when discussing the entire material.

Cellulose nanofibrils have a high aspect ratio due to the conservation of the noncrystalline domains, contrary to NCC [10]. Suspended in water, the nanofibrils form strongly entangled networks and therefore exhibit gel-like characteristics with pseudoplastic and thixotropic properties (see Section 1.7.2) even at concentrations as low as 0.125% w/w [5, 10]. Because of this, some of the first suggested uses for MFC were as a rheology modifier in foods, paints, cosmetics, pharmaceutical products, and coal and oil slurries [15].

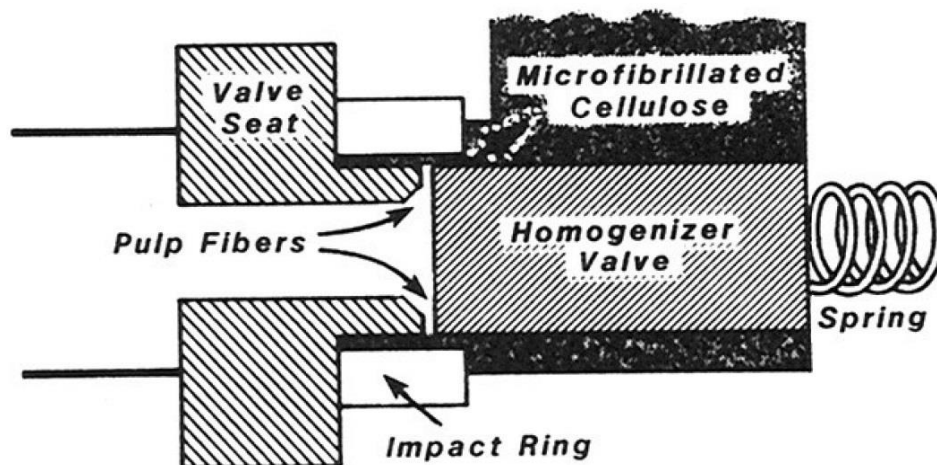


Figure 1.3.1: Schematic overview of a high-pressure homogenizer. The pulp cellulose fibers are pressed through a slit between the valve seat and the pressurized homogenizer valve. The valve opens and closes in rapid succession, subjecting the fibers to a large pressure drop with high impact and shearing forces, which lead to delamination of the fibers, thereby releasing (bundles of) nanofibrils. (Adapted from [15].)

Pulp is produced by chemically treating wood to liberate the cellulose fibers [5]. Kraft pulp is comprised of almost pure cellulose fibers, and is obtained by using a mixture of sodium hydroxide (NaOH) and sodium sulfide (Na₂S). The energy consumption for producing MFC from kraft pulp has been reported to range from 12 000 – 70 000 kWh per ton, depending on the desired fibrillation level and therefore on the required number of passes [18]. Such high energy requirements may have been one of the major factors withholding the application and commercialization of MFC products [9]. Another disadvantage with the high energy input of purely mechanical processing is the reported deterioration of both cellulose crystallinity and degree of polymerization with increasing number of passes [19]. A decrease of these factors leads to a decrease in the elasticity and strain at break of the MFC.

1.4 TEMPO-mediated oxidation

Introduction of charged species have been shown to cause swelling of the cellulose pulp fibers, thereby enhancing delamination of cellulose fiber walls [5]. Increasing charge density will also lead to a drastic decrease in fiber-fiber friction by charge repulsion, lessening the susceptibility to flocculation as well as decreasing clogging tendency in the homogenizer. Charge repulsion between the nanofibrils will also ease the fibrillation. An alternative route to decrease energy consumption is enzymatic treatment combined with mild acid hydrolysis [10].

Pioneered by Saito et al., one of the most widely used methods for introducing charged species in recent years has been 2,2,6,6-tetramethylpiperidine-1-oxyl radical (TEMPO)-mediated oxidation, as described below and seen in Figure 1.4.2 [5, 6]. The reaction regioselectively oxidizes the C6 primary hydroxyls into sodium carboxylate groups via aldehyde groups. Cellulose fibers are suspended in a solution of TEMPO and sodium bromide (NaBr) in water at pH 10-11. The reaction is started by adding sodium hypochlorite (NaClO) as the primary oxidant. NaClO oxidizes the TEMPO-radical into a nitrosonium ion, which selectively oxidize the primary hydroxyl group on C6 into an aldehyde group, and further into a carboxylate group. The introduction of C6 carboxylate groups lowers the pH of the solution, which can be used to monitor the progress of the oxidation. Continuously adding NaOH maintains the pH at 10 during the oxidation, as well as turning the carboxylate into its sodium salt form. During the oxidation, the nitrosonium ion is reduced to N-hydroxyl-amine, but it is regenerated by sodium hypobromite (NaBrO). NaBrO is created by the oxidation of NaBr by NaClO. NaBrO and NaClO also directly contribute to the oxidation of C6 aldehyde further into C6 carboxylate. NaClO is the limiting reagent in the oxidation, and the only reagent (except cellulose) that is not regenerated. Thus controlling the concentration of NaClO can be used to control the degree of oxidation (DO). The carboxylate and aldehyde content can be determined by conductometric titration, as described in Section 1.8.1. The introduction of the negatively charged carboxylate groups makes it possible to defibrillate cellulose fibers down to nanofibrils, with much milder mechanical treatment than previously reported methods [6].

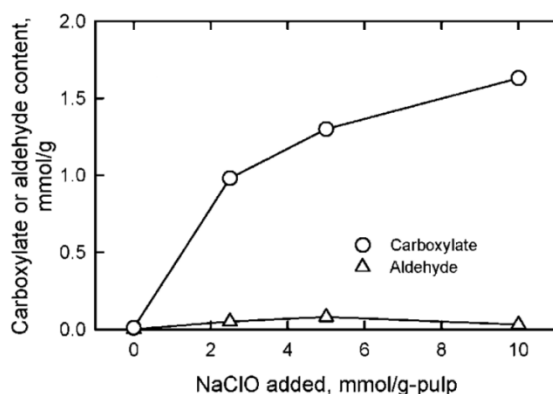


Figure 1.4.1: Relationship between carboxylate and aldehyde concentration and NaClO concentration in the TEMPO/NaBr/NaClO oxidation of bleached softwood kraft pulp at room temperature and pH 10. Oxidation time is not stated. (Adapted from [7].)

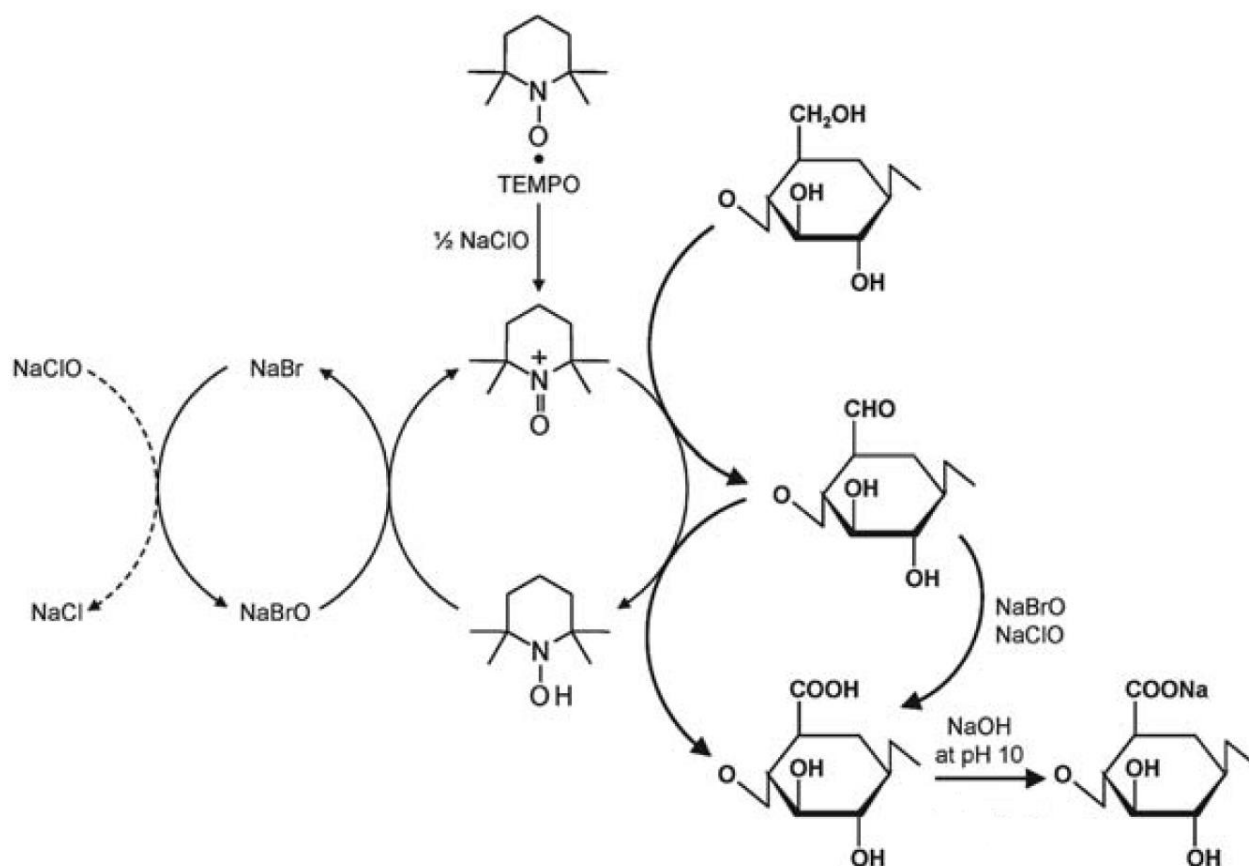


Figure 1.4.2: Introduction of negatively charged C6 carboxylate groups via aldehyde groups by TEMPO-mediated oxidation. (Adapted from [7].)

Figure 1.4.1 shows that the carboxylate content increases from 0.01 to 1.70 mmol/g pulp by increasing the amount of NaClO to 10 mmol/g pulp [7]. Saito et al. found that the carboxylate content should reach approximately 1.5 mmol/g cellulose to obtain a close to full fibrillation, i.e. individual cellulose nanofibrils with nearly uniform lateral size of 3-4 nm, of both once-dried and never-dried hardwood celluloses [20]. Calculations showed that this corresponded to one in two anhydroglucose units of the cellulose fibril surface being oxidized into an anhydroglucuronic acid unit. Later, this was confirmed by a study by Okita et al., where the total amount of carboxylate groups in totally fibrillated MFC from various sources was experimentally determined [21]. The MFC had been treated with NaClO in excess (10 mmol/g cellulose) for 5 hours to ensure full oxidation into C6 carboxyl groups. By accounting for the differences in crystal structure widths from the various sources, total number of anhydroglucose units on the surface of nanofibrils with Cellulose I structure was calculated, and was in good, quantitative

agreement with the experimental results. This showed that the oxidation occurs only at the surface of Cellulose I crystal structure. The results also suggested that carboxylate and aldehyde groups were partly formed inside the more accessible amorphous and disordered regions of the nanofibrils, in addition to on the surface.

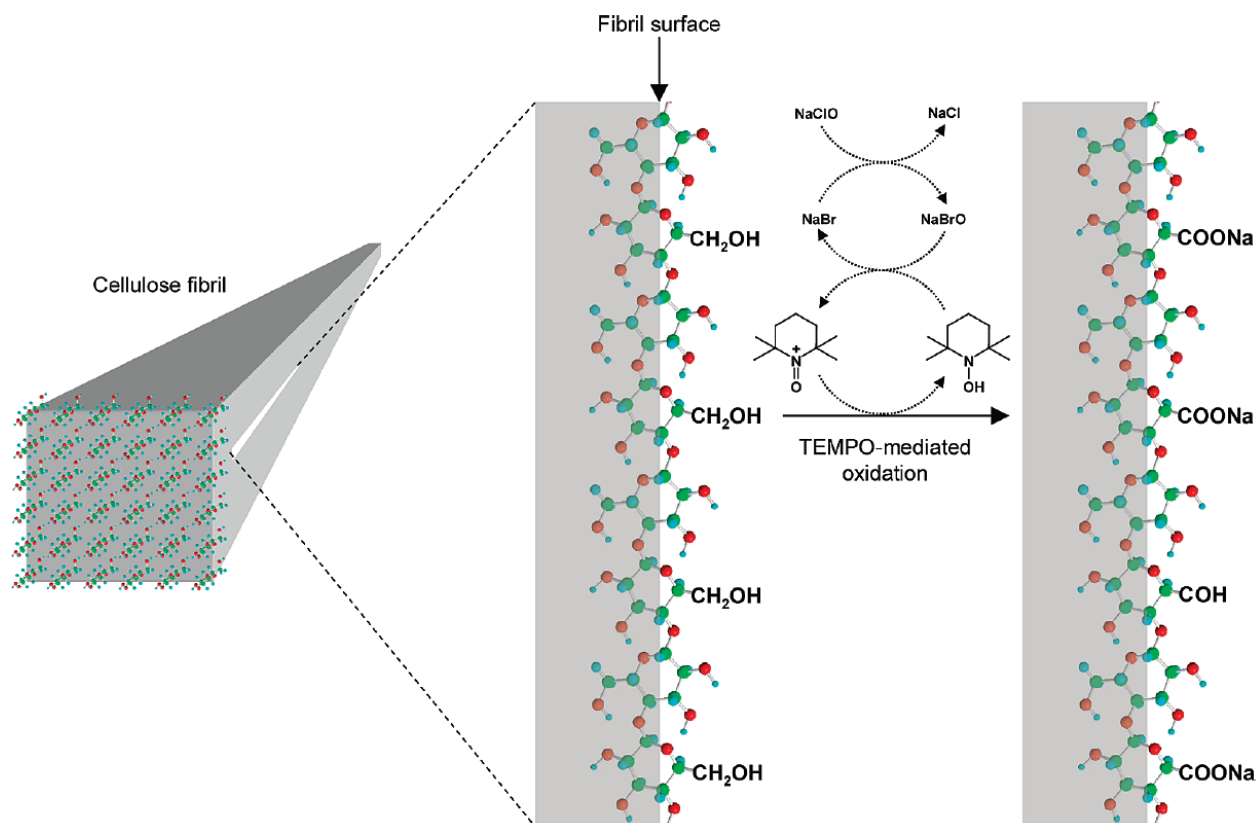


Figure 1.4.3: TEMPO/NaBr/NaClO-mediated oxidation of C6 hydroxyl groups on the Cellulose I crystal surface of nanofibrils into aldehyde and carboxyl groups. Due to the 180° rotation of neighboring anhydroglucose subunits, every second C6 group faces inwards into the crystal structure. The maximum degree of oxidation is therefore every second C6 anhydroglucose surface unit. Notice the two remaining hydroxyl groups between the oxidized C6 groups. (Adapted from [21].)

1.5 Crosslinking

In regards of the fibrillation process, the aldehyde groups introduced by the TEMPO-mediated oxidation are idle byproducts. Being an intermediate product, aldehyde concentrations have by some been reported to be higher than carboxylate concentrations at low concentrations of NaClO, where the limited amount of the primary oxidant hinders the further oxidation into carboxylate [22]. This can also be observed in Table 1.5.1. At surplus of NaClO and longer

oxidation times, the amount of carboxylate groups is much higher while the amount of aldehyde groups decreases significantly.

Table 1.5.1: Amount of carboxylate and aldehyde groups measured on different samples, with various amounts of NaClO and at various oxidation times. All concentrations are in mmol/g MFC in the samples.

Sample	NaClO [mmol/g]	Time [min]	Carboxylate [mmol/g]	Aldehyde [mmol/g]	Reference
Hardwood kraft pulp	0.30	<30	0.08	0.20	[22]
Hardwood kraft pulp	0.61	<30	0.27	0.22	[22]
Softwood sulfite pulp	1.3	5	0.45	0.35	[6]
Softwood sulfite pulp	3.8	42	1.23	0.25	[6]
Hardwood kraft pulp	10	300	1.65	0.07	[21]
Softwood kraft pulp	10	300	1.69	0.00	[21]

Being much more reactive than carboxyl groups towards forming covalent bonds with other chemical moieties, surface aldehyde groups can be used to introduce covalent crosslinks in a network of cellulose fibers or fibrils. Saito and Isogai used TEMPO-mediated oxidation with low amounts of NaClO to introduce aldehyde groups into hardwood kraft pulps [22]. The cellulose fibers were not fibrillated, but made into sheets on which wet tensile strength was tested. The wet tensile strength correlated with the amount of aldehyde on the surface on the cellulose fibers, but showed no correlation with total carboxylate or aldehyde content. This was explained as being a result of the formation of hemiacetal linkages between surface aldehyde and hydroxyl groups on the cellulose fibers. Han et al. used partial oxidation with sodium metaperiodate to manufacture dialdehyde cellulose (DAC) by the cleavage of the C2 – C3 bond on cellulose fibers from lyocell fabrics [23]. These dialdehyde groups were successfully crosslinked through Schiff-base formation with multifunctional amines such as melamine. The crosslinking was more successful at higher temperatures (80° C). The crosslinks were stabilized by reduction with sodium borohydride. Fibers with successfully formed crosslinks swelled less in water due to denser structures and were harder to fibrillate. Syverud et al. used TEMPO-

mediated oxidation with 3.8 mmol NaClO/g cellulose to introduce carboxylate and aldehyde groups on *P. radiata* (softwood) kraft pulp fibers, which were fibrillated into MFC [24, 25]. Polyethyleneimine (PEI; molecular weights 600 and 1,800 g/mol) and poly N-isopropylacrylamide-co-allylamine-co-methylenebisacrylamide particles were added to MFC suspensions of 0.5% w/v, and crosslinks were introduced by cryogelation at -12° C for 16 hours. This resulted in spongy and elastic gels after thawing and washing.

The formation of Schiff-bases between a primary or secondary amine and an aldehyde or ketone is a well-known chemical reaction, especially within biochemistry where it is used to tag, label or crosslink proteins or glycans [26]. A Schiff-base is a relatively labile double bond between the nitrogen of the amine and carbon on the aldehyde, as seen in Figure 1.5.1. At pH 9-10 the formation is more efficient than at pH values closer to neutral. In the reaction, the oxygen of the aldehyde and two hydrogen atoms are released and form a water molecule. A Schiff-base is theoretically reversible by hydrolysis in aqueous solution. The Schiff-base can be reduced to a highly stable secondary or tertiary amine linkage by a suitable reduction agent. Both the Schiff base and secondary amine linkage are zero-length cross-links where no additional spacer atoms are introduced between the molecules.

Two of the most widely used reduction agents are sodium borohydride and sodium cyanoborohydride, the latter approximately five times milder than the first [26]. Cyanoborohydride has often been preferred, as it is specific towards the Schiff base and will not affect the original aldehyde groups. It can therefore be used in a one-pot reaction. Reduction with borohydride is on the other hand a two-step process, where the borohydride has to be added after the Schiff-base formation, or it would rapidly reduce any non-reacted aldehydes into non-reactive hydroxyls. The major drawback with these reduction agents is their toxicity. Upon hydrolysis, sodium cyanoborohydride forms the toxic, volatile compound hydrogen cyanide [27]. Sodium triacetoxymethylborohydride ($\text{NaBH}(\text{OAc})_3$) has been introduced as a non-toxic alternative to sodium cyanoborohydride, but it is not compatible with water as a solvent, due to a rapid destruction of the carbonyl compound or decomposition of the reducing agent in water [28]. In 2004, Sato et al. introduced picoline-borane as another non-toxic reduction agent, suitable for one-pot reductive amination in solvents such as methanol, ethanol and water [28].

It was found that a large range of amines and carbonyls could be coupled with high yields through reductive amination with picoline-borane, in a solvent of water and ethanol (10:1 H₂O – AcOH). Later, Ruhaak et al. showed that *N*-glycans from human plasma and glucose oligomers could be labeled with fluorophores containing primary amines through reductive amination of Schiff-bases with 2-picoline-borane as the reduction agent [27]. 2-Picoline-borane showed labeling efficacies similar to sodium cyanoborohydride under both aqueous and non-aqueous conditions.

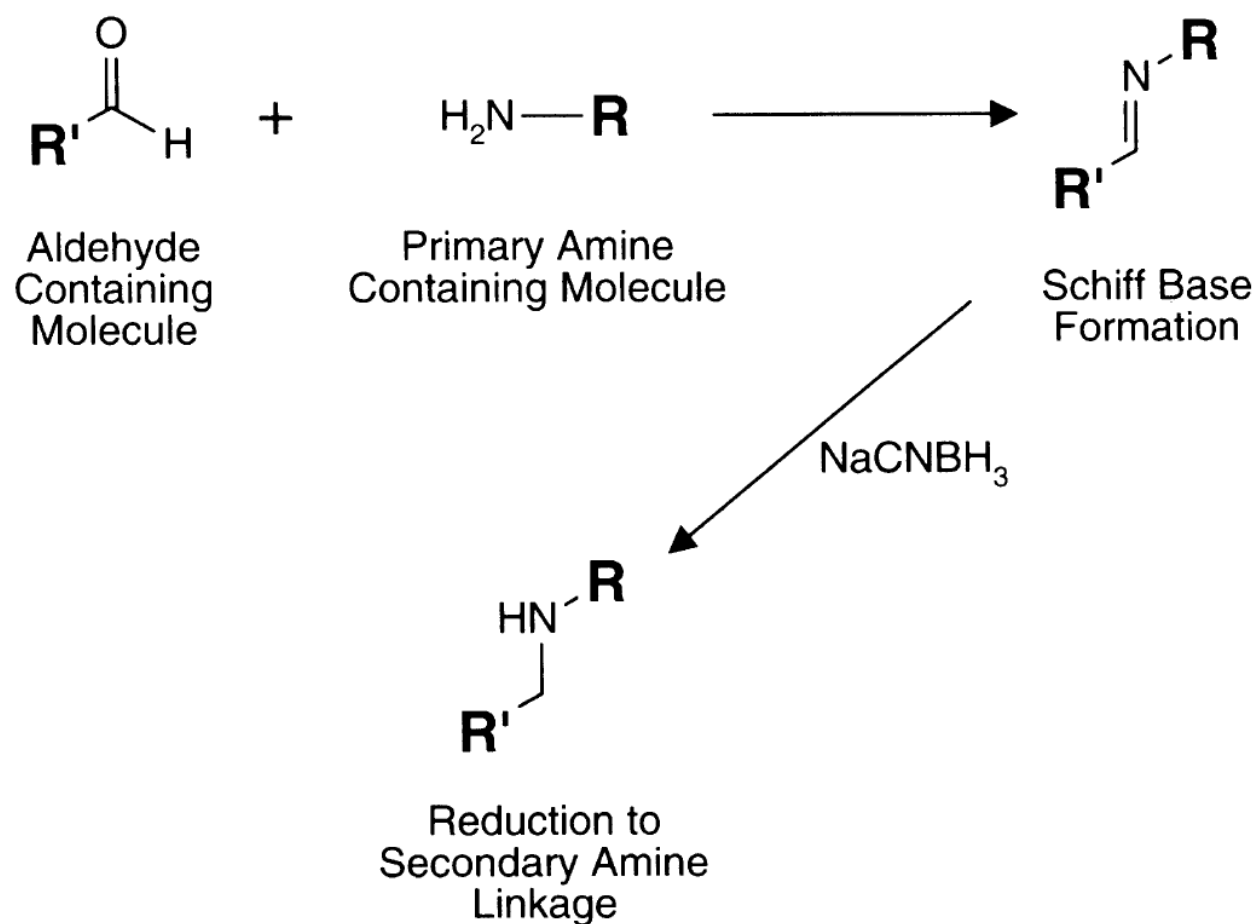


Figure 1.5.1: The formation and reduction of a Schiff base: An aldehyde containing molecule (e.g. TEMPO-oxidized cellulose) can react with an amine containing molecule (e.g. HMDA) to form a Schiff base. The linkage can be stabilized by reduction to a secondary amine linkage by an appropriate reduction agent, such as sodium cyanoborohydride. (Adapted from [26].)

1.6 Biomedical applications of cellulose and other hydrogels

As mentioned in Section 1.2, cellulose can also be produced by bacteria. Bacterial nanocellulose (BNC) does not differ from plant based cellulose on the polymeric level [5]. For industrial and academic production, BNC is excreted by aerobic bacteria at the interface between an aqueous nutrition media and air. The resulting nanofibrils are almost pure cellulose with only hydroxyl functional groups, diameters of 20 – 100 nm, high crystallinity of 80 – 90%, good mechanical stability, and high DP (4000 – 10000 anhydroglucose units). As the nanofibrils are formed by biotechnical assembly processes from low-molecular weight carbon sources, no fibrillation is necessary. The biotechnological origin of BNC as well as the properties mentioned above has led to a much more thorough investigation of BNC than MFC for biomedical applications. The multiple uses of BNC for biomedical applications are outside the scope of this thesis, but have been excellently reviewed by Klemm et al. [3, 5]. The results are not necessarily directly transferable from BNC to MFC, due to differences in morphology, possible post-processing residues, and introduction of other functional groups on the latter, but the possibilities for biomedical uses of MFC can still be perceived. BNC have been used as a three-dimensional (3D) template for *in vitro* and *in vivo* tissue growth to create (commercial) wound and burn dressings, grafts for vascular surgery, and for cartilage and bone repair [5]. BNC implants do not show any foreign-body reactions, such as fibrosis, capsule formation or giant cells, when evaluated *in vitro* and *in vivo*. Even further, implantation of BNC tubes into rats showed integration by endothelization of the inner surface, outside colonization by connective tissue and ingrowth of collagen-forming fibroblasts.

Much of the reason for the aptness of BNC for biomedical purposes is its excellent hydrogel properties, such as forming a stable nanofibril network that encloses up to 99% water; a property shared with and to some extent surpassed by MFC. Hydrogels are 3D networks of mainly hydrophilic polymers capable of absorbing up to thousands of times their own dry weight in water [29, 30]. Hydrogels can simulate hydrated structural aspects of the extracellular matrix (ECM), and have therefore been excessively studied for biomedical applications. There are several driving forces behind the large water absorption properties of hydrogels [29]. Both hydrophilic and hydrophobic areas of the polymers will interact with and bind water. The

entropic/osmotic driving force of the network chains towards infinite dilution will lead to further imbibition of water. Physical or chemical crosslinks oppose this additional swelling, which lead to an elastic network retraction force. As the opposing forces cancel each other out, the hydrogel reaches an equilibrium swelling level.

There is a large variety of different polymers of both natural and synthetic origin used in hydrogels for biomedical purposes [31]. Independent of origin, hydrogels can be divided into two categories [29]. In a *reversible* or *physical* gel, the polymer network is held together by molecular entanglements, and/or secondary forces including ionic, hydrogen-bonding or hydrophilic forces. Hence the interactions in physical gels are reversible, and they can be disrupted by changes in physical conditions such as ionic strength, pH, temperature, application of stress, or addition of specific solutes. In a *permanent* or *chemical* gel, the polymers are covalently crosslinked. A regular MFC or BNC suspension only held together by entanglements and H-bonds can therefore be viewed as a physical gel, while a TEMPO-oxidized MFC suspension covalently linked through its aldehyde groups is an example of a chemical gel. Some articles distinguish between nanofibrous scaffolds, which resemble the fibrillar ECM proteins *in vivo* by presenting a 3D nanostructured topology, and hydrogels [32]. Accounting for the nanoscale width dimensions of MFC along with the hydrophilic nature of the cellulose polymer constituents, a hydrated MFC network can be viewed as both.

Besides from the high water content of hydrogels, there is a range of other properties that are important for successful application for biomedical purposes, such as degradation, bioadhesion, bioactivity, transport through the network, and mechanical properties [30]. An investigation of all such relevant factors would demand a much larger project than a master project spanning 20 weeks. In this project, the main focus has been to investigate the mechanical, structural and viscoelastic properties of the (crosslinked) MFC hydrogels. There is a dynamic, complex interplay between the 3D environment of the ECM and the cells living in it. One of the factors that cells rely on is the elasticity of the ECM, which varies significantly depending on tissue, as seen in Figure 1.6.1 [33]. Cells attach to the ECM through a vast array of adhesive proteins, pull against the matrix and “feel” the resistance to deformation by the adjacent environment. Mechanically sensitive proteins along this connection will provide feedback, actuating processes in the cell

[33]. It has been shown that naive mesenchymal stem cells will specify lineage and commit to phenotype depending on the elastic modulus of the *in vitro* gel system in which they are grown [34]. Studies have also shown that the elastic modulus of the matrix is interconnected with oncogenesis [35]. Thus improving the control of mechanical properties is an important factor when developing hydrogels for biomedical applications, e.g. as implants or relevant *in vitro* test systems.



Figure 1.6.1: The various elastic moduli (E), exhibited by solid tissues. (Adapted from [34].)

1.7 Rheology

Rheology is the study of the flow and deformation of matter [36]. In addition to being applicable to liquids, rheological models can also be used to describe other states of matter, such as gels and solids.

1.7.1 Solids

A solid material can exhibit various rheological characteristics, such as the amount of deformation or force required to cause the material to fracture (tough vs. brittle) or the resistance of the material to an applied force (soft vs. hard) [36]. An *ideal elastic* or *Hookean* solid is a material where there is a linear relationship between the applied force per unit area (*stress*, symbolized by σ , units: N/m^2 or Pa) and the relative deformation (*strain*, symbolized by γ , dimensionless). The linear gradient in this relationship is the elastic modulus of the material. As can be seen in Figure 1.7.1, a stress can be applied to a material in a number of ways. The elastic modulus for the two modes shown in Figure 1.7.1 is called Young's modulus (E) and shear modulus (G), respectively (units: N/m^2 or Pa). These relationships are summed up in Table 1.7.1. For these relationships to apply, the material properties must be the same in all directions, i.e. the material must be homogeneous and isotropic. Poisson's ratio μ gives the relationship between the two elastic moduli as $E = 2G(1 + \mu)$, where $-1 \leq \mu \leq 0.5$ for an isotropic material ($\mu = 0.5$ for an incompressible (ideal) material) [37].

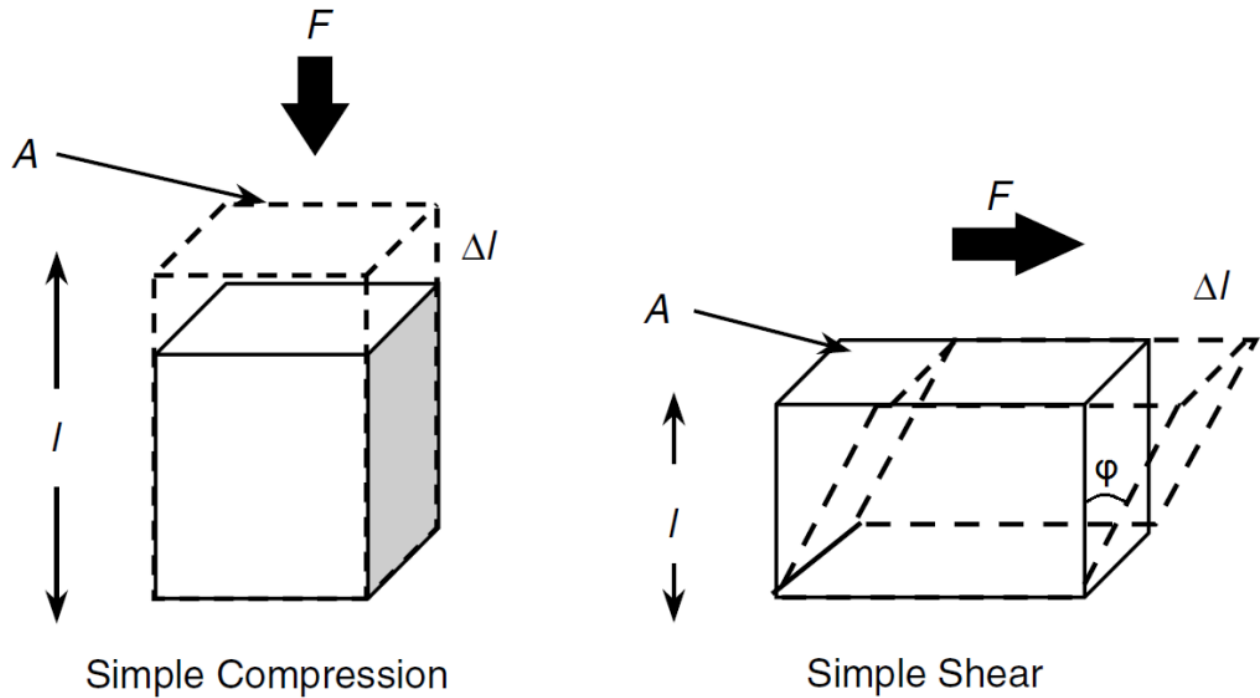


Figure 1.7.1: Depending on the direction of the applied stress, an elastic solid can be deformed in different ways. Here A is the basal area of the material, F is applied force (normal to A for compression, parallel to A for shear), l is the initial length of the material, Δl is change in l due to the applied stress, and ϕ is the angle of deformation. (Adapted from [36].)

Real, non-ideal elastic materials only show Hookean behavior at relatively small strains [36]. In this linear region the material acts as an ideal elastic solid, and the elastic modulus is independent of stress and strain. At larger applied stresses, the deformation is no longer proportional with the stress. Up to a certain strain above the Hookean regime, the material can still return to its original shape once the force is removed. Above this strain, the material either fractures or flows (see next section), and the solid will not return back to its original shape after the applied stress is removed.

Table 1.7.1: Rheological parameters for different types of deformations of elastic solids.

Deformation	Stress	Strain	Elastic Modulus
Simple compression	$\sigma = \frac{F}{A}$	$\gamma = \frac{\Delta l}{l}$	$E = \frac{\sigma}{\gamma} = \frac{Fl}{A\Delta l}$
Simple shear	$\sigma = \frac{F}{A}$	$\gamma = \frac{\Delta l}{l} = \tan \phi$	$G = \frac{\sigma}{\gamma} = \frac{F}{A \tan \phi}$

1.7.2 Liquids

An *ideal* or *Newtonian* liquid will flow when shear stress is applied, and will continue to flow after the applied stress is released, until the kinetic energy stored within the liquid is dissipated as heat due to friction [36]. An ideal liquid is the exact opposite of an ideal solid, as there is no elastic recovery of the material once the applied stress is removed, that is, it does not return to its original shape. In an ideal liquid the shear stress is proportional with the shear rate (or rate of strain, symbolized by $\dot{\gamma}$, unit: sec^{-1}), and not the strain as in an ideal solid, as seen in Table 1.7.2. The linear gradient in this relationship is the (shear or steady state) *viscosity* (symbolized by η , units: N sec m^{-2} or Pa sec) of the liquid. The viscosity is a result of the frictional force that arises as the (macro)molecules in the liquid slide past one another. It is thus a measure of the resistance to flow in the liquid; the higher the viscosity, the more friction in the liquid.

Table 1.7.2: Rheological parameters for an ideal Newtonian liquid. A shear force F is applied over a contact area A to a confined liquid, yielding a stress σ . This leads to a velocity v of the liquid at the surface area where the force is applied. Due to friction between the molecules of the liquid, the added energy will dissipate as heat and the liquid will be at rest a distance l away from the applied force. This yields a velocity gradient: the shear rate $\dot{\gamma}$, which equals the time derivate of the deformation strain. The viscosity is the ratio between the shear stress and the shear rate.

Deformation	Shear stress	Shear rate	Viscosity
Simple shear	$\sigma = \frac{F}{A}$	$\dot{\gamma} = \frac{d\gamma}{dt} = \frac{dv}{dl}$	$\eta = \frac{\sigma}{\dot{\gamma}} = \sigma \frac{dt}{d\gamma} = \sigma \frac{dl}{dv}$

The viscosity of a Newtonian liquid is independent of applied shear stress and strain rate [36]. It is dependent on temperature, and so temperature should always be stated together with the viscosity value. Water is a Newtonian liquid, with a viscosity at room temperature of about 0.001 Pa sec .

In many real liquids, viscosity is dependent on the shear rate, as seen in Figure 1.7.2 [36]. In such systems the viscosity at a particular shear rate is referred to as *apparent* viscosity. The two most common non-ideal shear-rate dependent fluid behaviors are *pseudoplastic* and *dilatant*. In pseudoplastic fluids, the viscosity decreases as the shear rate is increased, and the behavior is thus also referred to as *shear thinning*. This is a common behavior in polymer based systems,

due to the deformation and disruption of entanglements, and the alignment of (parts) of the polymers with the flow field at higher shear rates. The opposite is dilatant or *shear thickening* behavior. This is rarer, but can be observed e.g. in concentrated emulsions or suspensions where the particles are packed tightly together.

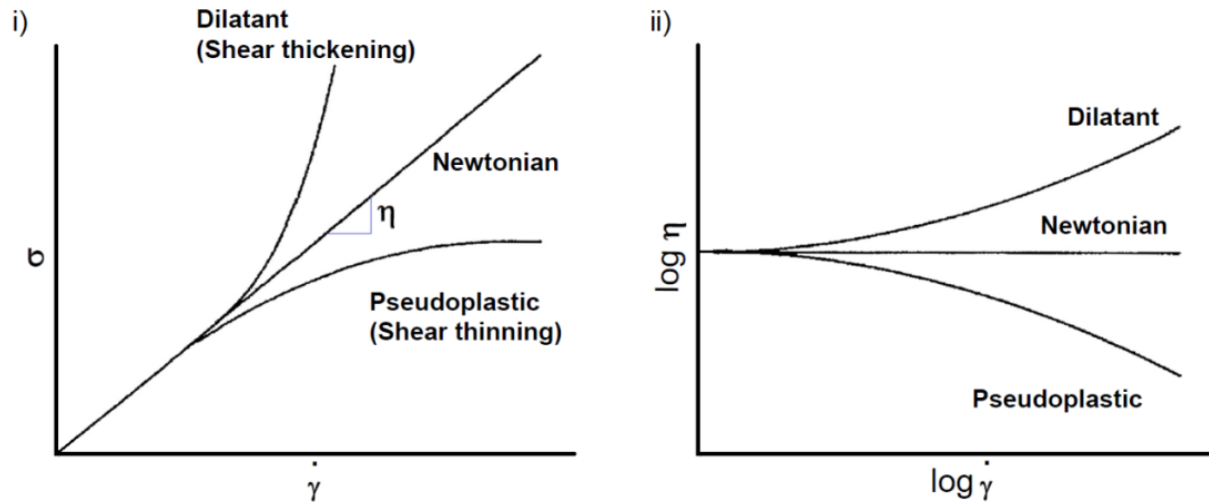


Figure 1.7.2: Comparison between the viscosities of ideal (Newtonian) and non-ideal (dilatant and pseudoplastic) liquids. i) Shear stress as a function of shear rate. ii) Apparent viscosity as a function of shear rate. Notice the logarithmic axes. (Adapted from [38].)

The viscosity can be time-dependent in addition to being dependent on shear rate. [36] One such behavior is *thixotropic*, in which the apparent viscosity decreases with time as the fluid is subjected to a constant shear rate. This behavior is most often seen in systems that are aggregated by weak forces, such as H-bonds and entanglements, where a constant shear rate over time will disrupt the aggregates and decrease the resistance to flow. Alternatively, the viscosity can increase due to network formation (*gelling*) over time.

1.7.3 Viscoelastic materials

Most materials act neither as pure ideal solids nor as pure ideal liquids, but have rheological properties in between the two extremities [36]. A viscoelastic material will exhibit both elastic and viscous behaviors simultaneously, i.e. part of the deformational energy will be stored as mechanical energy within the material, and part is dissipated as heat. This dissipation of part of the deformational energy due to viscous (frictional) forces is an invariable result of the second law of thermodynamics [37]. A viscoelastic material subjected to a force will therefore never

instantaneously adopt its new dimensions nor will it instantaneously return back to its nondeformed state when the force is removed (as an ideal elastic material would) [36]. Hence all elastic constants when measured on viscoelastic materials will inherently be functions of time or frequency [37]. All materials will show viscous behavior over a long enough time span, but the higher the elastic contribution, the longer the observation time has to be to observe this [39]. To apply the theory of ideal elastic solids on real materials, one has to assume that the time-dependence of its mechanical properties can be neglected, which it can for many materials such as metals and most elastomers at relevant observation times [37]. The rheological properties of a viscoelastic material are characterized by a complex elastic modulus, G^* (when the applied stress is simple shear) [36]. The complex elastic modulus is comprised of an elastic and a viscous contribution:

$$G^* = G' + iG'' \quad (1.7.1),$$

where the real part of the complex modulus (G') is known as the *storage* modulus (elastic contribution) and the imaginary part (G'') is known as the *loss* modulus (viscous contribution).

In a hydrogel, the 3D network of the polymers (or nanofibrils in MFC) is the solid, structural phase. The storage modulus of an elastic material is related to the strength of the intra- and intermolecular forces and bonds holding the molecules and structural units together, as well as to the number of interactions per unit area [36]. At small applied strains, energy will be stored by compressing or expanding these bonds, i.e. as increased enthalpy, and/or by reducing the entropy of the chains in the network [39]. The free chain ends of a chemical gel will thus represent a gel network “defect” that does not contribute to the elasticity of the network [29]. At larger strains, the applied force exceeds the forces holding the structural units together and the hydrogel will show more viscous behavior [36].

1.7.4 Dynamic measurements

In a dynamic rheometer, the sample is placed in a thermostated measurement cell with a fixed bottom plate and subjected to a controlled angular shear stress or strain by either a rotating cone or plate probe, as seen in Figure 1.7.3 [36]. The rheometer can be used in a strain controlled mode, in which the plate or cone is driven to a *strain* (angular deflection of the cone

or plate) that can be increasing or oscillating, and the resultant *torque* (angular force, unit: N m) is measured. The torque is converted to shear stress by the computer controlled rheometer. For investigation of the viscous properties of the sample, the *shear rate* (the speed at which the cone or plane rotates) can be controlled instead. Alternatively, the torque can be controlled, and the strain or rate of strain needed to reach the desired torque is measured.

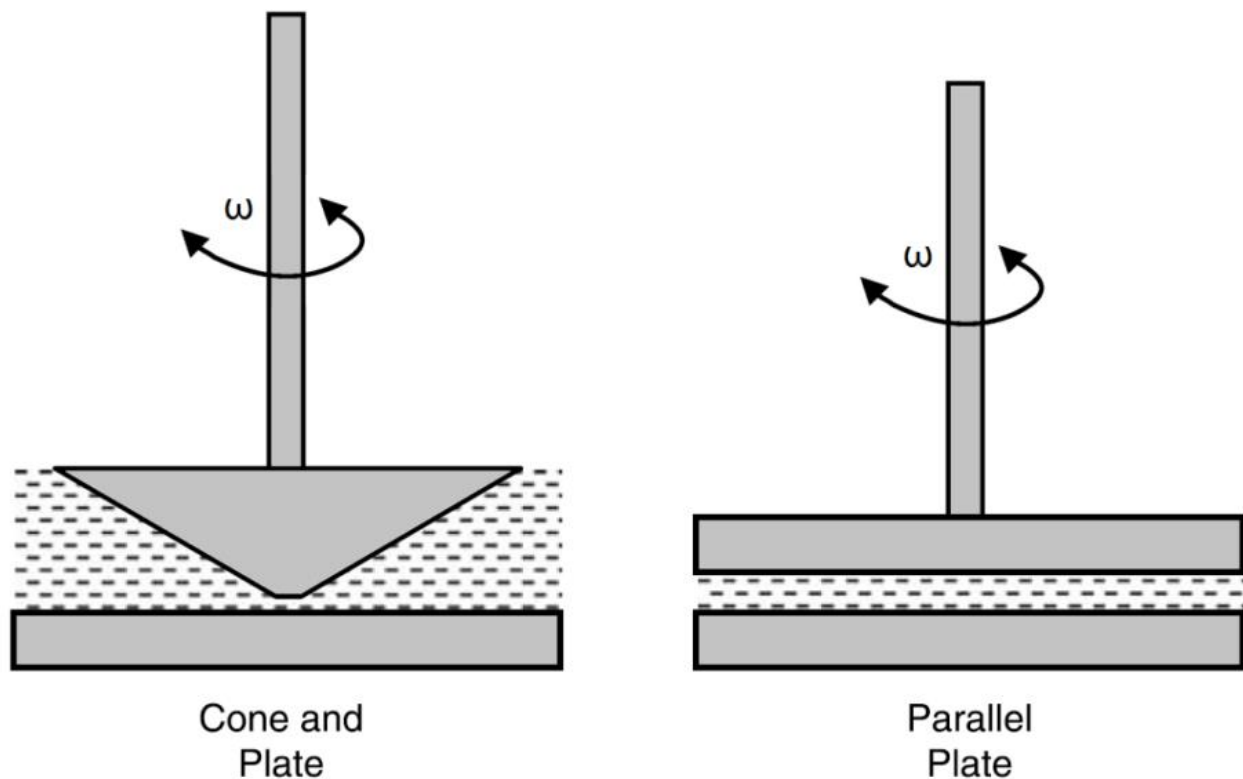


Figure 1.7.3: Two types of measurement geometries often used in dynamic shear rheometers. The top cone or plate is driven by applying a certain torque, strain or shear rate, while the bottom plate is stationary. Due to the angular movement of the probe, the torque and thus the shear stress will be smaller in the middle of the sample than at the edges when using plate-plate geometry. If the sample shows non-ideal viscous behavior (i.e. is dependent on shear rate), cone-plate geometry is more suited, as this is designed to ensure a more uniform shear stress across the sample. (Adapted from [36].)

The viscoelastic properties of a material can be investigated by applying a sinusoidal shear strain to the material and measure the resulting sinusoidal shear stress, or vice versa [36]. In strain controlled mode, this is done by oscillating the cone or plate at an angular frequency ω (unit: rad sec^{-1}) to a specific maximum amplitude (γ_0), as described in Figure 1.7.4.

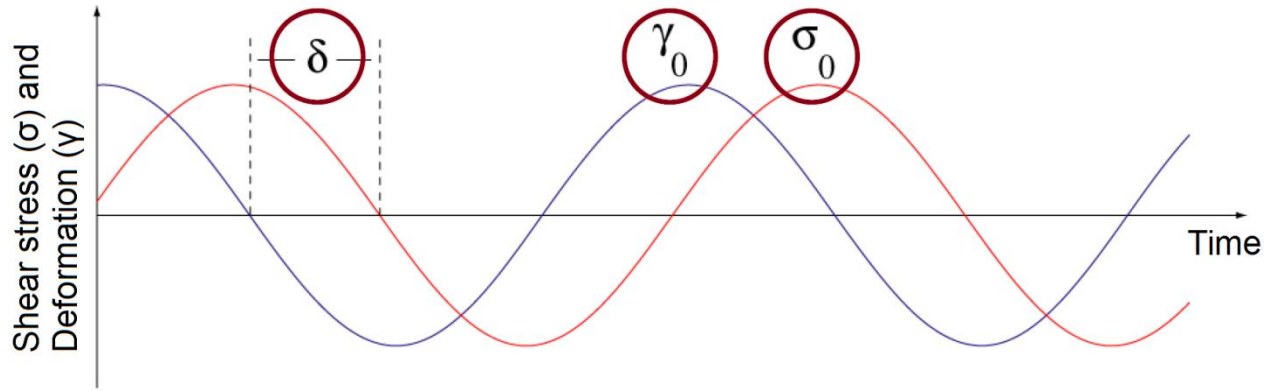


Figure 1.7.4: A dynamic measurement determines rheological properties of a viscoelastic material by measuring the relationship between an applied sinusoidal strain with a maximum amplitude γ_0 and the resulting sinusoidal shear stress with maximum amplitude σ_0 (or vice versa). The oscillating strain and stress have the same angular frequency (ω), but due to viscous dissipation of some of the applied deformational energy, the response will not be instantaneous, but delayed by a certain phase shift (δ), specific for the material at the given frequency. (Adapted from [38].)

Viscous dissipation of some of the deformational energy will lead to a phase angle/shift (δ) between the input and the measured response. The storage and loss moduli of the material are obtained from this phase shift and the maximum applied and resultant amplitudes, γ_0 and σ_0 , as described by Equations (2.2.2 – 2.2.4):

$$G' = \left(\frac{\sigma_0}{\gamma_0} \right) \cos \delta \quad (2.2.2),$$

$$G'' = \left(\frac{\sigma_0}{\gamma_0} \right) \sin \delta \quad (2.2.3),$$

$$\frac{G''}{G'} = \tan \delta \quad (2.2.4).$$

Table 1.7.3: Relations between the storage modulus G' , loss modulus G'' , phase angle δ , and viscoelastic behavior.

G', G''	δ	Behavior
$G' < G''$	$> 45^\circ$	Viscoelastic liquid
$G' = G''$	$= 45^\circ$	Transition
$G' > G''$	$< 45^\circ$	Viscoelastic solid (e.g. a gel)

For the theory on elastic materials to apply, the strain should be sufficiently small that the material is in the *viscoelastic region* (VLR), i.e. the region where stress is proportional to strain. At strains higher than the VLR, the structure of the material can be affected, e.g. through the disruption of the weak or strong bonds holding a hydrogel together [36]. The VLR can be found by doing an amplitude (strain) sweep and identifying the region where the storage modulus is constant. For any given material the viscoelastic properties described in Table 1.7.3 can vary with the time scale of the observation, i.e. ω^{-1} , as previously mentioned. Varying the frequency while keeping a constant strain within the VLR can thus give valuable information e.g. on the type of cross-links in a polymer solution, without disrupting the structure of the material. For example will covalent cross-links be permanent over longer relevant observation times and the phase angle thus constant and $<45^\circ$, whereas non-permanent interactions with relaxation times within the observation period can yield increasing δ at lower frequencies [39]. Such a frequency sweep will also yield the frequency-dependent *dynamic viscosity*, η^* , of the material without disrupting the structure of the sample. For many materials, the dynamic viscosity can be correlated with the shear rate dependent (apparent) viscosity η through the empirical Cox-Merz rule [40]. It states that $\eta^*(\alpha\omega) = \eta(\dot{\gamma})$ when $\dot{\gamma} = \omega = 2\pi f$, where the term α can be adapted to improve the agreement between the two sets of data [38, 41].

1.8 Other characterization methods

1.8.1 Conductometric titration for determination of total carboxylate and aldehyde content

Da Silva Perez et al. compared several characterization methods for measuring the carboxylate content of TEMPO-oxidized cellulose; the carbazole chemical method (hydrolysis and colorimetric determination), ^{13}C NMR spectroscopy, quantitative infrared spectroscopy (FTIR), conductometric titration and methylene blue adsorption [42]. It was found that methylene blue absorption and the carbazole method seemed to underestimate the carboxyl content, while ^{13}C NMR seemed to overestimate it. The only methods that could measure on both water-soluble and insoluble samples were FTIR and conductometric titration. Of these two, FTIR showed low repeatability due to problems associated with quantification, whereas conductometric titration yielded very reproducible results. Because of this, conductometric titration was given as the

most attractive and reproducible method for determining carboxylate content on cellulose. Habibi et al. also found this method to give results with remarkable reproducibility [43]. Later, Saito and Isogai used the conductometric titration method to determine total carboxylate content on TEMPO-oxidized cellulose and on TEMPO-oxidized cellulose further oxidized with sodium chlorite [22]. Sodium chlorite can oxidize aldehyde groups into carboxylate groups even without the presence of a catalyst such as TEMPO. By subtracting the carboxylate content of the TEMPO-oxidized cellulose from that of the TEMPO-cellulose further oxidized with sodium chlorite, Saito and Isogai found the aldehyde content of the TEMPO-cellulose.

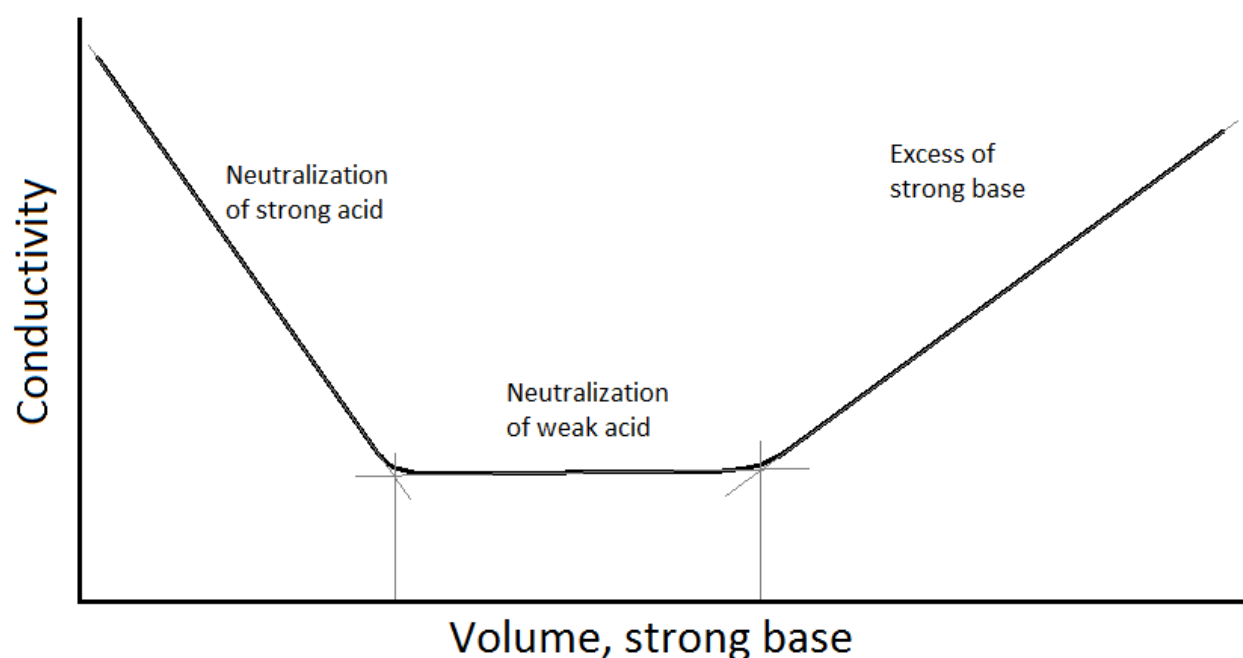


Figure 1.8.1: Typical conductometric titration curve when adding a strong base (e.g. NaOH) to a mixture of strong (e.g. HCl) and weak (e.g. HAc) acids. First, the conductivity decreases as the hydroxide ions neutralize the strong acid and forms a neutral water molecule. Each proton is replaced by an equally charged cation from the base, but these are larger than the protons and hence move more slowly, thereby decreasing the conductivity of the solution. When the strong acid is neutralized, the hydroxide ions will start attacking the non-dissociated protons of the weak acid. Since the non-dissociated weak acid, as well as the resulting water molecule and salt form of the acid are neutrally charged, the conductivity is approximately constant in the region where the weak acid is neutralized. After the weak acid is completely neutralized, both the cation and the anion of the base will contribute to a sharp increase in the conductivity of the solution, as base is added in excess.

During conductometric titration, the conductivity [S/m] in a solution with excess of acid is plotted as a function of volume of added base. A typical conductometric titration curve, with conductivity plotted as a function of volume of an added strong base, can be seen in Figure

1.8.1. As described in the figure text, the area where the conductivity is approximately constant corresponds to the volume of base needed to neutralize the weak acid; in this project being the carboxylate groups on the oxidized MFC. For this method to be applicable, the carboxylate groups must be on their protonated acid form, which is done by lowering the pH with HCl to beneath the pK_a values of the carboxylate groups. Two assumptions are made in the conversion from volume of base to number of carboxylate groups. First; that every hydroxide ion from the added base neutralizes one carboxylate group. Second; that no carboxylate groups are neutralized in the area with the large negative gradient and that none are left in the area with the large positive gradient. To further convert the difference in carboxylate content into aldehyde content, it must be assumed that all aldehyde groups are oxidized to carboxylate groups by the added sodium chlorite, and that all residues from acetic acid added during the oxidation reaction are removed before the conductometric titration. For equations for calculating carboxylate concentrations and degree of oxidation (DO), see Appendix A.

1.8.2 Macroscale characterization

As thoroughly discussed by Chinga-Carrasco, fibrillation of cellulose fibers produces a material that may be inhomogeneous (depending on pre-treatment, pressure during homogenization and number of passes through the homogenizer) [17]. Even MFC made of fibers pretreated with e.g. TEMPO-mediated oxidation can contain fragments of larger structures after several passes, as can be seen in Figure 1.8.2. The nanoscale width dimensions of the microfibrils may lead to a biased characterization focusing on these structures, while disregarding the possible presence of larger structures that may contribute to the properties (e.g. strength and elasticity) of the MFC material. A thorough assessment of an MFC material should therefore cover length scales from nm – mm [44]. High quality optical scanners can both be used to visualize whole and poorly fibrillated (residual) fibers in dried films, and to measure light transmittance, which can be correlated to fibrillation degree. The number of detectable fibrils and fibrillation degree can also be approximated using a FiberMaster [44, 45]. To image fibrils and fibril residues in the μm -size range, a laser profilometer (LP) can be used. This is a surface characterization technique, and works by the optical triangulation principle, which is explained in Figure 1.8.3. Chinga-Carrasco et al. found that coating the fibers and fiber residues with gold before LP imaging

decreased artifacts that may have been caused by internal reflections, without affecting the maximum resolution of approximately $1\text{ }\mu\text{m}$ [46].

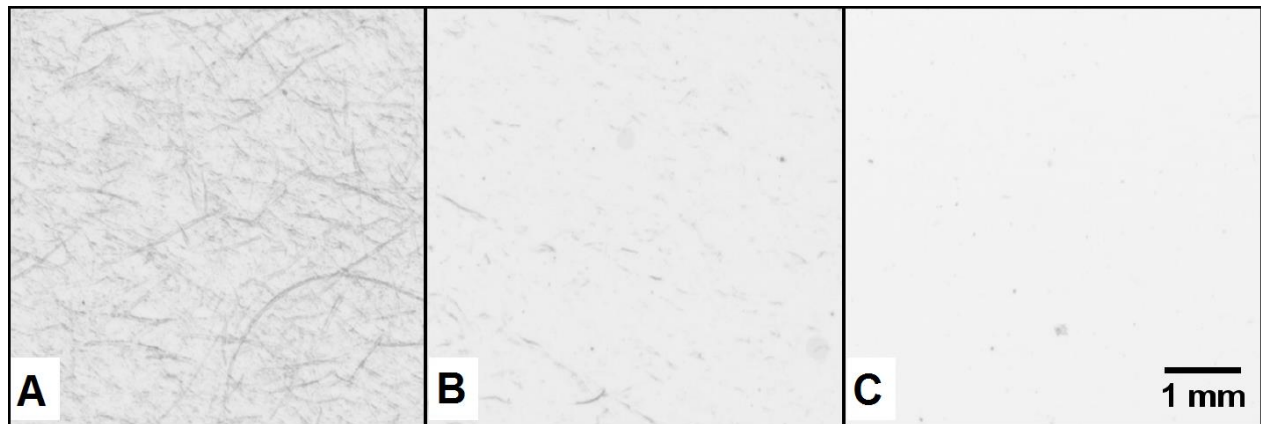


Figure 1.8.2: Scans of films prepared from TEMPO-MFC after A) three passes at 200 bar, B) three passes at 600 bar and C) five passes at 1000 bar. (Adapted from [17].)

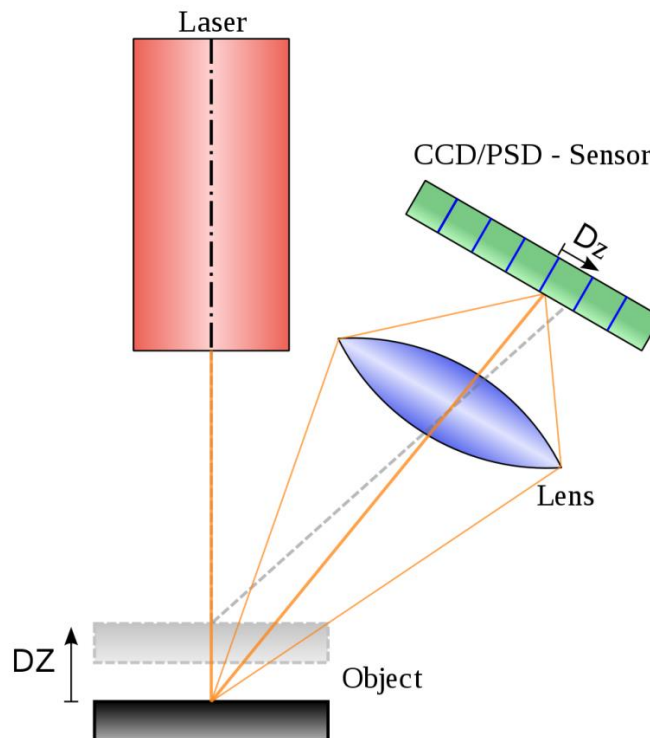


Figure 1.8.3: Optical triangulation principle, which laser profilometry is often based upon. A laser beam is projected unto the object surface. Light reflected from the surface is captured by a lens at an angle to the illumination direction, and imaged onto a light sensitive sensor such as a CCD (charge-coupled device) or a PSD (position-sensing device). The sensor or sample is scanned in two dimensions, and depth variation between adjacent measuring points are detected by an offset of the image, and saved as a height value in a topographical image. (Figure adapted from [47].)

1.8.3 Atomic force microscopy

The atomic force microscope (AFM) was introduced by Binnig et al. in 1986, and it soon became one of the most widely used small scale surface characterization techniques, due to down to atomic resolution at optimal conditions [48, 49]. An AFM works by scanning a microscopic tip over a surface and measuring deflections of the tip due to attractive and repulsive forces between the tip and a sample as described in Figure 1.8.4. Some of the greatest advantages with the AFM are no need for sample preparation, the capacity of measuring non-conductive surfaces, as well as being able to image surfaces in liquid [50].

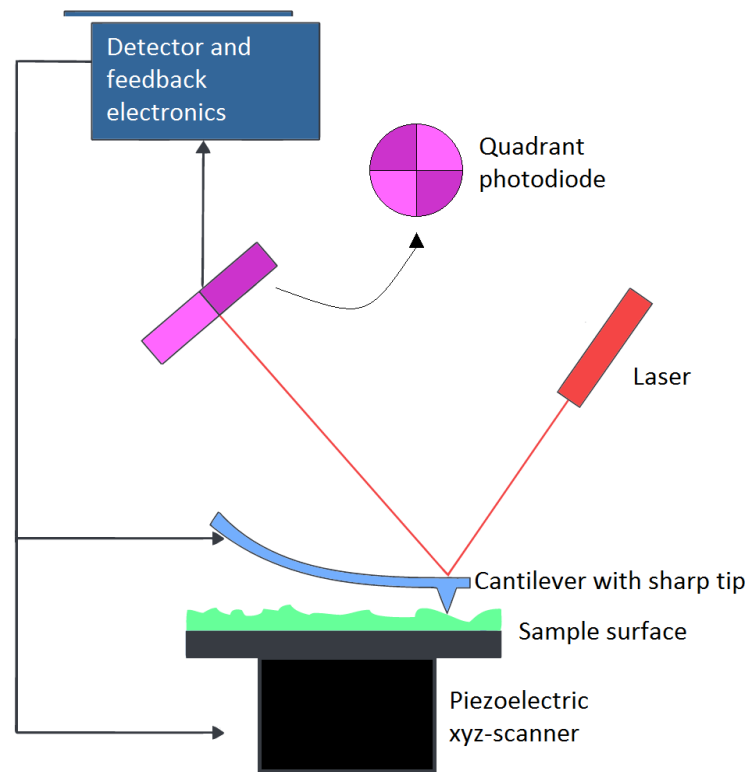


Figure 1.8.4: The basic setup of a modern AFM. A microfabricated cantilever with a small spring constant (usually in the range of 0.1 – 100 N/m) and a sharp tip (tip radius of curvature as small as possible, usually < 10nm) is scanned above a sample surface in a raster pattern. Usually the tip is stationary while the sample is mounted upon a piezoelectric scanner able of controlling movement with high accuracy in three dimensions [51]. Following Hook's law, the cantilever is deflected due to attractive and repulsive interaction forces between the tip and sample surface [52]. The detection system consists of a laser beam being reflected of the back of the cantilever and a position sensitive photodiode. When the cantilever is deflected, the laser beam is deflected as well, changing the ratio of the intensity in the different parts of the diode, leading to a change in the measured output voltage from the detector [53]. This is used by an electronic feedback system to control the interaction force and/or the tip-surface distance, which creates a topographical map of the surface.

An AFM can be run in a range of different modes; the most extensively used being tapping mode, wherein the cantilever is oscillated close to its resonance frequency. The tip only taps the surface for a very short time and the rms amplitude of the tapping cycles is kept constant by the feedback circuit [54]. A fairly new mode of operation is the peak force tapping mode, where the maximum (peak) force on the tip during each tapping cycle is kept constant instead of the amplitude [55]. The feedback loop keeps the peak force constant by changing the height of the sample, thus obtaining a topographical map of the surface. A peak force tapping cycle is described in Figure 1.8.5.

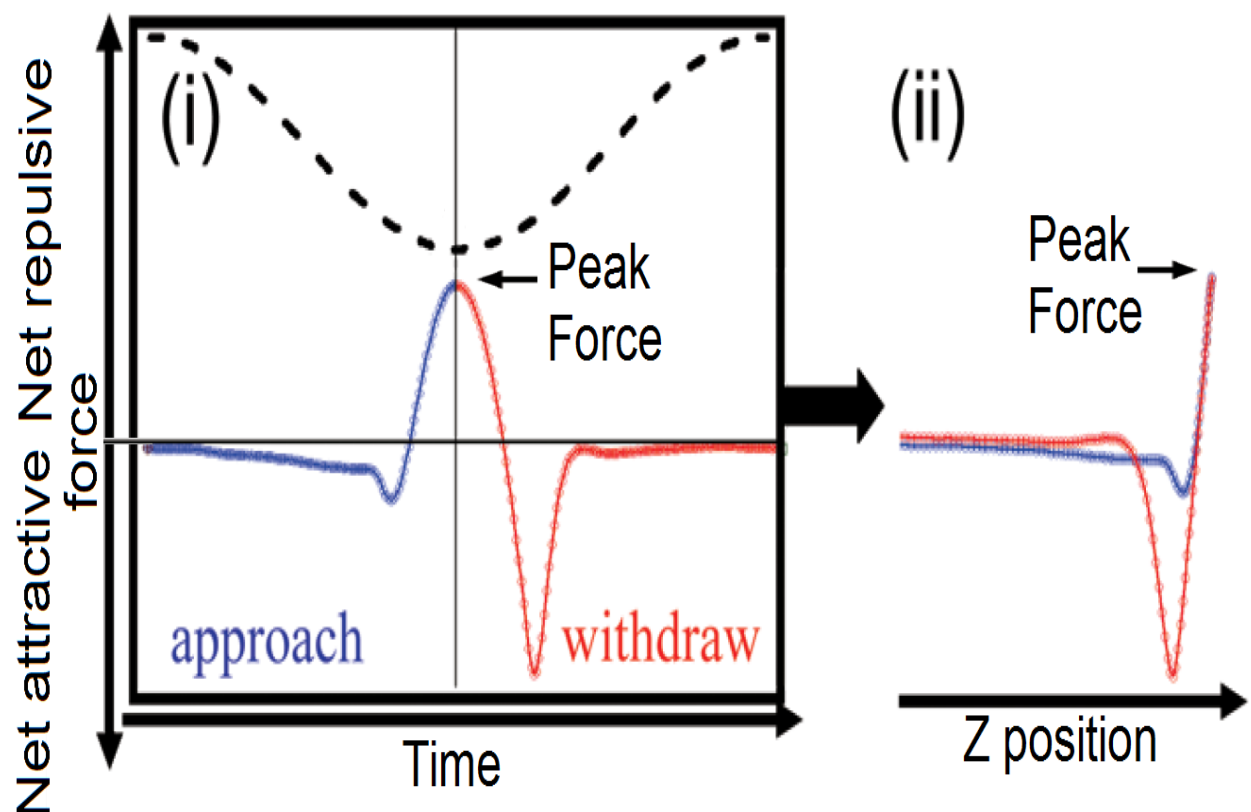


Figure 1.8.5: One oscillation cycle of the cantilever in peak force mode. i) Force as a function of time. The dashed line represents the z-position of one oscillation of the cantilever. The tip is first attracted by long-range forces (usually van der Waals, electrostatic or capillary). When these overcome the spring stiffness of the cantilever, the tip is snapped into contact with the surface. The tip stays in contact with the surface as the net repulsive forces (due to the Pauli Exclusion Principle and Coulombic repulsion between atom nuclei) increase until reaching the maximum peak force at the bottom of the oscillation cycle. As the tip is withdrawn, it will reach a maximum attractive force, which equals the adhesion force. ii) Since the cantilever oscillation frequency is controlled, and the force is measured as a function of time, the time variable can be eliminated and the force-distance curve can be directly obtained. (Adapted from [55].)

1.8.4 Scanning electron microscope

The resolution (the smallest distance at which two distinct points are discernible) of a microscope is limited by the wavelength of the electromagnetic source [56]. In vacuum, free electrons will exhibit both wave-like and particle-like properties due to wave-particle duality. This is used in the field of electron microscopy (EM), where an electron gun is used to create a beam of free electrons. The energy, and thereby the velocity and wavelength of the particles depend on the acceleration voltage (V_{acc}); the higher V_{acc} , the smaller the wavelength. Electrons can have wavelengths down to the picometer scale, thereby yielding theoretical resolutions approximately 100 000 times higher than optical microscopes (resolution of approximately $0.2\ \mu\text{m}$ [56]). There are several types of electron sources, with field emission (FE) guns yielding the highest resolutions while also being most expensive. There are two major classes of EM: transmission electron microscope (TEM) and scanning electron microscope (SEM). The basic schematic of the latter can be seen in Figure 1.8.6. The electron beam is collected and focused to a small spot by a set of electromagnetic lenses, and scanned in a raster pattern across the sample surface. The electrons will interact with the atoms of the sample, yielding different types of signals that are detected by different detectors, as seen in Figure 1.8.6. The impinging electrons can knock electrons of sample atoms. These secondary electrons (SE) will have much smaller energies than the impinging electrons, and can thus only escape from the topmost surface of the sample. Alternatively, the impinging electrons can be backscattered by sample nuclei, thus yielding the higher energy backscattered electron (BSE) signal. The interaction with the sample atoms will also cause excitation and de-excitation of electrons in the atomic orbitals, yielding x-rays with spectra characteristic of the sample material. Since the SE signal only escapes from the sample surface, SE imaging will yield high spatial resolution and high topographic contrast. Due to the tilted angle between the SE detector and sample surface, more electrons will reach the detector from areas facing towards the detector, thus creating a shadow effect. In high-vacuum imaging mode, samples for regular SEM imaging cannot contain volatile substances such as water. If the sample contains much material with low conductivity the surface can be coated with a thin layer of a conductive material to avoid charge

accumulation in the sample. However, modern SEM offers the capability of low-vacuum and low-voltage imaging, thus reducing the material conductivity requirements.

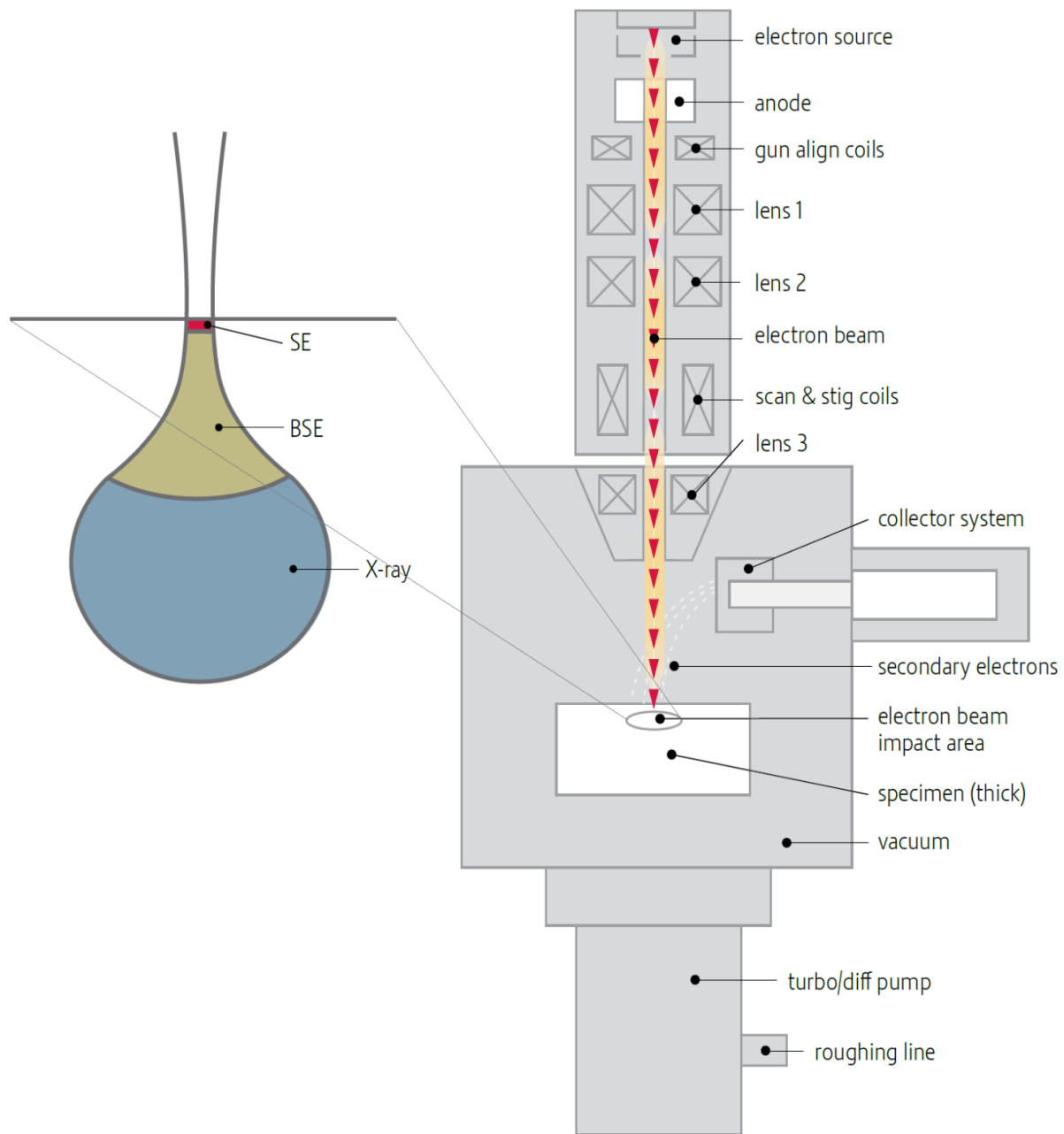


Figure 1.8.6: Basic schematic of a SEM: The electrons from the electrons source are collected and aligned to an electron beam by electromagnetic lenses, and scanned in a raster pattern over the sample surface. In each spot, the electron beam interacts with the sample material and different signals are emitted. Secondary electrons (SE) have the lowest energy and are thus only emitted from the top surface. The resolution depends on the size of the electron beam spot on the surface, and on the volume of interaction from where the signal is emitted. The latter depends on both the acceleration voltage and the material composition of the sample. (Adapted from [56].)

2 Experimental

2.1 Reagents

All water used as a reagent or dilutant during this project was of Milli-Q quality (Elga USF Maxima, resistivity 18.2 M Ω cm), unless otherwise stated. All chemical agents were purchased from Sigma Aldrich and were of laboratory-grade quality, unless otherwise stated. To compare two simple diamines with different linker-lengths, ethylenediamine (EDA) and hexamethylenediamine (HMDA) were chosen as crosslinkers. Melamine was also chosen as a crosslinker due to its successful Schiff-base formation with dialdehyde cellulose lyocell fibers as reported by Han et al. [23]. Melamine, HMDA and EDA were dissolved in MQ-water to 0.005 g/ml, as melamine did not completely dissolve at higher concentrations than this. EDA and HMDA were also dissolved in MQ-water to concentrations of 0.05 g/ml and 0.15 g/ml. The solid content of the MFC suspensions (% w/w MFC) was measured using a HR73 Halogen Moisture Analyzer (Mettler Toledo). For simplicity reasons, the mass percentage of MFC in the suspensions and gels will be given only as percentage for the remainder of this thesis.

2.2 Preparation of MFC

The processes described in this subsection were performed by engineers at PFI, two months prior to the startup of the project. Kraft pulp from softwood was added at 1.33% w/w to a solution of 1.67×10^{-3} g/ml sodium bromide (NaBr) and 1.67×10^{-4} g/ml TEMPO (2,2,6,6-tetramethylpyperidine-1-oxy radical) in DI water. The reaction was started by adding 13% sodium hypochlorite (NaClO) to a concentration of 3.8 mmol NaClO/g cellulose. The reaction lowered the pH by the selective oxidation of C6-hydroxy groups to aldehyde groups and further into carboxylate groups, as described in Section 1.4. The pH of the solution was measured continuously, and 0.5 M sodium hydroxide (NaOH) was added to keep the pH constant at 10.5. The reaction was deemed done when the pH stopped decreasing. The pH was then adjusted to seven by adding 0.5 M hydrochloric acid (HCl), before the fiber mass was cleaned by filtration using DI water. The introduction of the negatively charged carboxylate groups disrupted the hydrogen-bonds linking the nanofibrils together, thereby easing the fibrillation process. The

TEMPO-treated cellulose mass was run one pass through a homogenizer (Rannie 15 type 12.56X9), operated at 1000 bar. The solid content of the resulting MFC suspension was measured as 0.98%. Although the term MFC strictly only refers to the fibrillated cellulose fibers, the resulting microfibrillated cellulose suspension is termed MFC in the rest of this paper for simplicity reasons.

2.3 Oxidation of remaining aldehyde groups using sodium chlorite

As described in Section 1.8.1, a stronger oxidation agent than sodium hypochlorite, such as sodium chlorite (NaClO_2), can be used to further oxidize aldehyde groups to carboxylate groups, even in the absence of a catalyst such as TEMPO. Following a procedure similar to the one described by Saito and Isogai [22], 102.04 g MFC (0.98%) was measured into a beaker, and 10 ml 5 M aqueous acetic acid (diluted from >99.8% pure glacial acetic acid, Romil Ltd) and 0.91 g sodium chlorite was added to the sample. Using a magnetic stirrer at 1000 rpm, the sample was then stirred at room temperature for 48 h. The sample was cleaned in a Spectra/Por 4 dialysis membrane of regenerated cellulose (MWCO: 12 000-15 000 Da, Spectrum Laboratories Inc, Rancho Dominguez, CA, USA) by immersing the membrane in MQ water for 24 hours. Further cleaning was done by distributing the sample into 12 ml test tubes and centrifuging these five times at 2700 rpm for 10 minutes at 20° C using a Heraeus Labofuge 400R (DJB Labcare Ltd). The supernatant was replaced with MQ water after each centrifugation. Another parallel was oxidized three months after the first parallel, using the same amounts and the same reaction parameters as used during the first parallel. This sample was not cleaned using dialysis, only with centrifugation.

2.4 Measuring carboxylate and aldehyde content

As explained in Section 1.8.1, conductometric titration has been found to be the most accurate and reproducible method for determining total carboxylate content in MFC [42]. Following a conductometric titration procedure similar to the one described by Saito and Isogai [22], the carboxylate content was determined in the MFC and in both parallels of the sodium chlorite-oxidized MFC. MFC containing 0.1 g solid content was weighed out and 16.6 ml 0.01 M sodium chloride (NaCl) was added to each replicate. The total mass was increased to 200 g by adding

MQ water, and the pH was adjusted to ~2.8 by adding 0.1 M HCl, to ensure the protonation of the carboxylate groups. The sample was stirred continuously by a magnetic stirrer, and 0.04 M NaOH was added at a rate of 0.1 ml/min using an automatic titrator (Metrohm 902 Titrando). The conductivity of the sample was automatically measured at increments of 0.1 ml for the first parallel and 0.01 ml for the second parallel using a Metrohm 856 Conductivity Module, and the data was recorded by Tiamo® Titration Software. The conductivity was plotted as a function of volume of added NaOH and processed using Microsoft Excel 2010 software. By calculating the volume of added NaOH at the intercepts between the linear regression lines of the resulting plot, the volume of base needed to neutralize the weakly acidic carboxylate groups on the fibrils was found. Assuming that each added molecule of NaOH within this range neutralized exactly one carboxylate group, the relative amount of carboxylate groups in the MFC and in the sodium chlorite-oxidized MFC was calculated by the equations in Appendix A. Assuming all aldehyde groups were oxidized to carboxylate groups by the sodium chlorite, subtracting the carboxylate content of the MFC from the carboxylate content of the sodium-chlorite oxidized MFC then yielded the aldehyde content of the MFC.

2.5 Qualitative gelling experiment

A gelling experiment was designed to qualitatively investigate the crosslinking properties of the di- and triamines, and if possible to narrow down the optimal concentrations of crosslinkers per unit mass of MFC. It was assumed that 0.25% MFC would yield a sample that was thin enough to visually observe a change in viscosity due to Schiff-base formation. MFC (0.98%) was measured into 12 ml test tubes, 0.005 g/ml EDA and HMDA solutions were added in different amounts (see Table 2.5.1), and MQ-water was added to a total mass of 12 g. Test tubes were also prepared with melamine solution (0.005 g/ml), approximately with similar total amounts of amine groups as for EDA and HMDA. The crosslinker solutions were added using a P1000 micropipette with volume increments of 0.005 ml. The content of the test tubes were thoroughly mixed by stirring, and the test tubes were placed in a water bath (OLS200, Grant Instruments Ltd) at 80° C for approximately 20 hours. The test tubes were tilted, and the difference in viscosity was qualitatively compared.

Table 2.5.1: An overview of the different concentrations of the three crosslinkers used in the qualitative gelling experiment, when preparing the films and when preparing the cast gels, respectively. E = EDA, H = HMDA. The number after the capital letters describe the ratio between amine and aldehyde, calculated from the initially determined aldehyde content. 2picbor = 2-picolineborane, about 1.22 mmol/g MFC, dissolved in 96% ethanol, 0.025 ml/g total mass of sample. The calculated dry substance contents were 0.0300 g MFC in each test tube, 0.1135 g MFC in each film and 0.0290 g MFC in each cast gel (assuming perfectly filled casting molds), respectively.

Sample code	Crosslinker concentration [mmol/g MFC] ^[a]	MFC (w/w), qualitative gelling	MFC (w/w), films (pre-drying)	MFC (w/w), cast gels
MFC	n/a	0.25 %	0.25 %	n/a
E1	6.14×10^{-2}	0.25 %	0.25 %	0.80 %
E2.5	1.52×10^{-1}	n/a	n/a	0.80 %
E5	3.04×10^{-1}	0.25 %	n/a	0.80 %
E10	6.09×10^{-1}	0.25 %	n/a	0.80 %
E50	3.04	0.25 %	n/a	0.80 %
E100	6.08	0.25 %	0.25 %	0.80 %
H1	6.08×10^{-2}	0.25 %	0.25 %	0.80 %
H2.5	1.52×10^{-1}	n/a	n/a	0.80 %
H5	3.04×10^{-1}	0.25 %	0.25 %	0.80 %
H10	6.12×10^{-1}	0.25 %	0.25 %	0.80 %
H50	3.05	0.25 %	0.25 %	0.80 %
H100	6.09	0.25 %	0.25 %	0.80 %
H1 + 2picbor	6.08×10^{-2}	n/a	n/a	0.80 %
H2.5 + 2picbor	1.52×10^{-1}	n/a	n/a	0.80 %
H5 + 2picbor	3.04×10^{-1}	n/a	n/a	0.80 %
H10 + 2picbor	6.12×10^{-1}	n/a	n/a	0.80 %
H50 + 2picbor	3.05	n/a	n/a	0.80 %
H100 + 2picbor	6.09	n/a	n/a	0.80 %

^[a] These values were calculated from the actual added volume [ml] of crosslinker-solution [g/ml]. Due to the micropipette utilized, the added volume had to be approximated to the nearest 0.005 ml, which induced slight variations in relative amount of crosslinkers between samples that should ideally have contained equal amine to aldehyde ratios.

2.6 Film preparation

Using the results from the qualitative gelling test as guidance, films were prepared with different concentrations of crosslinkers, as can be found in Table 2.5.1. The films were prepared to have a final grammage of 20 g MFC/m². MFC (0.98%), different amounts of 0.005 g/ml crosslinker solutions and MQ-water were added to beakers and stirred using a magnetic stirrer. The crosslinker solutions were added using a P1000 micropipette with volume increments of 0.005 ml. The samples were prepared at a final solid content of 0.25% MFC, as samples with higher concentrations than this had previously been found to lead to inhomogeneous drying and subsequently uneven thickness in the films. Using disposable pipettes, 45.4 g sample was applied to disposable petri dishes with an area of 0.005675 m² per dish. As no visible gelling was observable after 24 hours in room temperature, the samples were placed in a heating cabinet (ULE 600, Memmert GmbH & Co) at 75° C for 24 hours with the lids on the petri dishes to avoid evaporation. The samples were then dried at room temperature for 5 days, until all moisture had evaporated from all films.

2.7 Gel casting

Casting molds of stainless steel (custom made at the Precision Mechanics Engineering Workshop, NTNU) for casting gels for Texture Analyzer analysis, were borrowed from the Department of Biotechnology, NTNU. The casting molds were comprised of small cylinders, 18 mm high and 16 mm in inner diameter, which could be screwed into tracks in a stainless steel well plate. The setup also contained silicone plates for sealing the bottom and tops of the cylinders and flat, heavy plates of stainless steel for fastening the silicone seals. This setup had to be modified, as the gels did not stick to the stainless steel, and hence were difficult to remove from the well plate without breaking. The final setup can be seen in Figure 2.7.1. A dry content of 0.80% MFC was chosen for the gels, as this was approximately the highest concentration obtainable after adding the largest amounts of crosslinker-solutions. MFC (0.98%), different amounts of crosslinker solutions (see Table 2.5.1) and MQ-water were added to beakers and stirred using a magnetic stirrer.

2-picoline-borane was chosen as a suitable reduction agent, since it should reduce the Schiff-bases to amines without reducing non-reacted aldehyde groups. Its non-toxicity made it preferable to other similar reducing agents such as sodium cyanoborohydride. The amount of 2-picoline-borane necessary for obtaining a concentration of 1.22 mmol/g MFC was dissolved in 96% ethanol, 0.025ml/g total mass of sample, which was added to the samples subsequently to the crosslinker-solutions. This concentration was approximately ten times higher than the initially determined aldehyde-concentration. It was assumed to be large enough to reduce all successfully formed Schiff-bases, while also conserving the amount of 2-picoline-borane, which was only available in bottles containing 5 g (Sigma Aldrich).

After the samples had been stirred for approximately 5 minutes, they were dispensed with positive/convex menisci into the casting molds. The silicone plates were put onto the casting molds and sealed by tightening the steel top plates as shown in Figure 2.7.1. The casting molds were placed overnight in a heating cabinet (ULE 600, Memmert GmbH & Co) at 80° C, the time varying between approximately 16.5 hours and 20.5 hours. Young's modulus was measured as soon as possible after removing the gels from the heating cabinet. One series of the H50 gels was prepared for time-lapsed measurements of Young's modulus. The preparation procedure was the same as described above, but gels were taken out of the heating cabinet after approximately 1, 3, 5, 8 and 24 hours, respectively.



Figure 2.7.1: The setup with the casting molds of stainless steel used in this project for preparing cylindrical gels of crosslinked MFC. The molds were filled with positive/convex menisci to obtain gels with equal volume, as the surplus of sample was pressed out of the molds when the silicone seals were tightened.

2.8 Dynamic measurements by rheometer

Using a rheometer (Stresstech, Reologica Instruments AB, Sweden), dynamic measurements were performed on MFC without crosslinkers at 0.98%, 0.80% and 0.50% MFC. Dynamic measurements were also performed with 3.05 mmol HMDA/g MFC at 0.80% MFC and 6.12×10^{-1} mmol HMDA/g MFC at 0.50% MFC. The HMDA-solution was added to the MFC and mixed using a magnetic stirrer. To remove air introduced by the stirring, the sample was placed in a simple vacuum chamber and degassed for approximately 2 – 3 x 15 minutes using a diaphragm vacuum pump (MZ 2C, Vacuubrand GmbH + Co KG). All samples were kept at room temperature until being added to the rheometer. Cone-plate measurement geometry (cone = 4° gradient, diameter = 35 mm, gap = 150 μ m at center) was used for all measurements. The rheometer during a measurement can be seen in Figure 2.8.1. Zero gap was performed at 20° C, prior to application of sample. Approximately 1.5 ml sample was applied to the bottom plate and excess sample was removed.

2.8.1 Amplitude sweep

To find the viscoelastic linear regime (VLR) of the samples, amplitude sweeps were performed by logarithmically increasing the strain from 0.001 – 1. The frequency and temperature were kept constant at 1 Hz and 20° C, respectively. To investigate how quickly or if the structure of the samples would resettle after disruption at the highest strains, for some samples the strain was instantly decreased to 0.01 after having reached 1, and kept constant for > 10 minutes.

2.8.2 Frequency sweep

To investigate whether the samples acted like gels or liquids at relevant frequencies, frequency sweeps were performed by logarithmically increasing the frequency from 0.01 – 10 Hz. This also yielded the dynamic viscosity of the samples. The strain and temperature were kept constant at 0.01 and 20° C, respectively.

2.8.3 Steady state viscosity

To investigate the structure of the samples and whether they followed the Cox-Merz rule, the steady state viscosity of the samples was measured while increasing the shear rate from < 0.1 – 60 s^{-1} . This was the only dynamic rheological measurement performed by constantly rotating

the probe in one angular direction; all other measurements were performed at oscillatory movement.

2.8.4 Small strain oscillatory measurements (temperature sweep)

To investigate whether the structure of the samples were temperature dependent, as well as to induce crosslinking in the samples with HMDA, the temperature was increased to 80° C and kept constant for 60 minutes before being decreased back to the initial temperature of 20° C. The temperature gradient during the increase/decrease was $\pm 4^{\circ}$ C/min. The strain and frequency was 0.01 and 1 Hz, respectively. The sample was covered with silicone oil (Dow Corning®, 200/10 cS fluid, UK) to prevent evaporation during the measurements. To investigate if the crosslinking was dependent on high temperatures to initiate, one measurement was performed with the temperature constant at 20° C. To investigate if the gel stabilized at a certain plateau, one measurement was performed where the temperature was kept at 80° C for >10 hours.

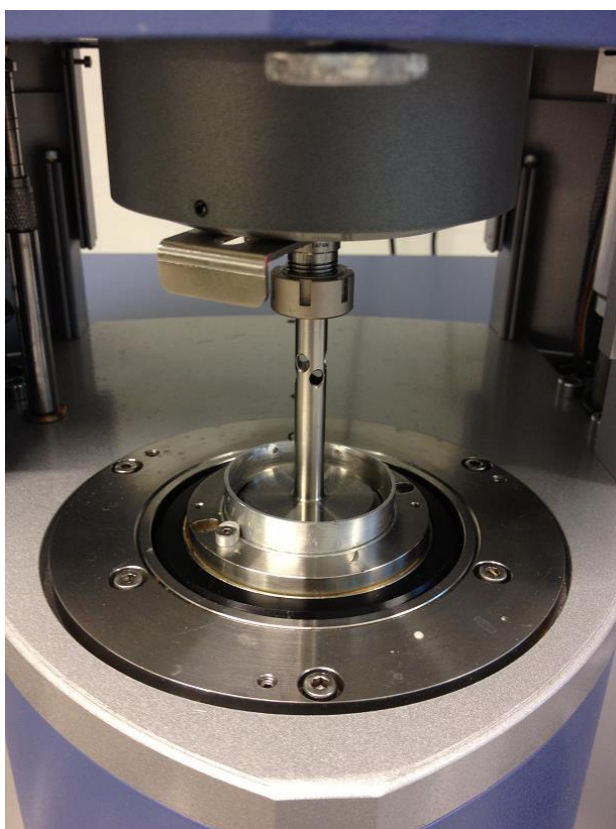


Figure 2.8.1: The rheometer with cone-plate measuring geometry during a measurement. During dynamic oscillatory measurements, the cone is oscillating back and forth in an angular movement, usually at small enough amplitudes to not disrupt the structure of the samples (i.e. within the VLR).

2.9 Longitudinal measurements by texture analyzer

To determine Young's modulus of the cylindrical cast gels, a texture analyzer (TA) (TA.XT.-Plus Texture Analyzer, Stable Micro Systems, Surrey, UK) was used to perform compression measurements. The gels were decanted directly from the casting molds onto the stationary bottom plate of the apparatus, and the diameter at the top and the height of the gels were measured using a digital caliper. A cylindrical stainless steel probe (p/35, diameter = 35 mm) was used to compress the gels 2 mm in longitudinal direction, after an initial trigger force of 1 g was reached. The compression speed was 0.1 mm/s, and the compression force was measured by a 1 kg load cell. To measure the course up till and after break, two parallels (H50 and E50, see Table 2.5.1) were compressed 8 mm. The data was recorded and analyzed using the respective software (Exponent v5.1.2.0) of the apparatus. The compression force was plotted as a function of deformation length, and linear regression was performed on the data points from 0.15mm – 0.30 mm compression to find the gradient in the linear region. Young's modulus was calculated by multiplying the gradient ($F/\Delta l$) with the initial height of the gels and dividing by their cross sectional area, according to the relationship in Table 1.7.1.

2.10 Micro-topographical characterization by laser profilometry

Samples of approximately 1 cm × 1 cm were cut from all of the films found in Table 2.5.1 and attached to object glass using double sided tape. The samples were oriented with the same side facing upwards as when drying the films, as the side facing downwards was artificially smoothed by the surface of the petri dishes. The samples were coated with gold for 120 seconds using an Agar Automatic Sputter Coater (Agar Scientific, UK) to increase the reflectivity of the surface and thus reduce artifacts. An automated laser profilometer (LP) (Lehmann, Lehman Mess-Systeme AG, Baden-Dättwil, Germany) was utilized to acquire ten LP topography images from each sample. The area of each image was 1 mm × 1mm, with an image size of 1000 × 1000 pixels, yielding a lateral resolution of 1 μ m. The vertical resolution of the LP system was 10 nm. The images were analyzed using the SurfCharJ plugin in the Java-based public domain program ImageJ [46]. The SurfCharJ plugin was used to horizontally align the images by subtracting a regression plane from the surface, before calculating the root-mean-square deviation surface

roughness (Sq) of each image without further filtering. The average Sq-value of each sample was calculated and plotted as a function of crosslinker concentration.

2.11 Nano-topographical characterization by atomic force microscopy

Samples of approximately 1 cm × 1 cm were cut from all of the films found in Table 2.5.1 and attached to magnetic sample holders. The samples were oriented with the same side facing upwards as when drying the films. An atomic force microscope (AFM) (diMultiMode V) with a NanoScope V controller (Bruker Corporation, previously Veeco Instruments Inc., Santa Barbara, CA, USA) was used to image the samples. All images were acquired using ScanAsyst mode in air at room temperature. This mode is based on Veeco's Peak Force Tapping mode, which controls the maximum force on the tip, and it continuously monitored the image quality and automatically made the appropriate parameter adjustments [55]. The AFM cantilevers were triangular with nominal spring constant values of 0.4 N/m (SCANASYST-AIR, Bruker Corporation). The size of each captured area was 2000 nm × 2000 nm, with an image size of 1024 × 1024 pixels, yielding a lateral resolution of < 2 nm. The scan rate was approximately 0.8 Hz per line. The SurfCharJ plugin in ImageJ was used to horizontally align the images by subtracting a regression plane from the surface, before calculating the root-mean-square deviation surface roughness (Sq) of each image. The images were analyzed with and without a FFT filter, which applied a difference of Gaussian bandpass filter, thus suppressing structures above and below a predefined size [46]. The filtered bands were 0 – 5 nm, 5 – 10 nm, 10 – 20 nm, 20 – 40 nm, 40 – 80 nm, and 80 – 160 nm. One wavelength is twice a band length, thus multiplying the filtered bands with 2 yielded the filtered wavelengths. The Sq-values were plotted as functions of crosslinker concentration.

2.12 Fiber and fibril size distribution (FiberMaster)

The relative amount of residual fibers in the MFC was estimated using a STFI FiberMaster (AB Lorentzen Wettre). The FiberMaster worked by guiding a diluted MFC suspension through a flow cell while capturing fine (6 μm/pixel) and coarse (26 μm/pixel) resolution images with a two-CCD-camera system [45]. The images were processed and analyzed by the FiberMaster for a number of fiber characteristics, such as average fiber length and diameter. The MFC was

diluted to 0.25% and a known volume was run through the FiberMaster. Knowing the density of cellulose, the average lengths and diameters were used to estimate the average mass of a fiber, \overline{w} . The relative amount of residual fibers was then calculated by Equation 2.12.1:

$$\text{residual fibers (\%)} = \frac{\overline{w}}{w_s} \times n \times 100 \quad (2.12.1),$$

where w_s is the total mass of cellulose in the assessed sample and n is the detected number of fibers. (For details, see [45].)

2.13 Freeze drying of gels

Cast gels (H1, E1, H50 and E50; see Table 2.5.1) were placed onto a metal plate with approximately 1.5 cm high edges, still in the cylindrical casting molds. MFC was diluted to 0.80% and pipetted into empty casting molds placed on the same metal plate. Liquid nitrogen was then poured directly onto the plate, as it was hypothesized that the samples would freeze almost instantaneously due to the direct contact with the metal plate and metal casting molds, thereby limiting the time for ice crystal growth. The metal plate with the samples was placed in a freeze dryer (LyoPro 6000 with an AC300 chamber, Heto-Holten A/S, Denmark) for 8 days.

2.14 Scanning Electron Microscopy (SEM)

Films with high relative amounts of crosslinkers (E100, H50 and H100; see Table 2.5.1) as well a pure MFC film were imaged by a Hitachi S-5500 scanning (transmission) electron microscope (S(T)EM). Small pieces of the films were attached to appropriate sample holders by double sided conductive carbon tape, oriented with the same side facing upwards as when drying the films. To improve the signal and to avoid charge accumulation, a 15 nm thick layer of gold was sputtered onto the samples using a sputter coater (208 HR B, Cressington). The films were imaged with a secondary electron detector at an acceleration voltage of 2.00 kV.

Pieces of freeze dried gels (H1, H50, E1, E50 and pure MFC) were imaged by a Hitachi S-3000N scanning electron microscope (SEM). Pieces from the edges which had been facing against the casting molds, as well as pieces with the cross sectional area facing upwards, were attached to appropriate sample holders by double sided conductive carbon tape. To improve the signal and

to avoid charge accumulation, the samples were coated with gold for 45 seconds using an Agar Automatic Sputter Coater (Agar Scientific, UK). The films were imaged with a secondary electron detector at an acceleration voltage of 5.00 kV. The pieces from the edges of the freeze-dried gels, pre- and post-coating, can be seen in Figure 2.14.1.



Figure 2.14.1: Pieces from the edges of the freeze-dried gels, mounted with carbon tape on SEM sample holder, pre- (left frame) and post-coating (right frame) with gold for 45 s.

2.15 Water reabsorption

Freeze dried gels (E50, H50 and pure MFC) were weighed on a laboratory scale (Mettler AT201, Mettler-Toledo) with a readability range of 0.0001 g. The gels were then immersed in MQ-water and taken out at different times to be weighed. Using tissue paper, secreted and surplus water was soaked up before weighing. Two replicates were weighed, one focusing on the first hour and the other on a longer time span. Using Equations 2.15.1 and 2.15.2, the moisture content (%) and water absorption (%) was calculated:

$$\text{moisture content (\%)} = \frac{W_w - W_d}{W_w} \times 100 \quad (2.15.1),$$

$$\text{water absorption (\%)} = \frac{W_w - W_d}{W_d} \times 100 \quad (2.15.2),$$

where W_w is the weight of the wet sample and W_d is the weight of the dry sample before immersion in water. (For details, see [57].)

2.16 pH measurements

The measurements described in this sub-section were performed with a pH-meter (inoLab pH Level 2, WTW GmbH & Co, Germany). The pH-meter was calibrated before use with buffers of pH 7.01 and pH 4.01. The probe was rinsed with MQ-water between each measurement. The pH-values of 0.005 g/ml EDA and HMDA solutions were measured. Eight gels (2×E10, 2×E10 + 2picbor, 2×H10 and 2×H10 + 2picbor; see Table 2.5.1]) were freshly prepared and immersed in separate containers with 100 ml MQ-water. One replicate of each gel was treated carefully to keep the gels intact, while the other replicate was dissolved completely using a magnetic stirrer. The pH was measured immediately after immersion or dissolution, and at increased times after this. It was calculated that the amount of 0.005 g/ml crosslinker-solution in one gel was approximately 0.410 ml in the gels with HMDA and 0.210 ml in the gels with EDA. These volumes of the respective crosslinker-solutions were added to 100 mL MQ-water, and the pH of the solutions was measured.

3 Results

3.1 Conductometric titration

One of the major issues when working with MFC is cleaning the sample. Cellulose fibers can easily be cleaned using filtration, but MFC with its large aspect ratios, large total surface area and ability to pack very densely quickly clogs conventional paper filters. To measure carboxylate content in the MFC oxidized with sodium chlorite, all traces of acetic acid had to be removed. Cleaning the MFC only with dialysis yielded unrealistically high carboxylate values (4.35 mmol/g MFC), most likely due to acetic acid residues. The MFC oxidized with sodium chlorite was therefore centrifuged as described in Section 2.3. This yielded reasonable results, as seen in Table 3.1.1, although the calculated aldehyde content was somewhat lower than expected from literature (see Table 1.5.1). An observation supporting the successful removal of acetic acid

residues was the absence of any acetic acid scent when measuring the solid content of the sample after centrifugation, in contrast to the measurement after dialysis.

Table 3.1.1: Calculations based on V_{NaOH} -values from the first conductometric titration parallel. The coefficient of variation (CV) is the ratio between the standard deviation (SD) and the average value. Due to the propagation of errors, CV became much larger for the average aldehyde than carboxylate values.

First parallel	Average	SD	CV
Sample	MFC oxidized with sodium chlorite		
Carboxylate groups [mmol/g MFC]	1.106	0.025	2.3 %
Degree of oxidation, DO	18.7 %	0.4 %	2.4 %
Sample	MFC		
Carboxylate groups [mmol/g MFC]	0.937	0.043	4.5 %
Degree of oxidation, DO	15.7 %	0.7 %	4.7 %
Sample	MFC		
Aldehyde groups [mmol/g MFC]	0.169	0.050	29.3 %
Degree of oxidation, DO	2.9 %	0.9 %	29.2 %

Note that the initially calculated aldehyde value of 0.122 mmol/g MFC, on which the ratios between amine and aldehyde naming the crosslinked samples are based upon (see Table 2.5.1), differs from the value in Table 3.1.1. This was due a simple mix-up of +/- before the y-intercept value of the increasing linear expression when calculating the interception between the constant and increasing linear expressions of the first replicate of the regular MFC. This led to an overestimation of the calculated volume of NaOH of this first replicate, which led to an overestimation of the carboxylate amount of the regular MFC, finally leading to the underestimation of the aldehyde content of the MFC. This shows how vulnerable this method is to errors introduced by the operator.

There were some limitations with the first parallel. After centrifugation, there was only enough sodium chlorite-oxidized MFC left for two replicates. Also, only two replicates were obtained from the regular MFC. These were from another project using the same MFC, and thus measured by another operator.

To investigate the repeatability of the measurements, a second parallel was oxidized with sodium chlorite and examined using conductometric titration three months after the first parallel, as described in Section 2.3. Three replicates were also measured on the regular MFC, and all measurements were recorded with ten times more data points (i.e. increments of 0.01 ml instead of 0.1 ml) than during the first parallel. Conductometric titration curves from the second replicates (which yielded values closest to average) of both sodium chlorite oxidized and regular MFC can be seen in Figure 3.1.1 and Figure 3.1.2, respectively. As can be seen in Table 3.1.2, the calculated amount of carboxylate groups was lower on both regular MFC and sodium chlorite-oxidized MFC, but the resulting aldehyde content was somewhat higher. Due to the differences between the two parallels, and because the second replicate contained one more replicate with the replicates containing ten times more data points, the average values were calculated separately for the two parallels. Values for the separate replicates can be observed in Appendix A.

Table 3.1.2: Calculations based on V_{NaOH^-} -values from the second conductometric titration parallel. The coefficient of variation (CV) is the ratio between the standard deviation (SD) and the average value. Due to the propagation of errors, CV became much larger for the average aldehyde than carboxylate values.

Second parallel	Average	SD	CV
Sample	MFC oxidized with sodium chlorite		
Carboxylate groups [mmol/g MFC]	0.991	0.030	3.0 %
Degree of oxidation, DO	16.7 %	0.5 %	3.1 %
Sample	MFC		
Carboxylate groups [mmol/g MFC]	0.810	0.030	3.7 %
Degree of oxidation, DO	13.5 %	0.5 %	3.9 %
Sample	MFC		
<i>Aldehyde groups [mmol/g MFC]</i>	<i>0.181</i>	0.042	23.4 %
<i>Degree of oxidation, DO</i>	<i>3.1 %</i>	0.7 %	23.4 %

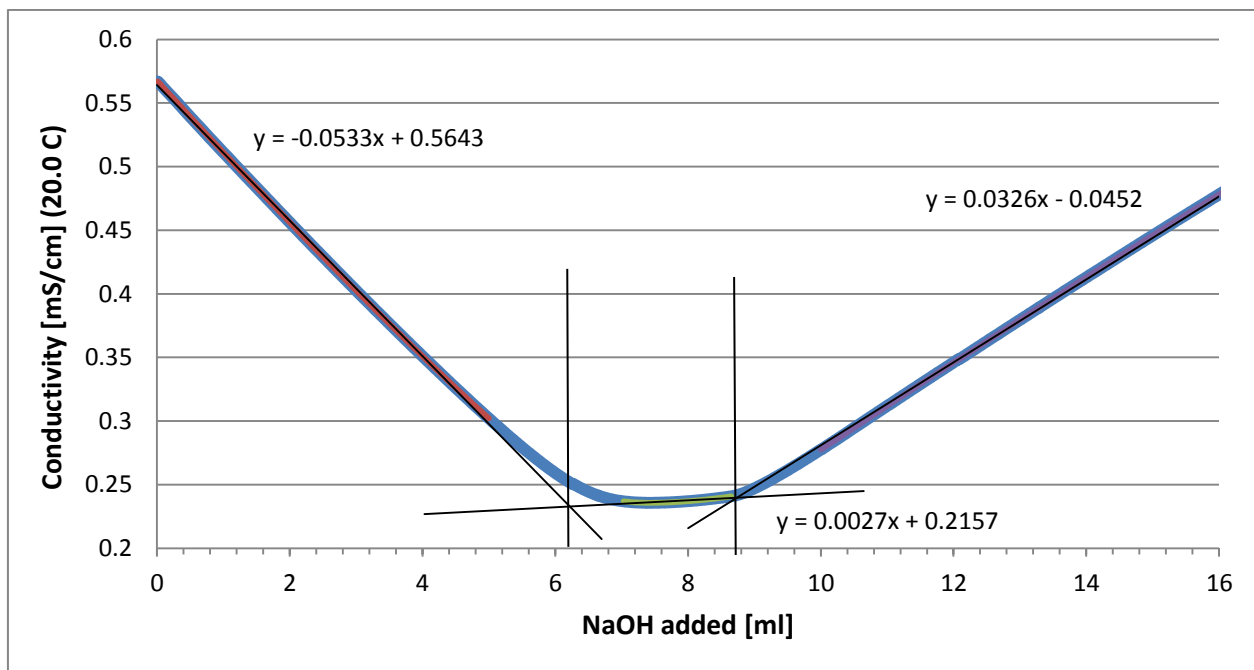


Figure 3.1.1: Conductometric titration plot of the second replicate of the second parallel of sodium chlorite-oxidized MFC. The added volume of NaOH between the two intercepts of the linear sections of the plot was used to calculate the number of carboxylate groups in the sample.

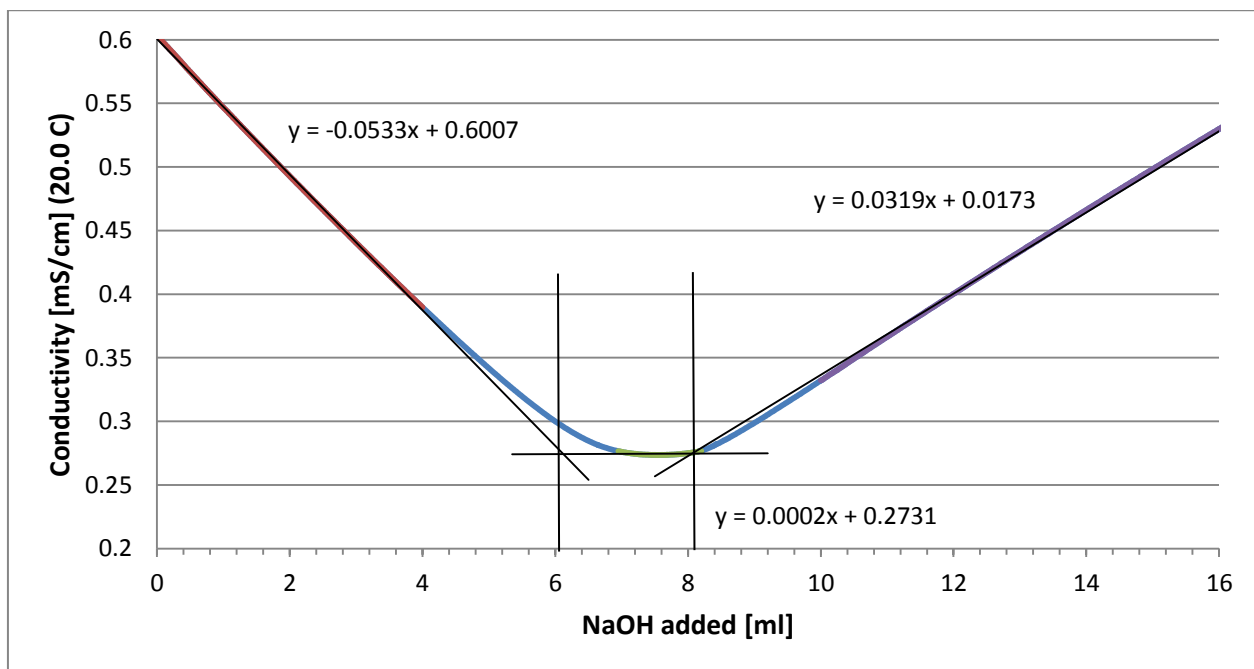


Figure 3.1.2: Conductometric titration plot of the second replicate of the second parallel of original MFC. The added volume of NaOH between the two intercepts of the linear sections of the plot was used to calculate the number of carboxylate groups in the sample. The difference in V_{NaOH} between Figure 3.1.1 and this figure is assumed to correspond to the aldehyde groups on the original MFC which are oxidized to carboxylate by sodium chlorite.

3.2 Qualitative gelling experiment

No change in either color or viscosity could be visually observed in any of the samples containing melamine, suggesting that no significant crosslinking had occurred. In the test tubes with HMDA, an increase in viscosity could be observed in sample H5 – H100 (see Table 2.5.1 for crosslinker concentrations). The viscosity seemed to correlate with the increasing concentration of HMDA, although no difference could be observed between H50 and H100. There was also a color change from the initial bluish grey of the MFC to a brownish yellow in all of the samples containing HMDA, the intensity of the color change seemingly correlated to increasing crosslinker-concentration. The same color change was observable for the samples containing EDA, although less intense. The color of the sample with highest EDA concentration (E100) seemed to correspond to sample H5. These samples also showed approximately equal viscosity, while no change in viscosity could be observed for the samples with lower EDA concentration.



Figure 3.2.1: Test tube containing 0.25% MFC and 3.05 mmol HMDA/g MFC (H50) after approximately 20 hours in a water bath at 80° C. Even containing >99.5% water, the test tube could be turned sideways and upside down without observable viscous behavior in the gel. Notice the phase separation where water has been excreted in the bottom of the test tube. Also notice the air bubbles captured in the gel matrix. These were probably introduced during the mixing of the crosslinker solution into the MFC suspension. The color change from the original slightly bluish grey to a brownish yellow seemed to correlate with the amount of HMDA.

3.3 Dynamic measurements

3.3.1 Amplitude (strain) sweeps

As can be seen in Figure 3.3.1, both storage modulus (G') and loss modulus (G'') decreased as the concentration of MFC decreased. The storage moduli were nearly constant up to a strain of approximately 0.04, yielding a linear relation between stress and strain (the viscoelastic regime, VLR) for strains ≤ 0.04 . (This limit is a matter of definition, as the steepness of the decline in storage moduli differed between the samples.) The strain was thus set as 0.01 in the remaining constant strain-controlled measurements, to ensure measurements within the VLR. Within the VLR, the average storage moduli (± 1 SD) were 274.7 ± 13.0 Pa (0.98%), 126.2 ± 2.6 Pa (0.80%) and 31.8 ± 1.0 Pa (0.50%), respectively. The storage modulus decreased even further (11.5 ± 0.6 Pa) when HMDA (6.12×10^{-1} mmol/g MFC) was added to the sample with 0.50% MFC without pre-heating the sample.

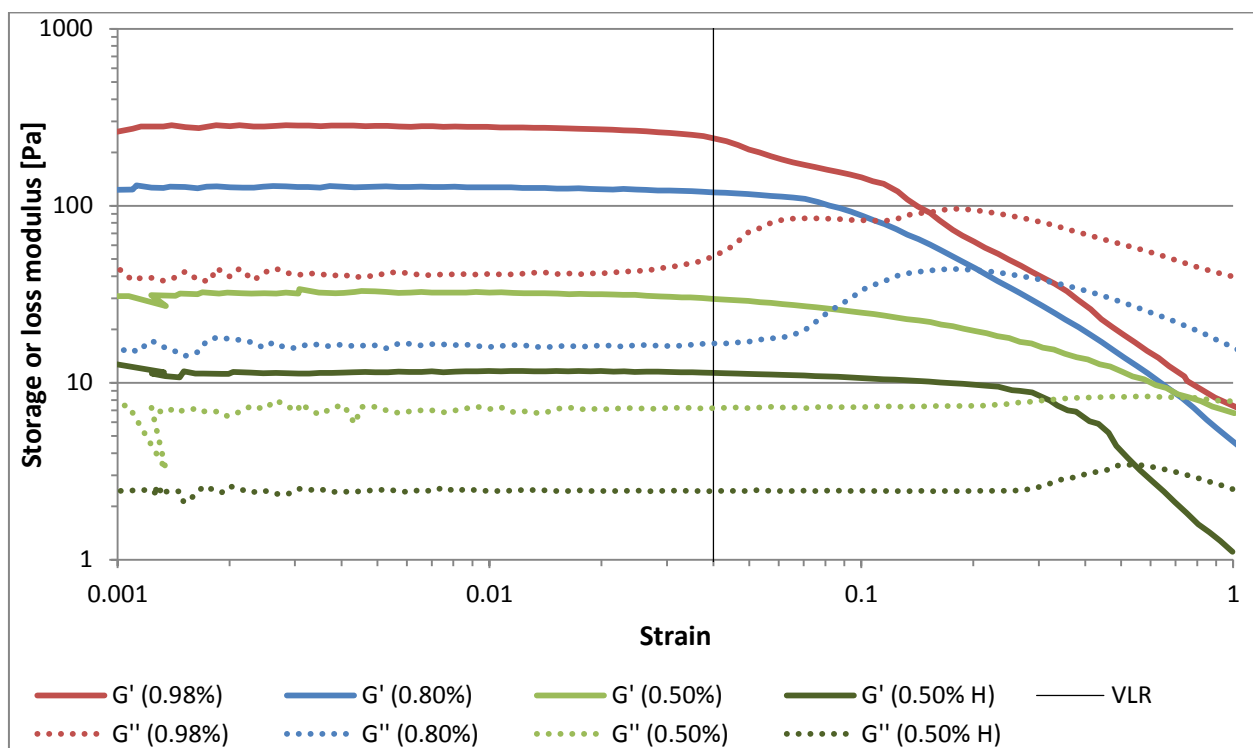


Figure 3.3.1: Amplitude sweep on MFC (0.98%, 0.80%, and 0.50%). H denotes sample containing HMDA (6.12×10^{-1} mmol/g MFC). None of the samples were heated. The temperature and frequency was held constant at 20° C and 1Hz, respectively. Two concentrations (0.98% and 0.80%) are averaged from two replicates. The two concentrations of 0.50% are based on one replicate each. The storage and loss moduli were approximately constant (i.e. yielding the VLR) for strains ≤ 0.04 .

3.3.2 Frequency sweeps

The trend with the storage and loss moduli decreasing as the concentration of MFC was decreased, and further decreasing by the addition of HMDA (6.12×10^{-1} mmol/g MFC), was also observed during the frequency sweeps, as seen in Figure 3.3.2. The samples showed an approximately constant ratio between storage and loss moduli, and thus constant phase angles, for the whole frequency range from 0.01 – 10 Hz.

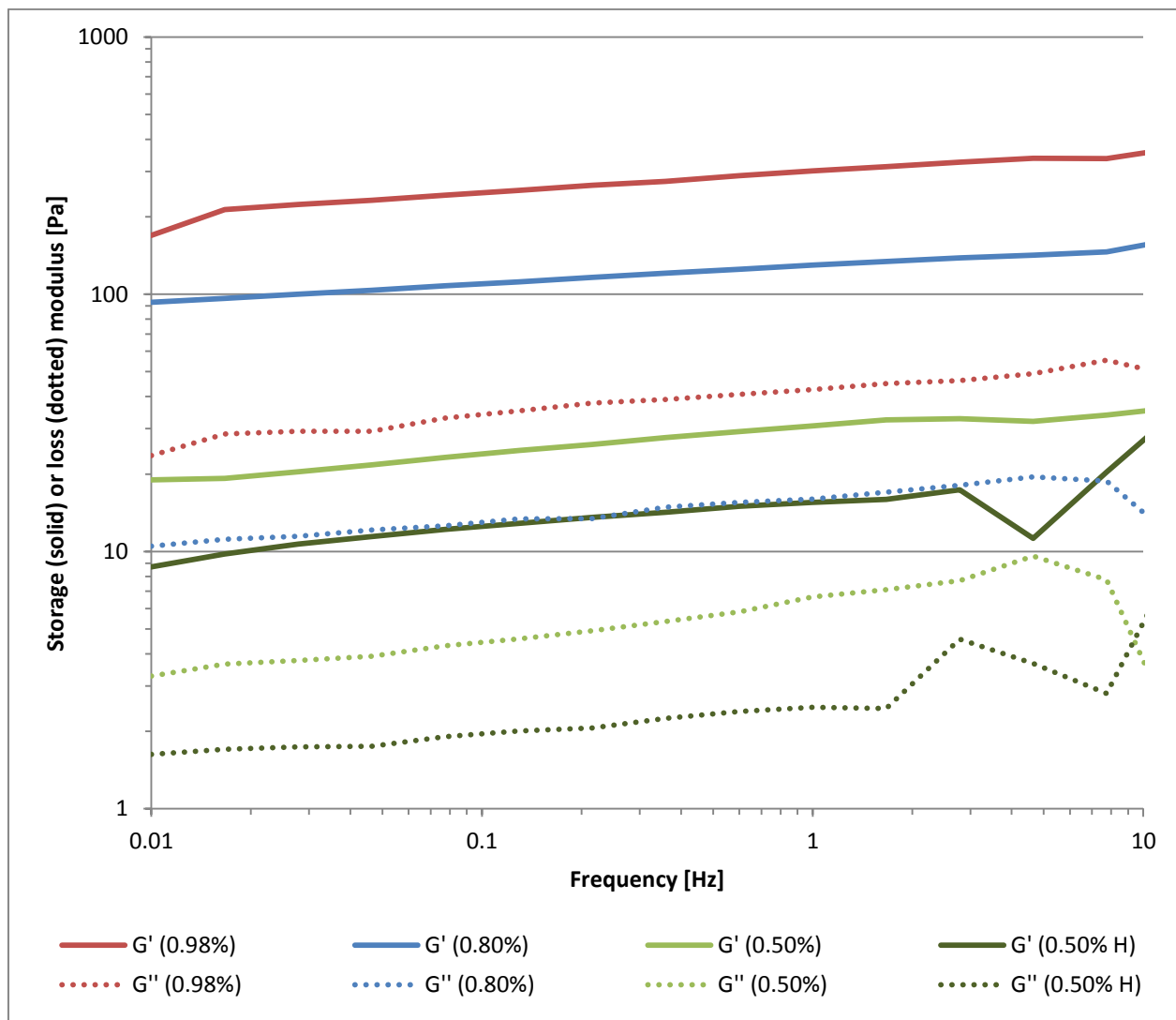


Figure 3.3.2: Frequency sweep on MFC (0.98%, 0.80%, and 0.50%). H denotes sample containing HMDA (6.12×10^{-1} mmol/g MFC). None of the samples were pre-heated. The temperature and strain was held constant at 20° C and 0.01, respectively. Two concentrations (0.98% and 0.50%) are averaged from three replicates, and two concentrations (0.80% and 0.50% with HMDA) are averaged from two replicates. All samples showed gel-like behavior for the whole frequency range (i.e. $G' > G''$, δ constant).

3.3.3 Viscosity measurements

MFC showed pseudoplastic (shear thinning) behavior, as expected from literature (see Section 1.3). Both dynamic and steady state measurements on two concentrations (0.98% and 0.50%), the latter with and without HMDA (6.12×10^{-1} mmol/g MFC), can be seen in Figure 3.3.3. Logically, the viscosity decreased as the concentration decreased. The viscosity decreased further by adding HMDA when the sample was not pre-heated. This was also qualitatively observed, as the MFC seemed to become thinner (less viscous) as the crosslinkers were stirred into the suspension during gel preparation (see Section 2.7).

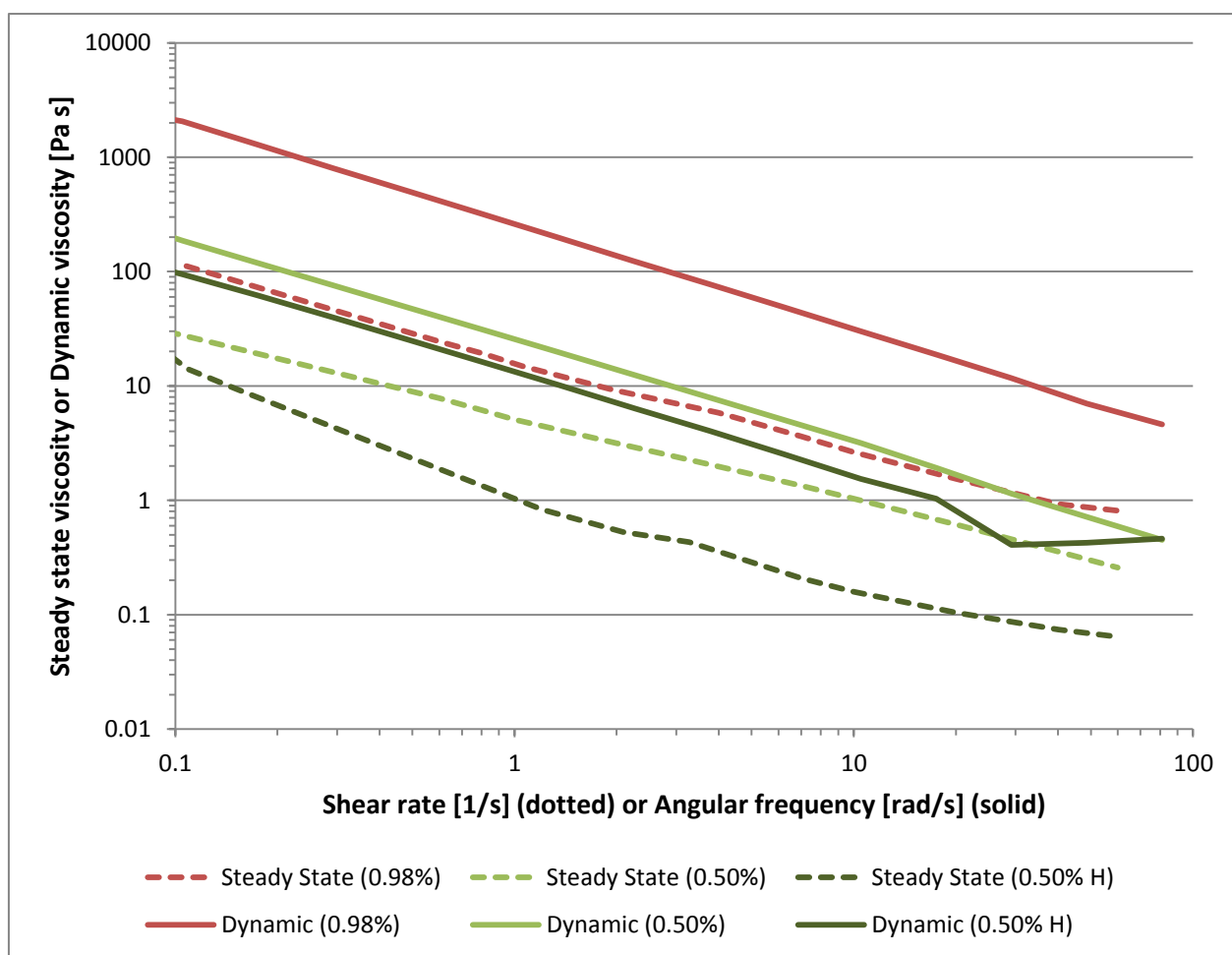


Figure 3.3.3: Steady state and dynamic viscosities measured as functions of shear rate and angular frequency, respectively. The temperature was held constant at 20° C for all measurements. For the dynamic measurements, the strain was held constant at 0.01. Two concentrations (0.98% and 0.50%) are averaged from three replicates, whereas the concentration (0.50% H) with HMDA (6.12×10^{-1} mmol/g cellulose) is averaged from two replicates. All measurements showed pseudoplastic (shear thinning) behavior.

The samples did not directly follow the Cox-Merz rule, as the dynamic viscosity was approximately ten times higher than the steady state viscosity when the shear rate ($\dot{\gamma}$) equaled the angular frequency ($\omega = 2\pi f$). The dynamic viscosity was recorded during the frequency sweeps, i.e. during small, non-disruptive angular deflections (strain of 0.01) within the VLR, whereas the steady state viscosity was recorded at logarithmically increasing shear rates in one angular direction.

3.3.4 Temperature sweeps and crosslinking

Heating the samples with crosslinkers had a significant effect on the elastic properties of the MFC gel, as can be seen on a sample with 0.50% MFC and 6.12×10^{-1} mmol HMDA/g MFC in Figure 3.3.4. During the first 60 minutes of the heating process, the storage modulus increased from approximately 15 Pa to a maximum value of just above 1000 Pa. Values on the corresponding non-heated samples from the amplitude and frequency sweeps were 11 Pa at 0.01 strain and 12 Pa at 1Hz, respectively. There was a noticeable sudden drop in the storage modulus after about 124 minutes. After this break, the storage modulus stabilized at 741.9 ± 18.1 Pa for five hours (125 – 425 minutes). The gradual increase towards the end is probably a result of the onset of the evaporation of the protective silicone oil, as the sample dried out and was charred after approximately 12 hours (data not shown).

Several attempts were made on measuring the increase in and maximum storage modulus of the MFC as a function of temperature-induced crosslinking, but almost every attempt ended in breaks in the gels, such as the one observed in Figure 3.3.4. As a result, it was very difficult to obtain proper measurements on the heat induced gelling course. A complete series of a temperature sweep, followed by a frequency sweep and finally an amplitude sweep measured on two replicates of MFC (0.80%) with HMDA (3.05 mmol/g MFC) can be observed in Appendix B. The measurements showed several breaks during the heat induced crosslinking. The behavior of the gels during frequency and amplitude sweeps were similar to the ones observed in Figure 3.3.1 and Figure 3.3.2. The breaks were most likely due to the introduction of air while stirring the crosslinker into the MFC. This air would coalesce into bubbles which expanded as the temperature was increased, leading to the observed breaks. As a countermeasure, an attempt on degassing the gels after stirring in the crosslinker was made, as described in Section 2.8.

Unfortunately, possibly due to the high viscosity of the MFC, the degassing vacuum was not powerful enough to properly remove the air bubbles.

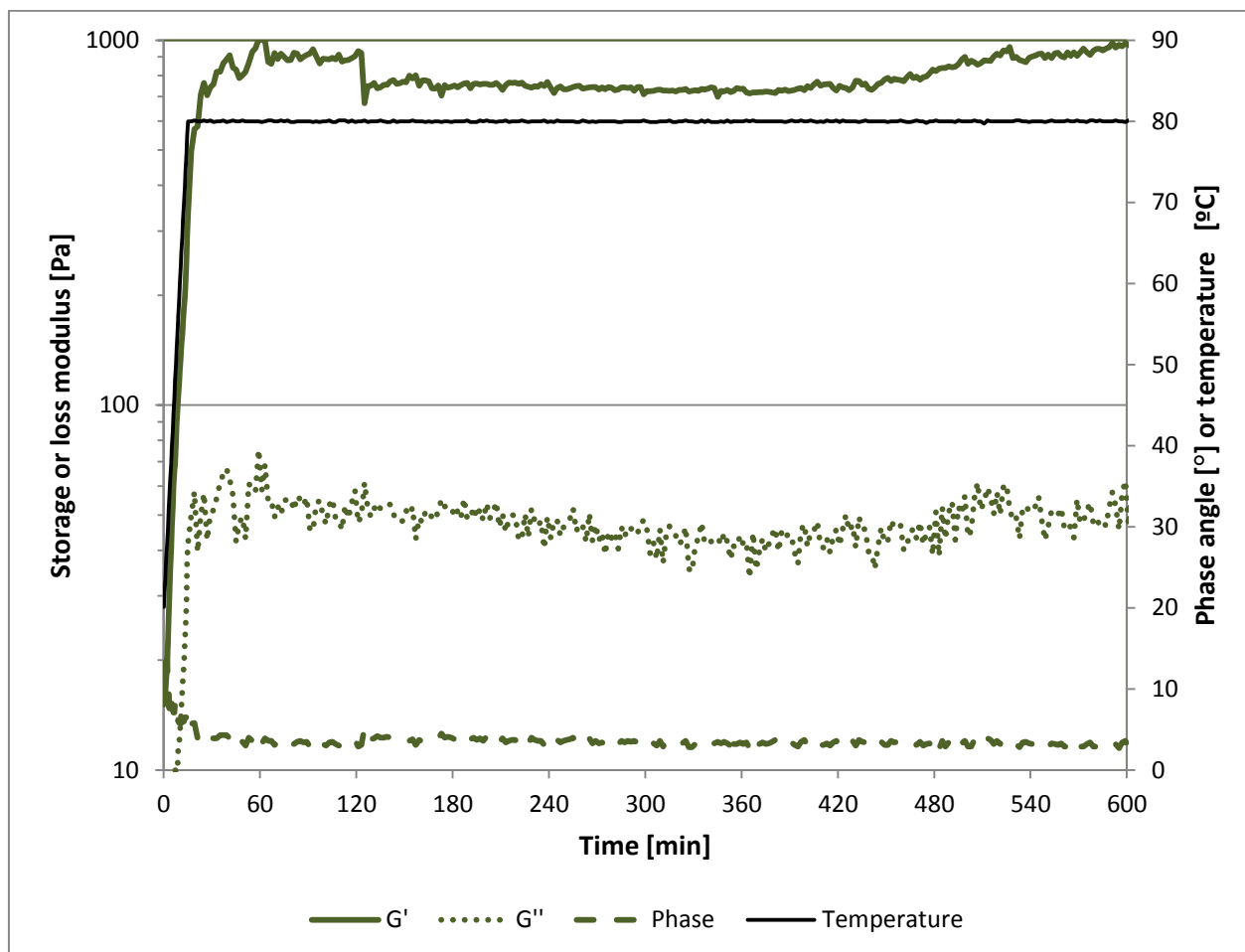


Figure 3.3.4: Temperature sweep, 20 – 80 °C (4 °C/min), then constant 80 °C for > 10 hours, measured on one replicate of 0.50% MFC with HMDA (6.12×10^{-1} mmol/g MFC). The frequency and strain was held constant at 1 Hz and 0.01, respectively.

Only one replicate of 0.80% MFC with 3.05 mmol HMDA/g MFC (corresponding to the H50 cast gels) was successfully measured without such breaks in the gel. This can be observed in Figure 3.3.5. The storage modulus of this sample reached a plateau of 1374.4 ± 49.4 Pa (25 – 75 minutes) as the temperature was held at 80° C, and decreased by about 200 Pa as the temperature was decreased back to 20° C. The storage modulus of MFC (0.80%) without HMDA decreased at constant high temperature, and increased as the temperature was decreased back down. The average storage modulus for this sample was 121.0 ± 7.6 Pa (25 – 75 minutes), more than 11 times lower than the storage modulus for the sample with HMDA.

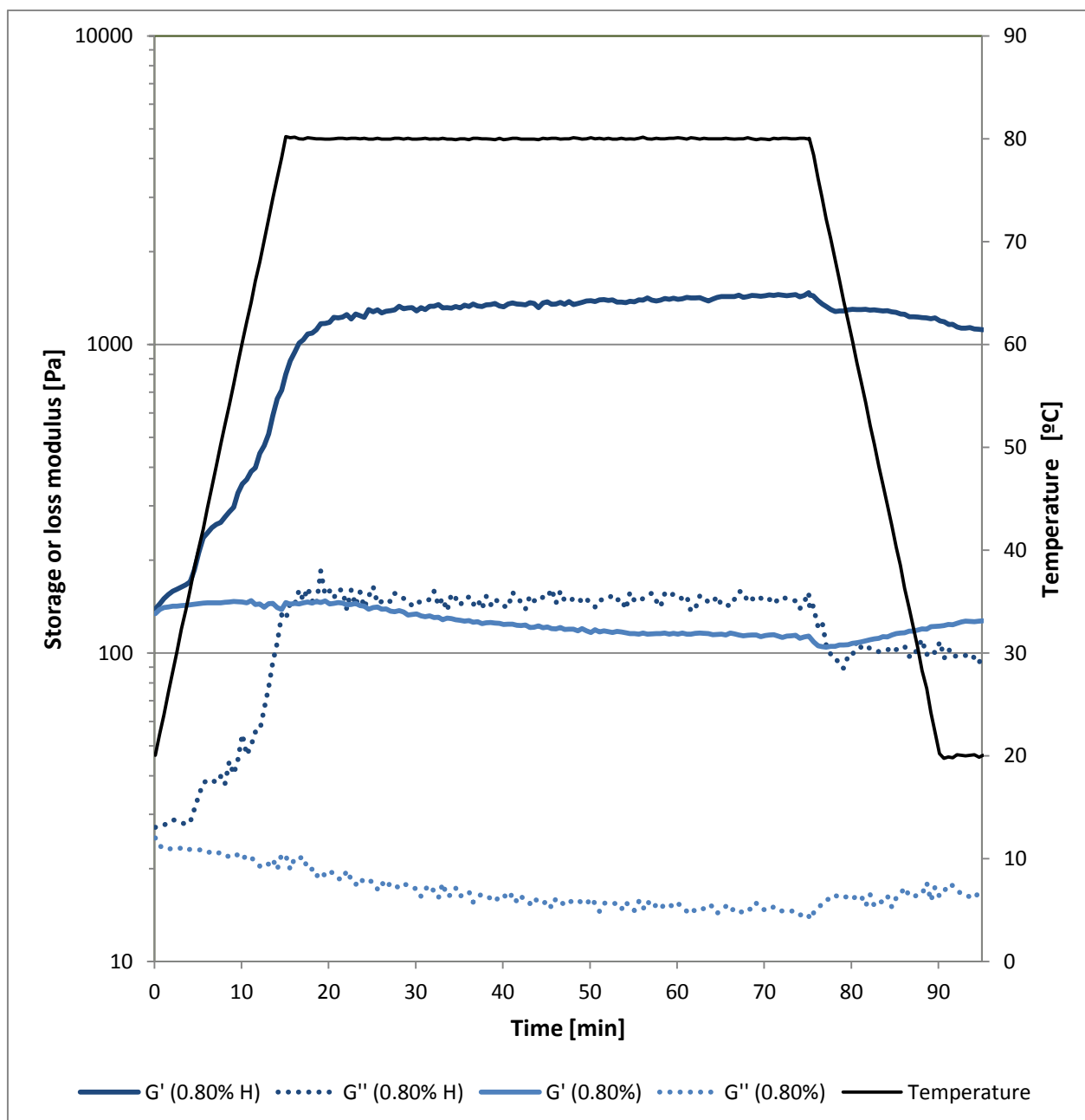


Figure 3.3.5: Temperature sweep, 20 – 80 – 20 ° C (± 4 ° C/min), constant 80° C for one hour, measured on one replicate of 0.80% MFC with HMDA (3.05 mmol/g MFC). The concentration (0.80%) without crosslinker is averaged from two replicates. The frequency and strain was held constant at 1 Hz and 0.01, respectively.

To check whether the gelling needed high temperature to initiate, a measurement was performed on MFC (0.80%) with HMDA (3.05 mmol/g MFC) where the temperature was held constant at 20° C. As can be seen in Figure 3.3.6, the storage modulus increased even in absence of higher temperatures, although not nearly as rapid as at higher temperatures.

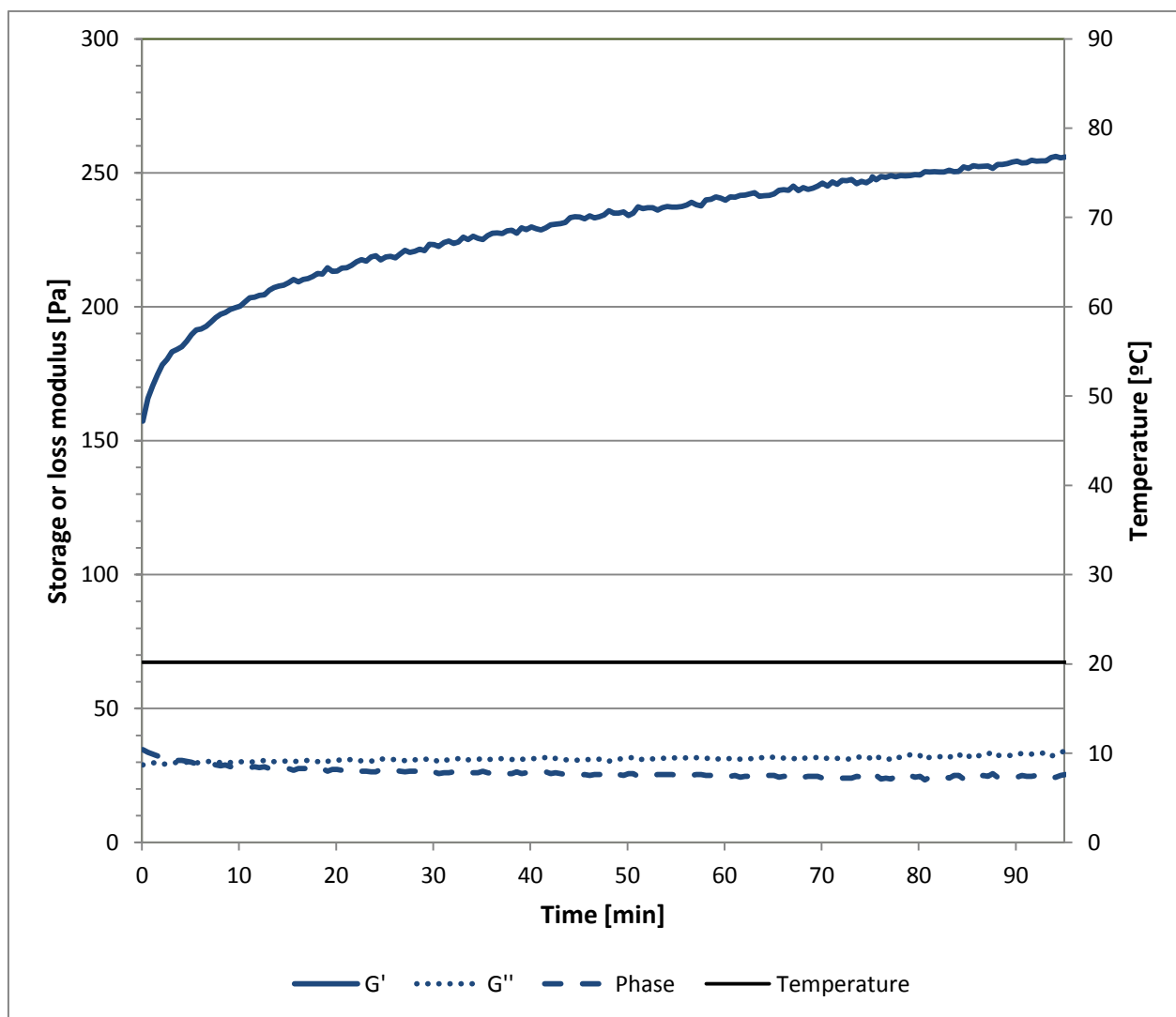


Figure 3.3.6: Constant temperature (20 ° C), strain (0.01) and frequency (1 Hz) on one replicate of MFC (0.80%) with HMDA (3.05 mmol/g MFC).

A further observation supporting the presence of successfully formed stronger crosslinks in the gels is the behavior that can be seen in Figure 3.3.7. MFC (0.80%) with and without HMDA (3.05 mmol/g MFC) was first run through a temperature sweep, then the structure was disrupted by an amplitude sweep up to a maximum strain of 1, before the strain was instantly set to 0.01. The storage modulus of the crosslinked sample only recovered to approximately half the initial value, whereas the storage modulus of the sample without crosslinker almost reached the same modulus. The structure in the samples stabilized almost immediately as the strain was set below the limit of the VLR, but the sample with HMDA did not show the same increase in the storage modulus as the sample in Figure 3.3.6.

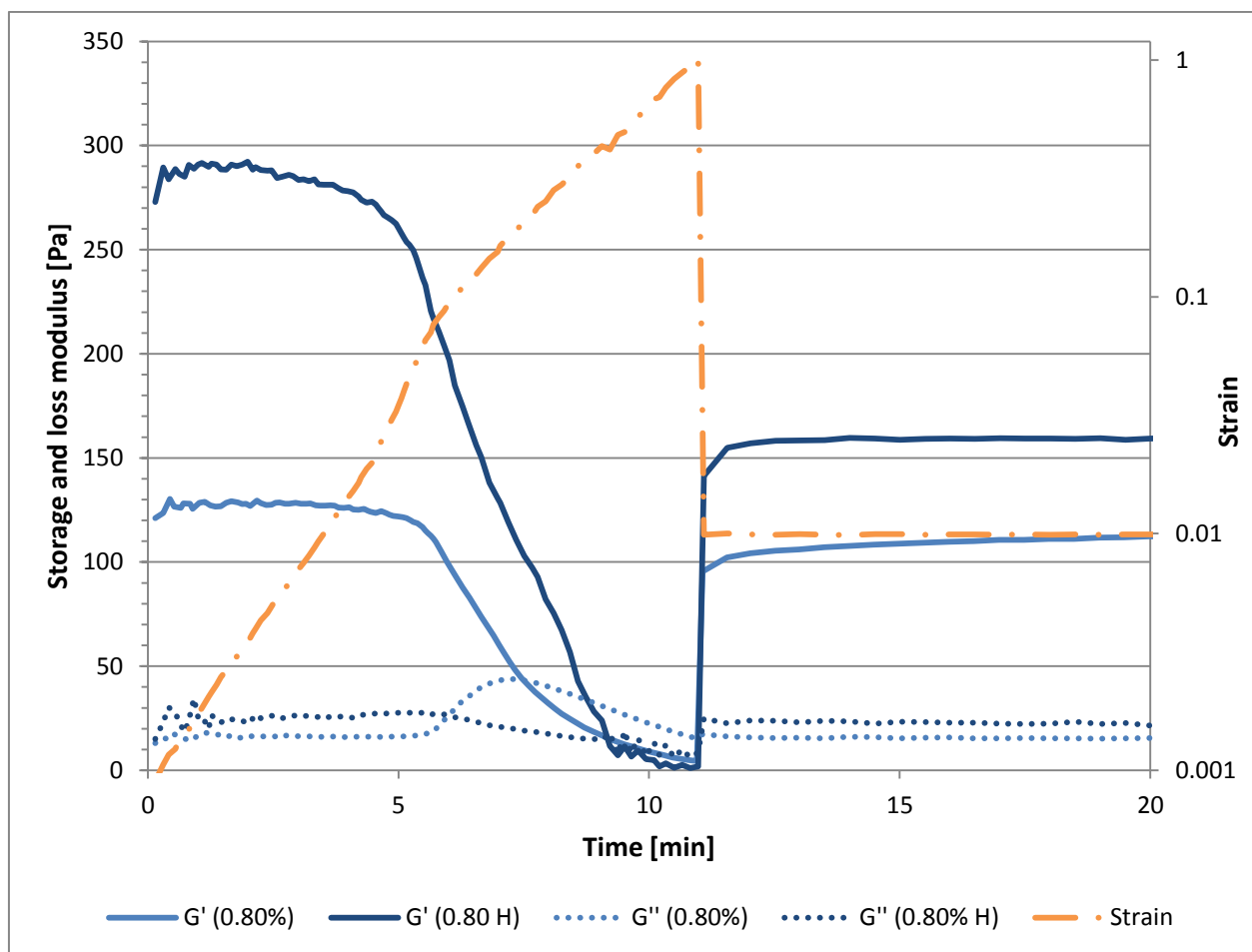


Figure 3.3.7: Amplitude sweep followed by an instant decrease of strain back to 0.01 (within the VLR) on MFC (0.80%) with and without HMDA (3.05 mmol/g MFC). The temperature and frequency was held constant at 20 ° C and 1Hz, respectively. The samples were run through a temperature sweep (20 – 80 – 20 ° C) before the measurement to induce crosslinking in the sample with HMDA, although the samples did not reach a plateau G' due to breaks. Both samples are averaged from two replicates.

3.4 Longitudinal compression and Young's modulus

Cast gels with 0.80% MFC showed remarkable elastic properties when taking in account a water content of approximately 99%. All gels were strong enough to carry their own mass, although the gels with lowest Young's moduli (≤ 2 kPa) can be said to have partly collapsed, as they expanded somewhat in width at the expense of heights. Using the *Correl* function in Microsoft Excel 2010, the coefficient of correlation between the height and the diameter of the gels with HMDA was calculated to be -0.8832. The correlation function correlates two arrays of data, yielding a coefficient of correlation between -1 (total inverse correlation) and 1 (total correlation), where a value of zero equals no correlation. There is also a positive correlation of

0.9115 between the height and Young's modulus, and a negative correlation of -0.9342 between the diameter and Young's modulus. Since both the height and diameter is incorporated in the equation for Young's modulus (see Table 1.7.1), this is logical. The reason they do not correlate completely is the addition of another factor in the equation, i.e. the gradient of initial linear part of the force-compression curve, as seen in Figure 3.4.1. The second parallels of the E50 and H50 gels were compressed 8 mm, to observe the flow and fracture behavior of the gels. The gels with HMDA showed an average compression length ($\pm 1SD$) of 5.09 ± 0.19 mm at maximum force, whereas the gels with EDA were compressed a little longer, 5.28 ± 0.17 mm. The gels with HMDA were stronger, yielding at an average maximum compression force of 0.85 ± 0.08 N. The average maximum compression force of the EDA gels was 0.53 ± 0.02 N. The full compression curves of these gels can be observed in Appendix C.

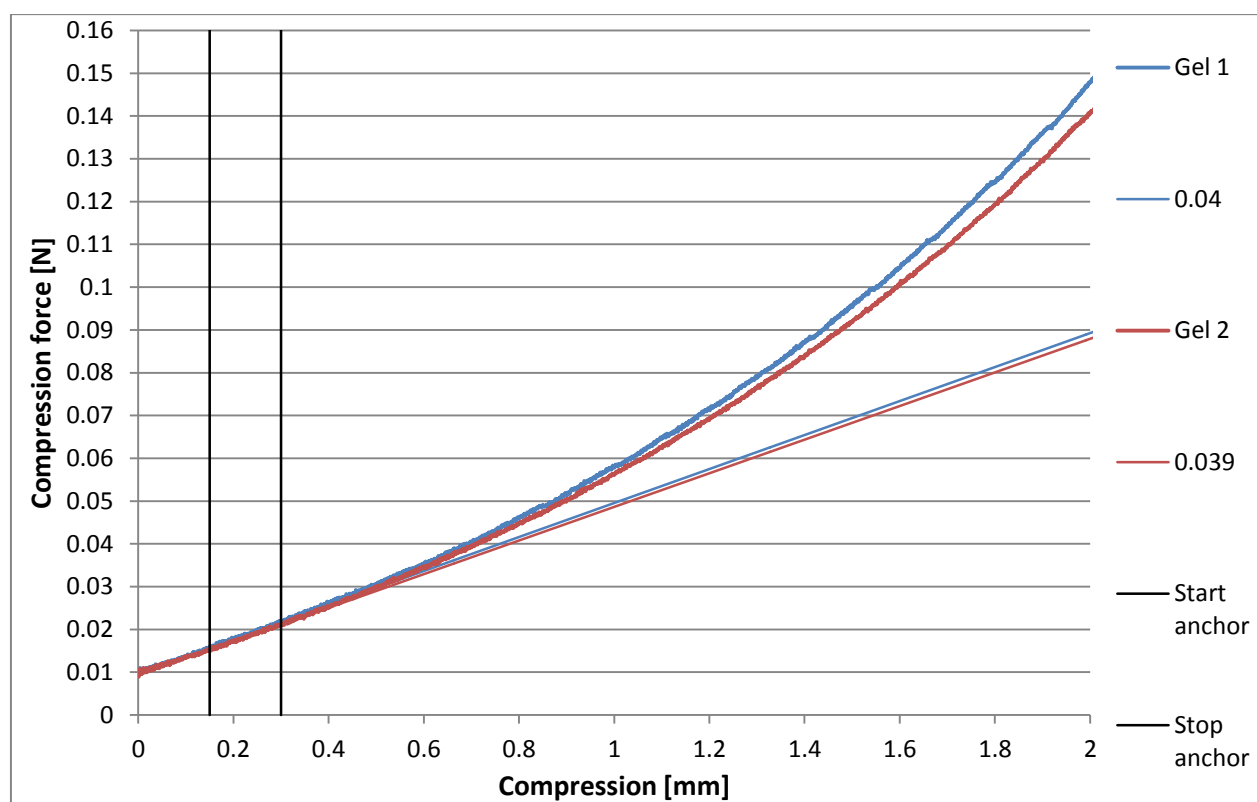


Figure 3.4.1: Force-compression curves for two gels with HMDA (3.05 mmol/g MFC) obtained by longitudinal compression with a texture analyzer. The numbers in the legend are the gradients of the linear regression lines for the individual curves, which were obtained for compression between 0.15 – 0.30 mm. The curves were recorded after an initial trigger force of 1 g was reached. The gels only showed ideal (i.e. linear) elastic behavior for very small strains (< 0.5 mm). The remaining replicates can be found in Appendix C.

The gels were easily decanted from the casting molds, without any need for lubrication. Some of the gels adhered to the probe after compression. This adhesion was not permanent, as the gels could be slid around while still attached to the probe, suggesting physical interactions such as capillary or electrostatic forces. Figure 3.4.2 shows a such adhesion. The gels regained their shape after being removed from the probe.

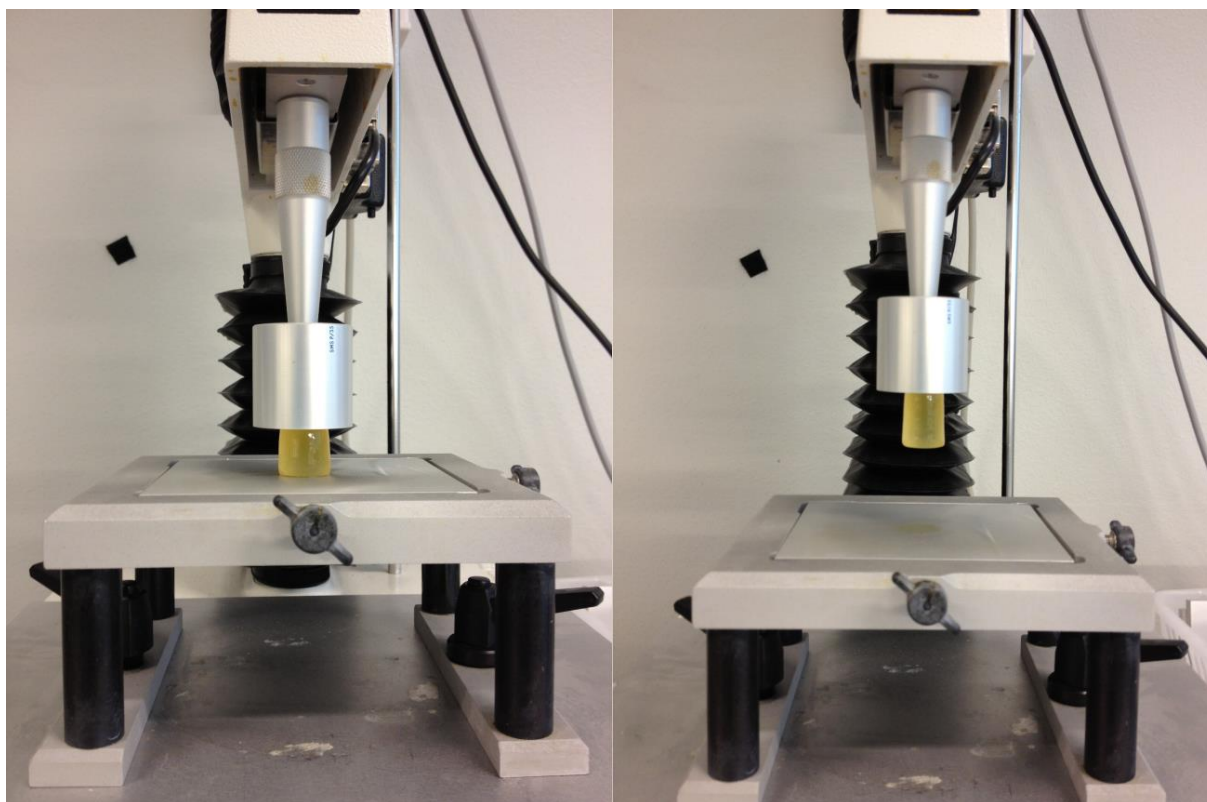


Figure 3.4.2: A gel with the highest concentration of EDA (6.08 mmol/g MFC) approximately at maximum (2 mm) compression (left) and adhering to the probe after the retraction of the probe (right). Note that the gel is elongated by the gravitational force, but it reached a maximum elongation without breaking, and the shape was regained after removal from the probe.

As can be seen in Figure 3.4.3, the strength of the gels could be controlled by the concentration of crosslinkers, with a maximum increase in Young's modulus of 270% from the lowest concentration of HMDA to the highest. Numerical values can be found in Appendix C. Another factor controlling the strength seemed to be the length of the crosslinkers. The only difference between EDA and HMDA is a longer carbon chain of four more carbon atoms in the latter. The results were also remarkably reproducible, as the second parallels of H50 and E50 gels prepared independently from the first parallels yielded very similar Young's moduli.

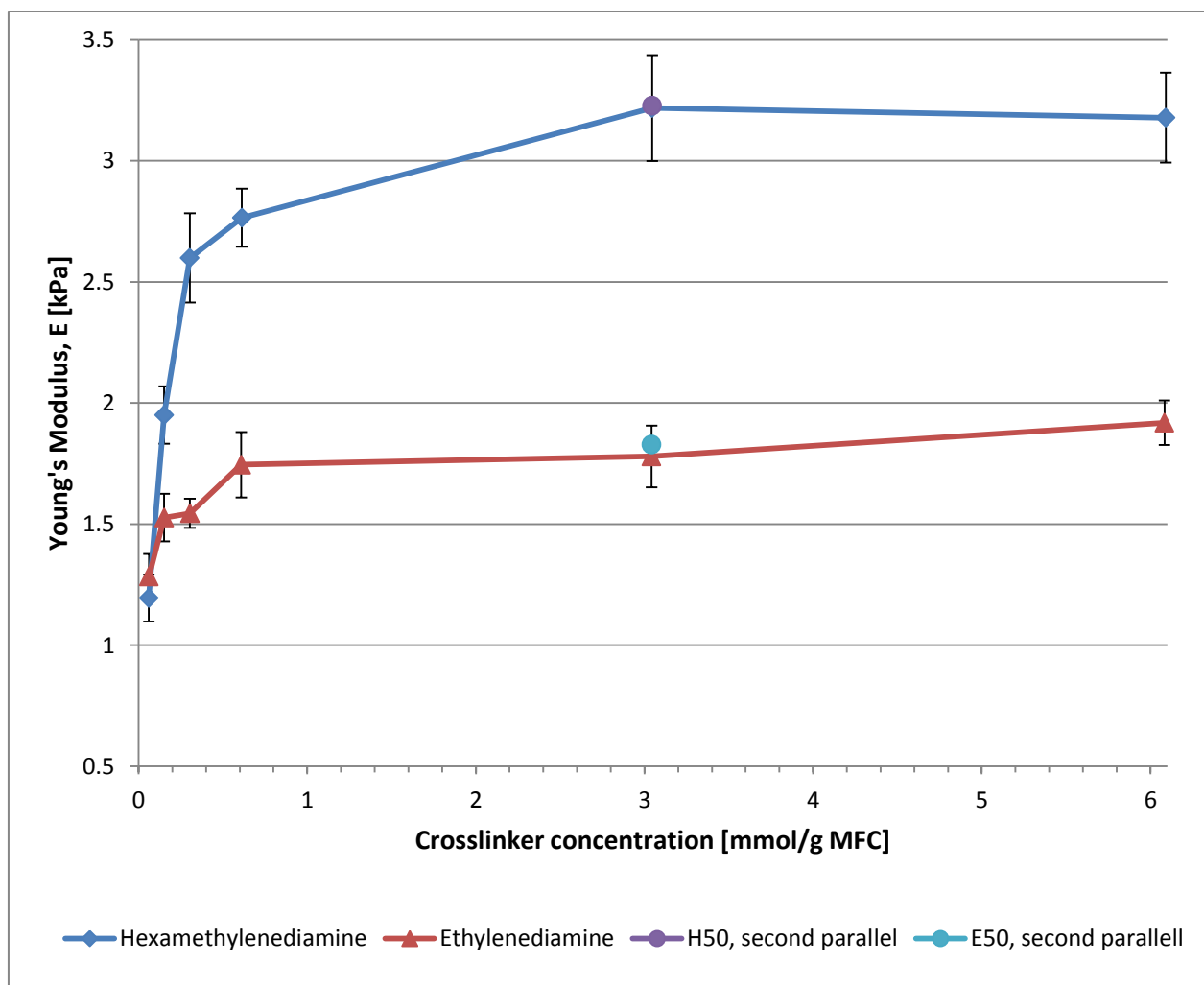


Figure 3.4.3: Young's modulus as a function of crosslinker concentration. Seven gels were prepared and measured for each crosslinker at each concentration. The error bars show \pm one standard deviation from the mean. Notice the reproducibility for the second parallels of H50 (3.05 mmol HMDA/g MFC) and E50 (3.04 mmol EDA/g MFC), which were measured gels prepared independently from the first parallels.

A factor that does not show in Figure 3.4.3 is the time dependence of the gelling. Due to the sharp increase in storage modulus occurring almost at once in the dynamic measurements (see Section 3.3.4), it was assumed that the gelling would reach a maximum point rather quickly during heating. The gels were heated overnight at 80° C, but the total time varied from approximately 16.5 hours – 20.5 hours between the different concentrations, as can be seen in Appendix C. To investigate whether this variation could affect the results in Figure 3.4.3, time-lapsed measurements of a H50 parallel was executed. As can be seen in Figure 3.4.4, the gelling might not have reached saturation even after 24 hours. Looking closer at the results, there

seems to be a linear increase in gelling during the first 5 hours, which apparently leveled out to a gentler increase after this. The minimum and maximum total time in the heating cabinet for the gels in Figure 3.4.3 is also marked (vertical lines) in Figure 3.4.4. The increase of Young's modulus within this time interval is approximately 0.3 kPa (assuming the linear assumption between 8 hours and 24 hours is correct), thereby being in the same range as approximately two standard deviations for the concentration dependent measurements. Thus this variation in total time of heating does probably not severely affect the trend seen in Figure 3.4.3. The correlation coefficient between HMDA concentration and Young's modulus for the gels in Figure 3.4.3 is 0.6874, whereas the correlation between heating time and Young's modulus is only 0.0874, supporting this assumption. Even so, the variation in heating time might explain some of the smaller deviations, e.g. between E2.5 (20.5 hours in heating cabinet, $E = 1.527$ kPa) and E5 (16.8 hours in heating cabinet, $E = 1.544$ kPa).

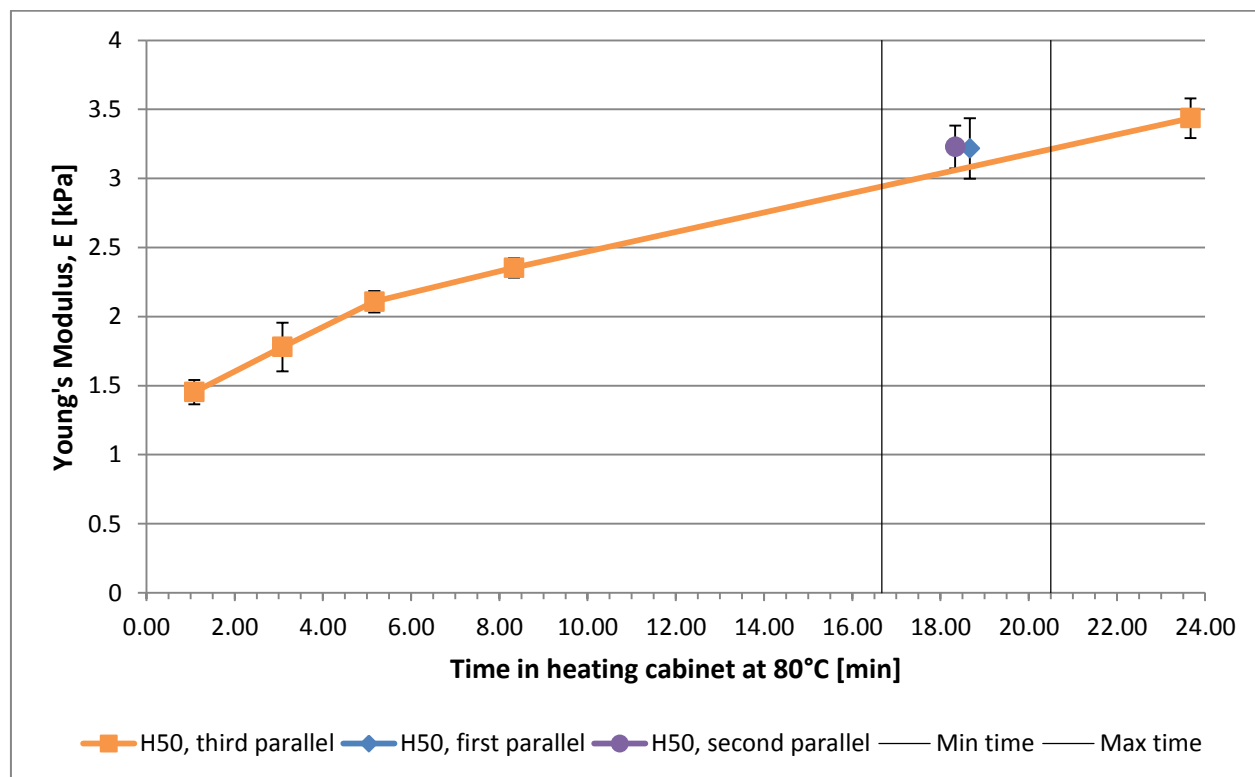


Figure 3.4.4: Young's modulus as a function of time in heating cabinet at 80° C for three independent parallels of gels with HMDA (3.05 mmol/g MFC). $n = 7$ (first and second parallel), $n = 5$ (third parallel) for each data point. The error bars show \pm one standard deviation from the mean. The vertical lines mark the variation of heating time for the gels with different concentrations of crosslinker in Figure 3.4.3.

Longitudinal deformation was also measured on gels prepared with HMDA and 2-picoline-borane. These gels showed, with the exception of one concentration, slightly lower Young's moduli than the regular gels, as can be seen in Figure 3.4.5. The trend with a correlation between crosslinker concentrations and Young's modulus held for these gels as well. The most striking difference between the regular gels and the gels with 2-picoline-borane was that the latter showed none of the color change typical for the regular gels. Given the almost equal Young's moduli, this may suggest that the color change stem from the double bonds of the Schiff bases, whereas the reduced single amine bonds do not give rise to any observable colors.

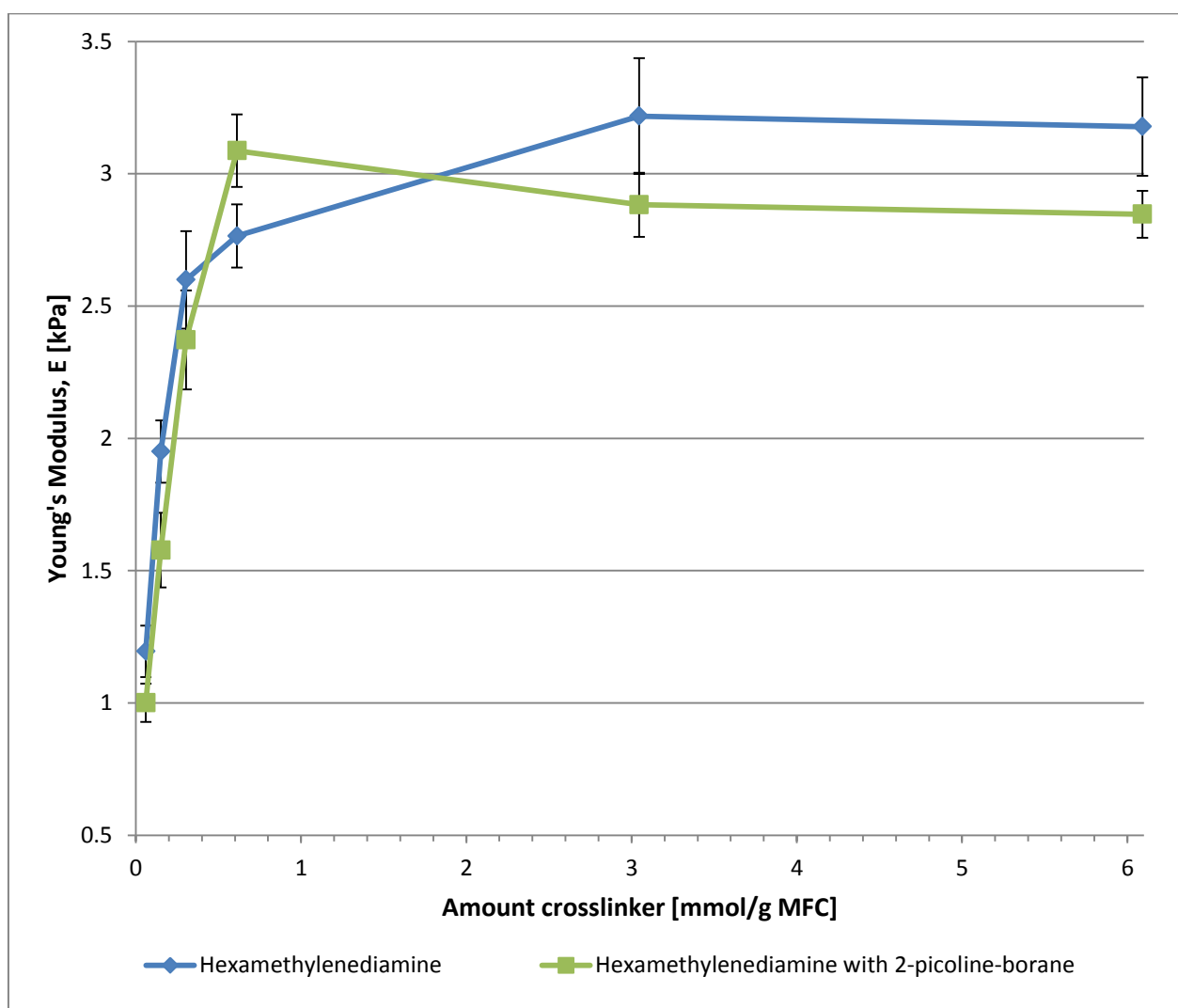


Figure 3.4.5: Young's modulus as a function of HMDA concentration for gels with and without 2-picoline-borane. $n = 7$ for each data point. The error bars show \pm one standard deviation from the mean.

3.5 pH measurements

The pH-values of the 0.005 g/ml HMDA and EDA solutions were 11.78 and 11.43, respectively. Adding the amount of crosslinker-solutions equal to the amount in one single H10 or E10 gel to 100 ml MQ-water yielded pH-values of 10.26 and 9.80 for HMDA and EDA, respectively. When whole gels were immersed in 100 ml MQ-water for some time, the pH increased from approximately neutral to maximum values of 9.22 (H10), 9.21 (H10 with 2-picoline-borane), 8.57 (E10), and 8.89 (E10 with 2-picoline-borane), as seen in Figure 3.5.1. When gels were dissolved by stirring before measuring pH, the pH was highest at the first measurement and lower than for undamaged gels, as seen in Figure 3.5.2.

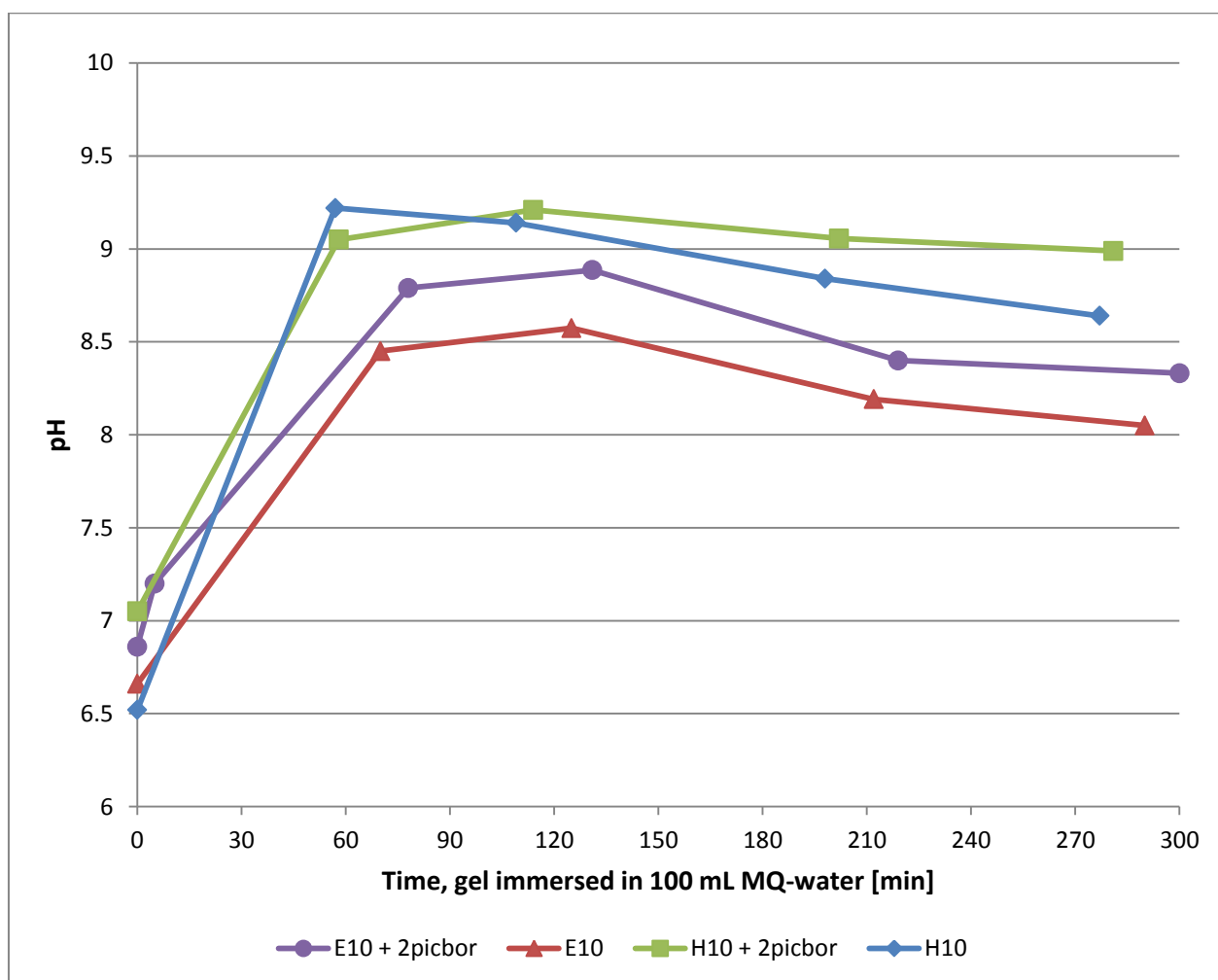


Figure 3.5.1: pH measured at different times after immersing whole gels with HMDA (6.12×10^{-1} mmol/g MFC) or EDA (6.09×10^{-1} mmol/g MFC), with and without 2-picoline-borane (1.22 mmol/g MFC), in 100 ml MQ-water.

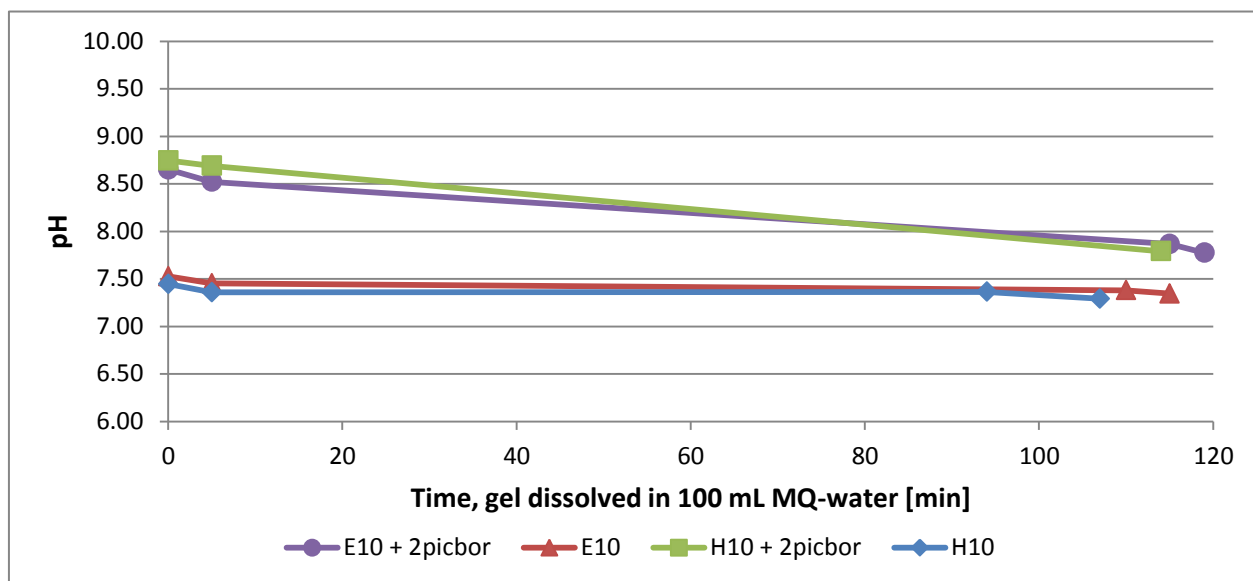


Figure 3.5.2: pH measured at different times after dissolving gels with HMDA (6.12×10^{-1} mmol/g MFC) or EDA (6.09×10^{-1} mmol/g MFC), with and without 2-picoline-borane (1.22 mmol/g MFC), by magnetic stirring in 100 ml MQ-water.

3.6 Water absorption

The crosslinked gels were prepared with an initial MFC concentration of 0.80%, but during the approximate 5 hours the gels were immersed in water for the pH measurements seen in Figure 3.5.1, they swelled significantly. These gels were unfortunately not weighed, but a qualitative comparison between the swelled gels and gels just after the removal from the casting molds can be seen observed in Figure 3.6.1. The cylindrical structure of the strongest gels (with HMDA) seemed to keep more intact than the weaker gels (with EDA).

The water reabsorption of freeze-dried gels was also measured, as described in Section 2.15, and seen in Figure 3.6.3. The gels almost instantly reached approximately maximum absorption, and the variation seen in Figure 3.6.2 may have been induced when removing surplus water using a tissue paper. The moisture content was averaged from the plateau values from both replicates of each gel type. The average moisture content of the pure MFC gels were 98.66% (1SD = 0.22%), 97.81% (1SD = 0.20%) for the gels with EDA (3.04 mmol/g MFC), and 97.50% (1SD = 0.15%) for the gels with HMDA (3.05 mmol/g MFC).

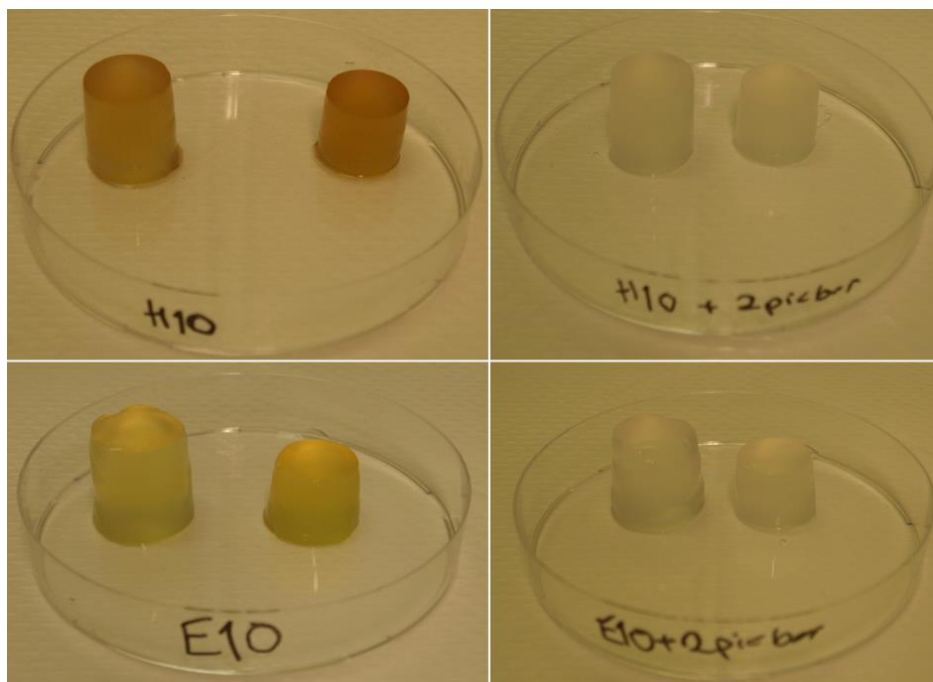


Figure 3.6.1: Qualitative comparison between gels that had been immersed in MQ-water for approximately 5 hours (left) and gels right after removal from the casting molds (right). Also notice the color difference between the gels where the Schiff-bases had been reduced by 2-picoline-borane (right frames) and the gels with Schiff-base links (left frames), as well as the color difference between the stronger gel (H10; upper frames) and the weaker gel (E10; lower frames).

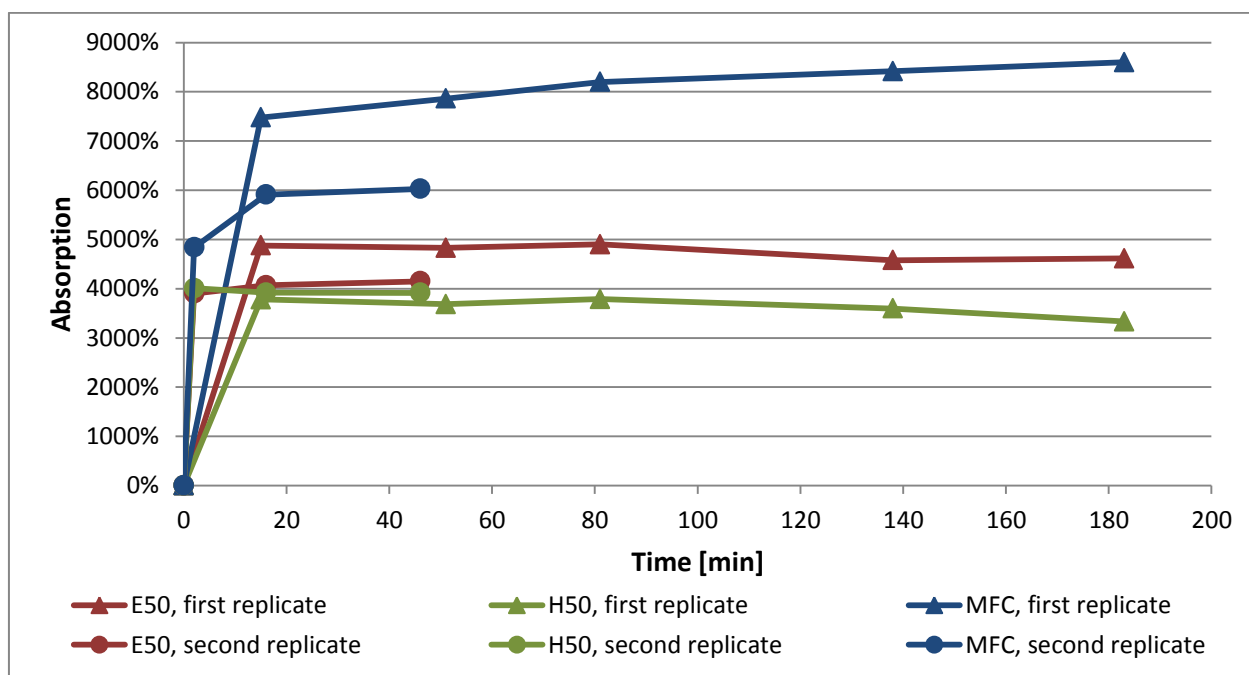


Figure 3.6.2: Water absorption over time for freeze-dried MFC gels without crosslinkers, with EDA (3.04 mmol/g MFC), and with HMDA (3.05 mmol/g MFC).

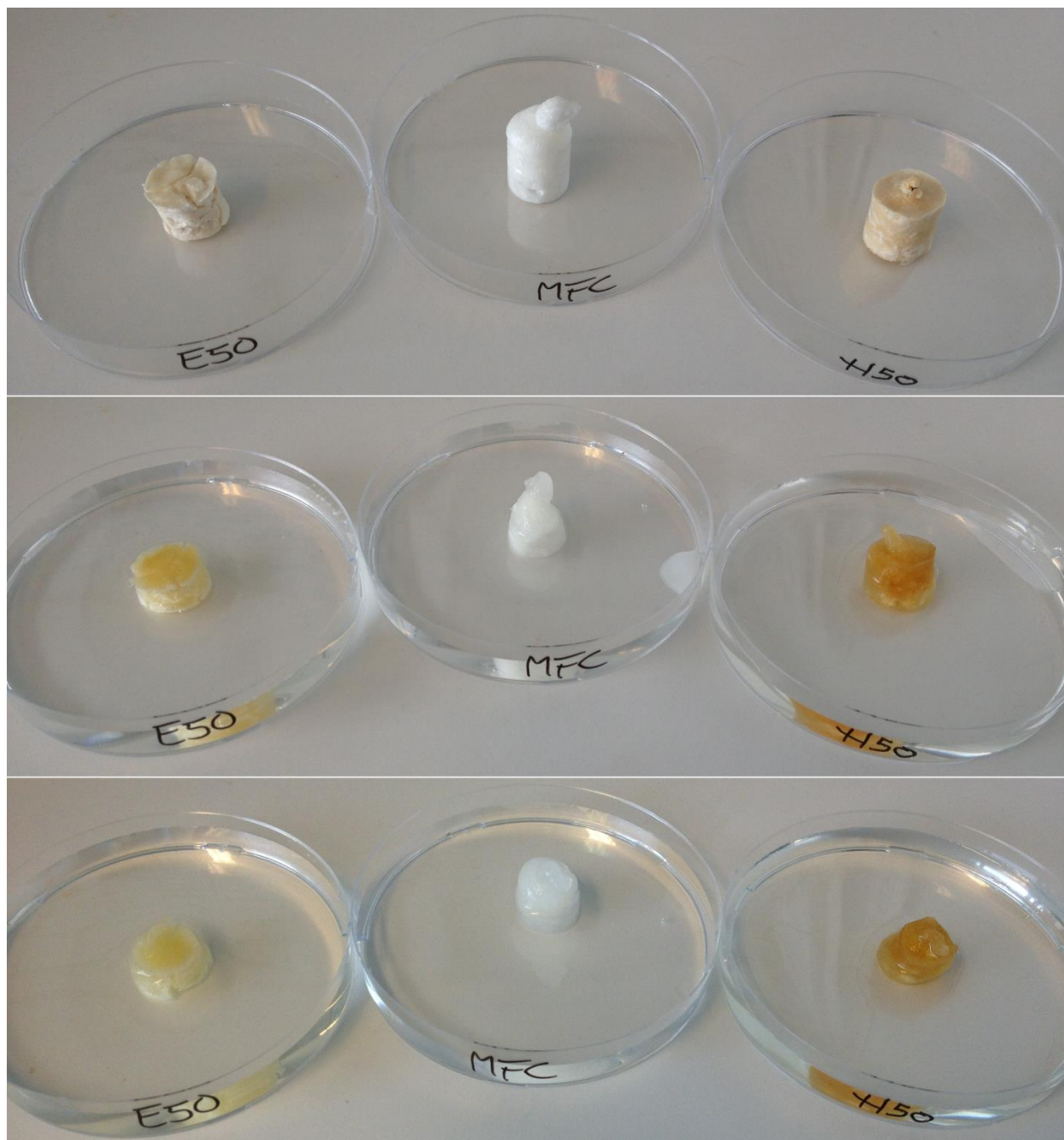


Figure 3.6.3: Water absorption in freeze-dried gels with EDA (3.04 mmol/g MFC, left), no crosslinkers (middle), and HMDA (3.05 mmol/g MFC, right), before addition of water (top), instantly after adding water (middle), and 15 minutes after adding water (bottom).

3.7 SEM images of freeze-dried gels

Imaging pieces of the freeze-dried gels using SEM uncovered an extensive pore network structure in all the gels. It is important to be aware that the structure observed in these images probably was a result of the freeze-drying process, and not representative for the original network structure in the never-dried MFC gels. The use of liquid nitrogen ensured an almost instantaneous freezing, and thus minimal ice-crystal formation, close to the metal of the casting molds and plate. The center of the gels took longer to freeze, and since the ice was hindered from expanding outwards, it expanded upwards from the center, as can be observed in the freeze-dried gels in Figure 3.6.3. Despite of this, several interesting observations could be made, as can be seen in the following figures. For more images, see Appendix D.

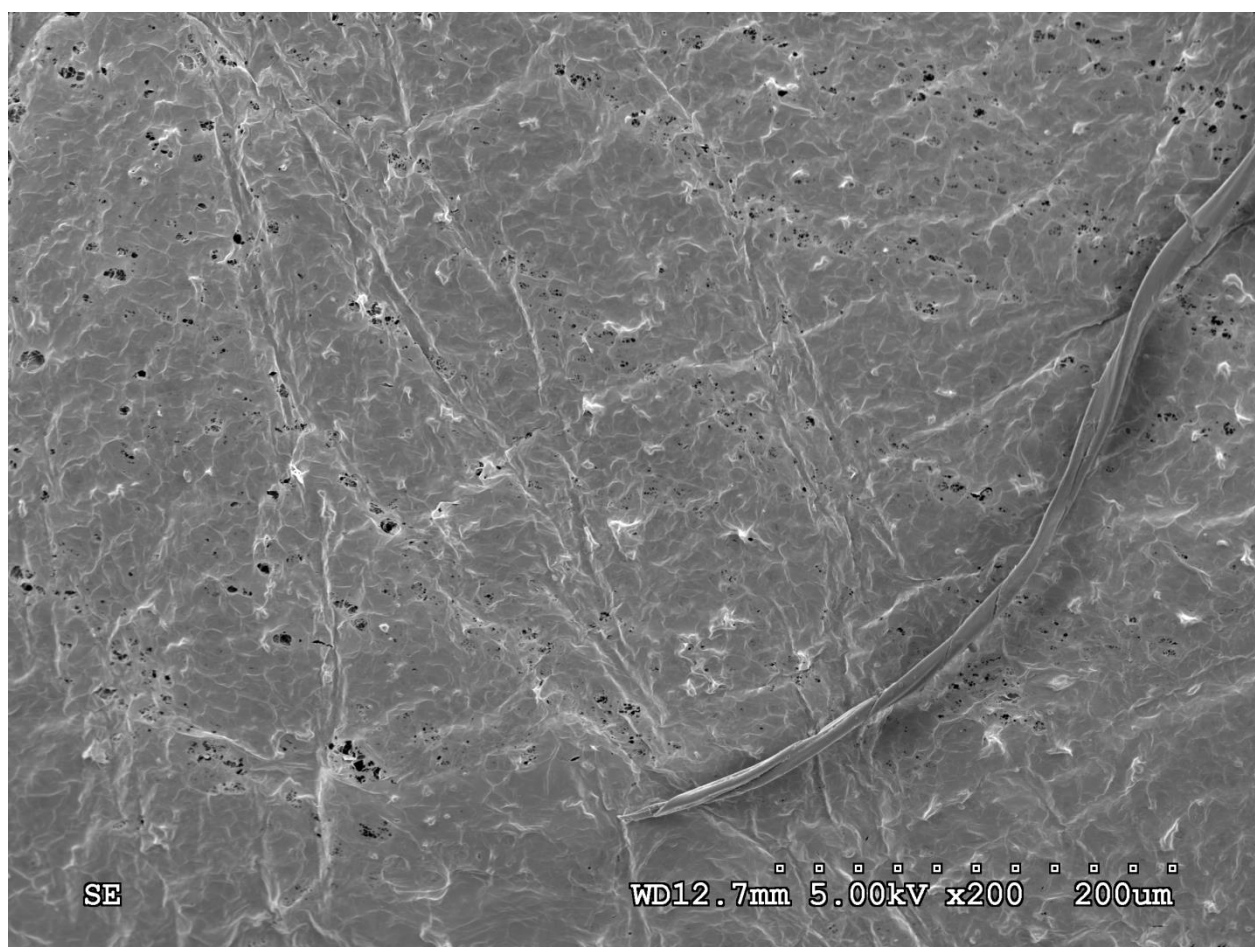


Figure 3.7.1: Surface of a freeze-dried MFC gel with EDA (3.04 mmol/g MFC). The smooth surface was probably an artifact from being pressed against the smooth wall of the metal casting mold. Notice the unfibrillated fiber and the presence of several small particles on the surface.

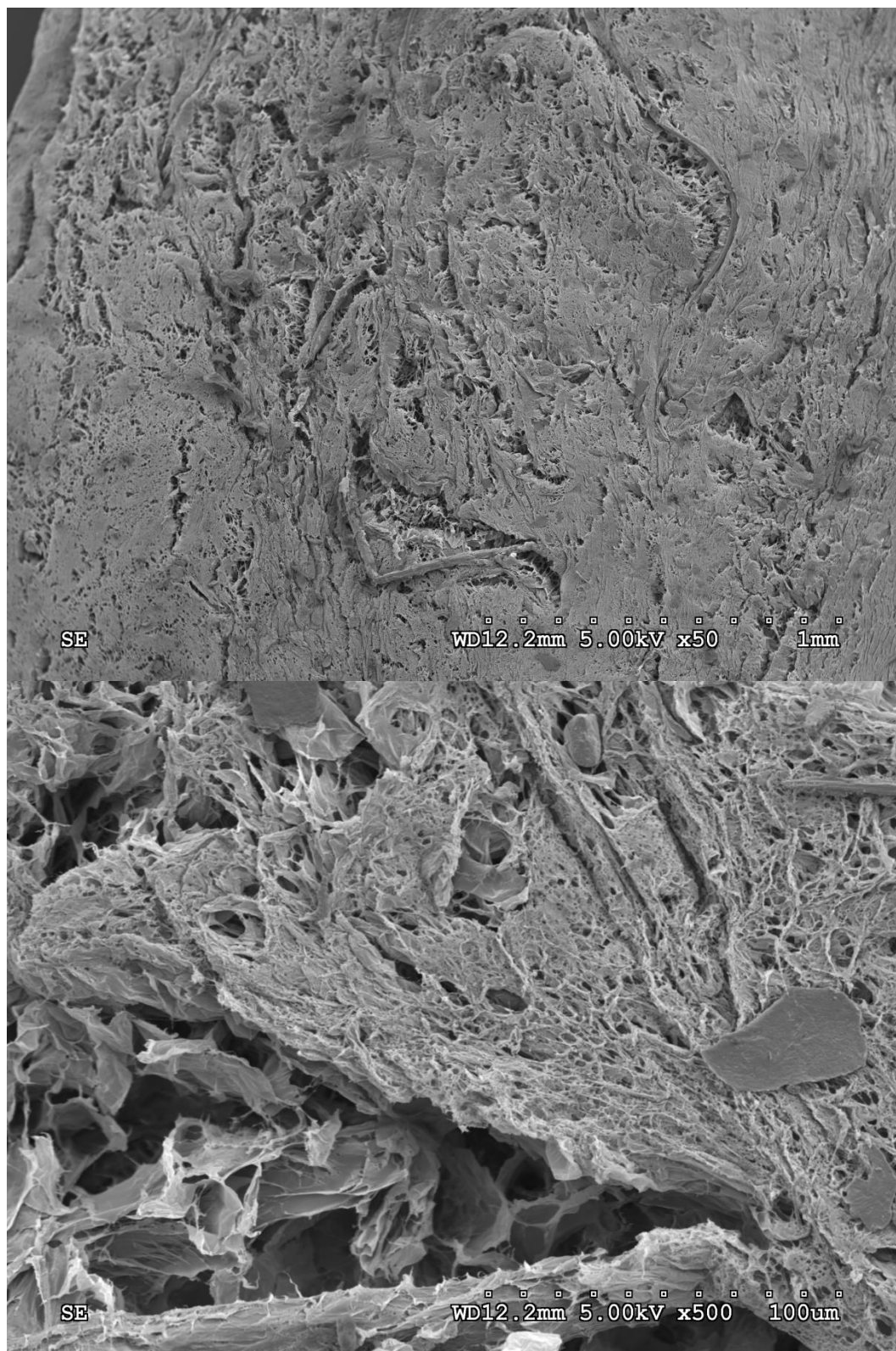


Figure 3.7.2: Surface of a freeze-dried MFC gel without crosslinkers. Notice the very porous, irregular structure, as well as the presence of several unfibrillated fibers.

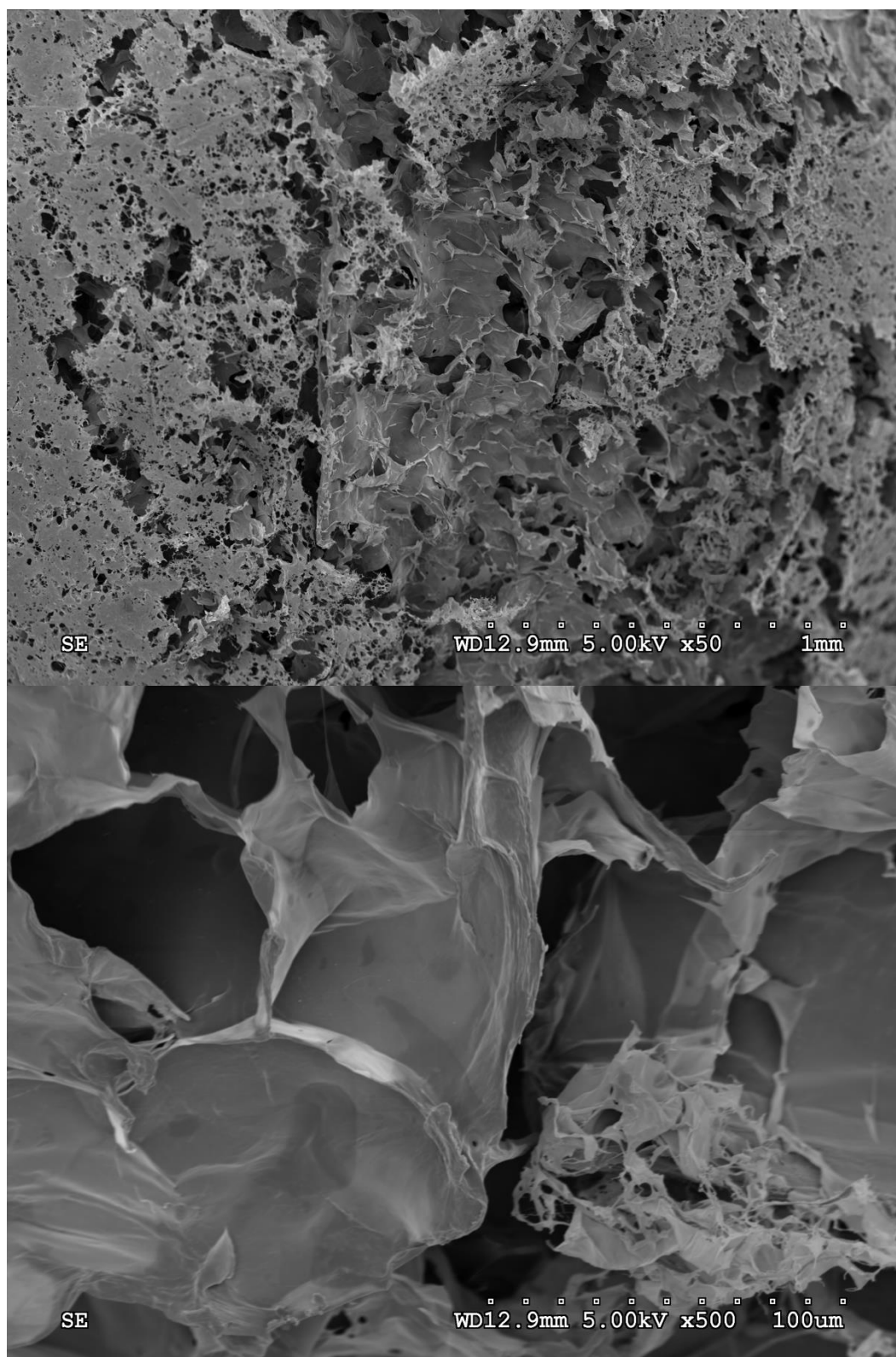


Figure 3.7.3: Surface of a freeze-dried MFC gel with HMDA (3.05 mmol/g MFC). Notice the extremely thin sheets making up the walls of the pore network.

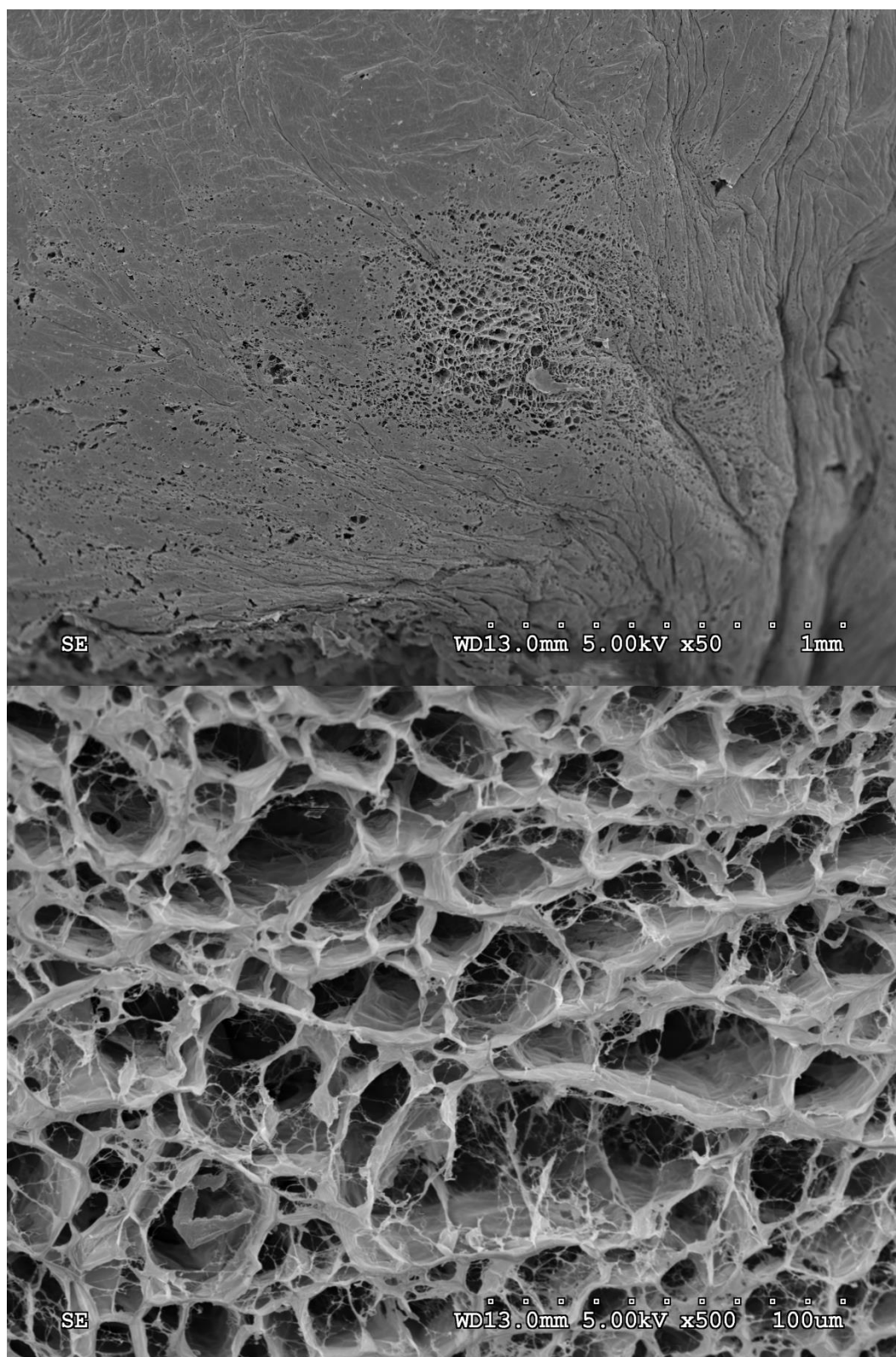


Figure 3.7.4 Surface of a freeze-dried MFC gel with EDA (3.04 mmol/g MFC). Notice the presence of microfibrils not fully compressed into the sheet-structure making up the freeze-dried gels.

3.8 Residual fibers and micro-topographical characterization

Using the data from the FiberMaster and the procedure described in Section 2.12, the amount of residual fibers in the MFC was estimated to be 7.57% (1SD = 0.28%). The presence of residual fibers was also confirmed by the laser profilometry images, as can be seen in Figure 3.8.2 and Figure 3.8.3. Even with the layer of gold coated upon the surface of the films, there was some noise in the images. This was especially prominent at the edges of fibers, probably because of light being reflected there due to the large variations in height. Representative images of each film can be found in Appendix E. As can be seen in Figure 3.8.1, the root-mean-square deviation surface roughness (Sq) values of the films seemed to increase with increasing amounts of crosslinkers, although the variations were large within the image sets for each concentration. This might be explained by the presence of small particles of some sort at the highest concentrations, possibly crystals of surplus crosslinkers, as seen in Figure 3.8.3.

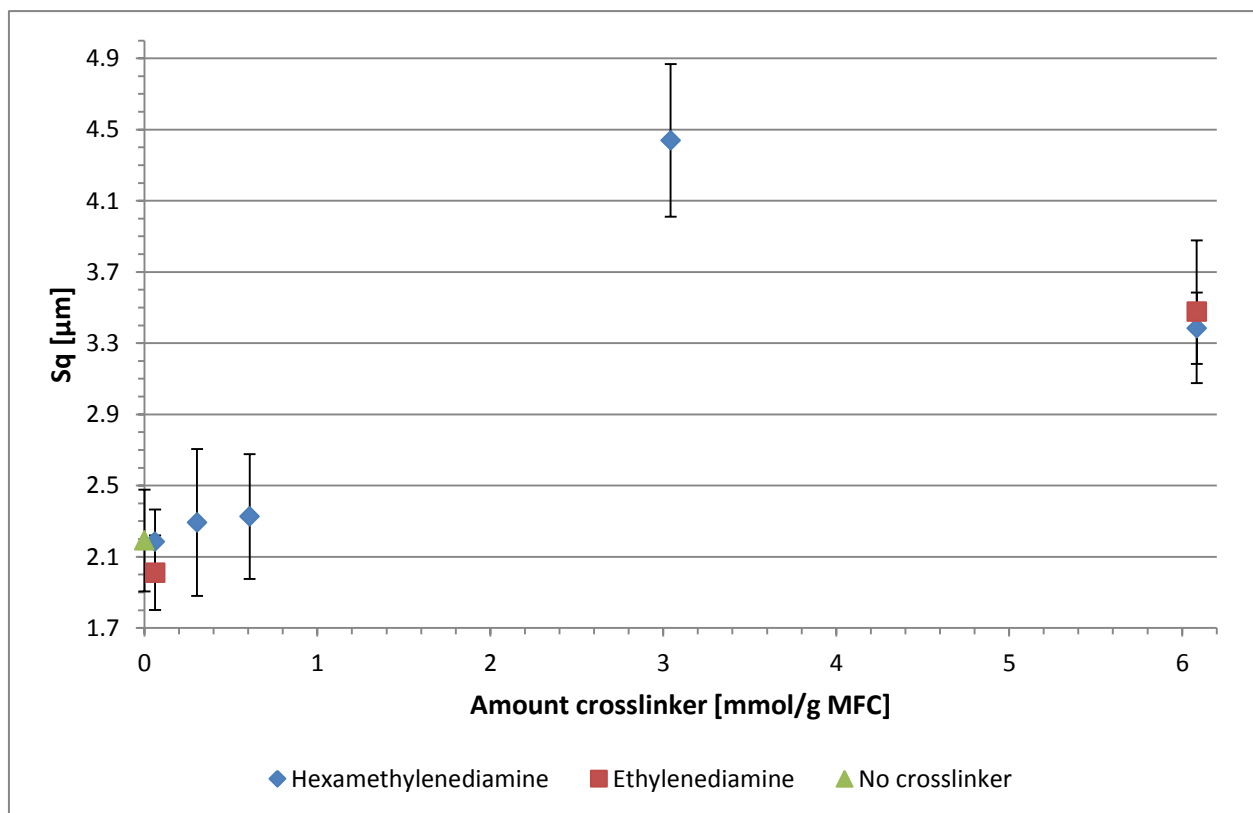


Figure 3.8.1: Root-mean-square deviation surface roughness (Sq) as a function of amount of crosslinkers in the dried films, obtained by processing laser profilometry images using ImageJ. Each concentration is the average of ten images. The error bars show \pm one standard deviation from the mean.

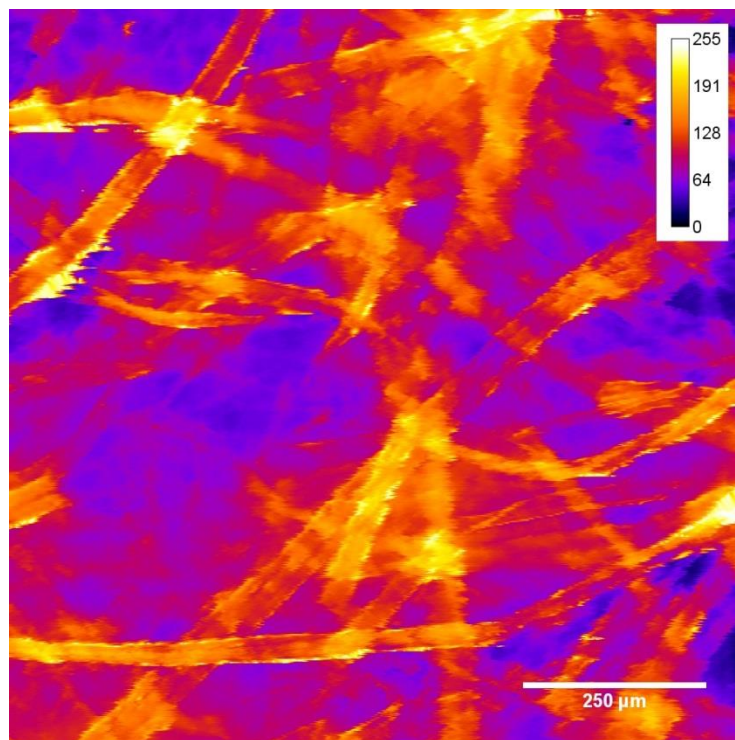


Figure 3.8.2: Topographic image (1 mm × 1mm) of the surface of a film of dried MFC with a small amount of HMDA (6.08×10^{-2} mmol/g MFC), captured by laser profilometer.

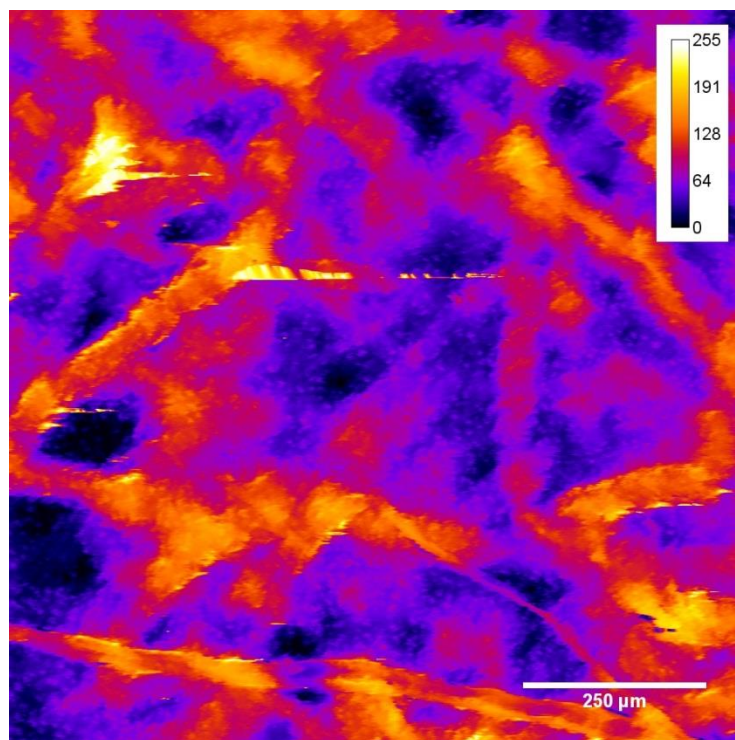


Figure 3.8.3: Topographic image (1 mm × 1mm) of the surface of a film of dried MFC with a large amount of HMDA (6.09 mmol/g MFC), captured by laser profilometer.

3.9 Nano-topographical characterization

As seen in Figure 3.9.2 and Figure 3.9.3, the films were constituted of a dense layer of intertwined nanofibrils. The sub-nm lateral resolution of these images suggests that the smallest observed fibrils may be the elementary nanofibrils and that the somewhat larger structures thus are aggregates of these and not completely fibrillated. Some of the imaged films containing crosslinkers showed the presence of small particles of some kind, as seen in Figure 3.9.4. A representative selection of the images obtained by AFM can be found in Appendix F. The rough trend was the Sq-values increased as a function of crosslinker concentration, as seen in Figure 3.9.1 for the unfiltered images, although the correlation coefficient was quite small (0.5). When the images were divided into different wavelengths using a FFT filter, the largest correlation coefficient (0.74) was for structures in the size range of 20 – 40 nm, as seen in Table 3.9.1. Even so, the variations within the concentrations were large, and the data sets were small, only containing 3 – 4 images.

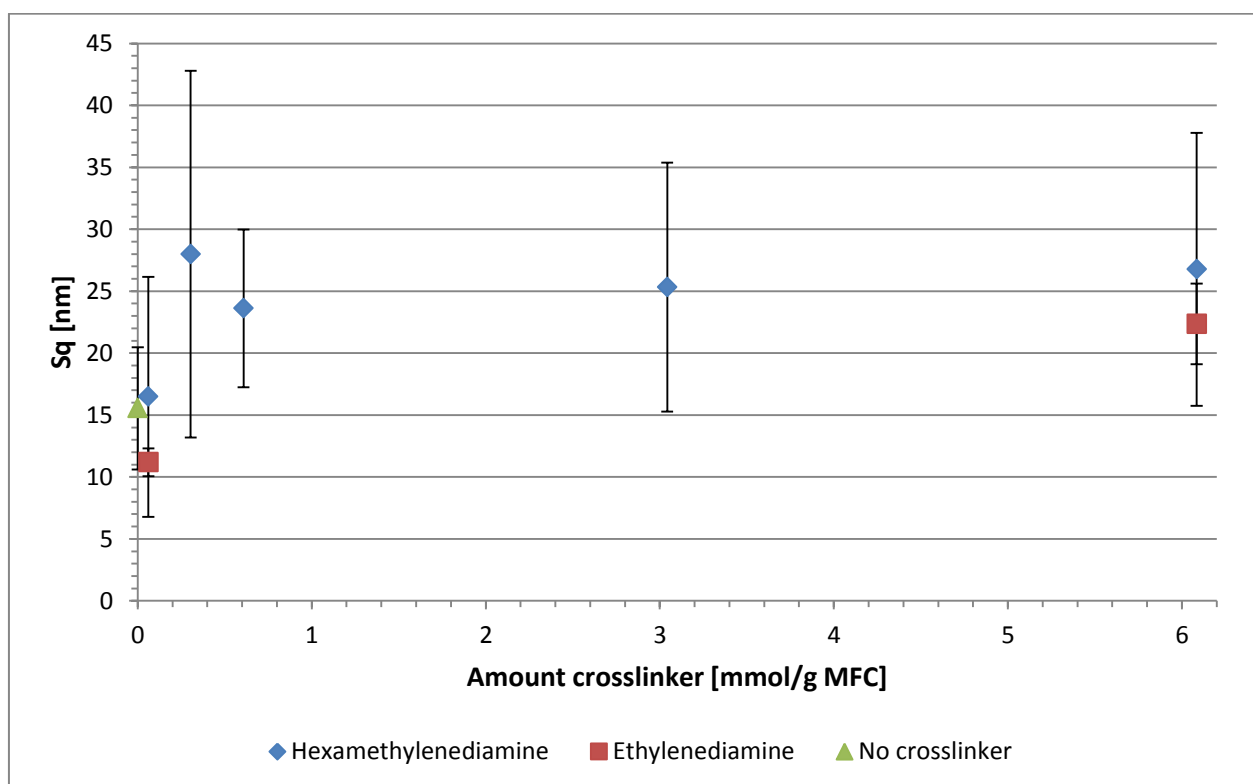


Figure 3.9.1: Root-mean-square deviation surface roughness (Sq) as a function of amount of crosslinkers in the dried films, obtained by processing AFM images using ImageJ. Each concentration is the average of three or four images. The error bars show \pm one standard deviation from the mean.

Table 3.9.1: Sq-values [nm] for the unfiltered AFM images and for the images divided into increasing wavelength [nm] intervals using a FFT filter. The correlation coefficient show a positive correlation ≥ 0.50 between Sq and crosslinker concentration for all wavelengths except < 10 nm (probably due to the small amount of pixels for the smallest wavelength interval.)

Wavelength	Unfiltered	<10	10-20	20-40	40-80	80-160	160-320
E1	11.19	0.38	0.51	0.81	1.20	1.68	2.08
E100	22.35	0.47	0.61	0.92	1.21	1.59	2.33
H1	16.48	0.36	0.48	0.79	1.12	1.50	2.06
H5	27.98	0.37	0.51	0.80	1.13	1.57	2.27
H10	23.62	0.37	0.50	0.82	1.18	1.68	2.44
H50	25.33	0.45	0.64	1.01	1.41	2.02	2.91
H100	26.76	0.37	0.54	0.93	1.35	1.92	2.68
MFC	15.54	0.67	0.55	0.83	1.10	1.43	1.97
<i>Correlation coefficient</i>	<i>0.50</i>	<i>-0.07</i>	<i>0.60</i>	<i>0.74</i>	<i>0.65</i>	<i>0.53</i>	<i>0.61</i>

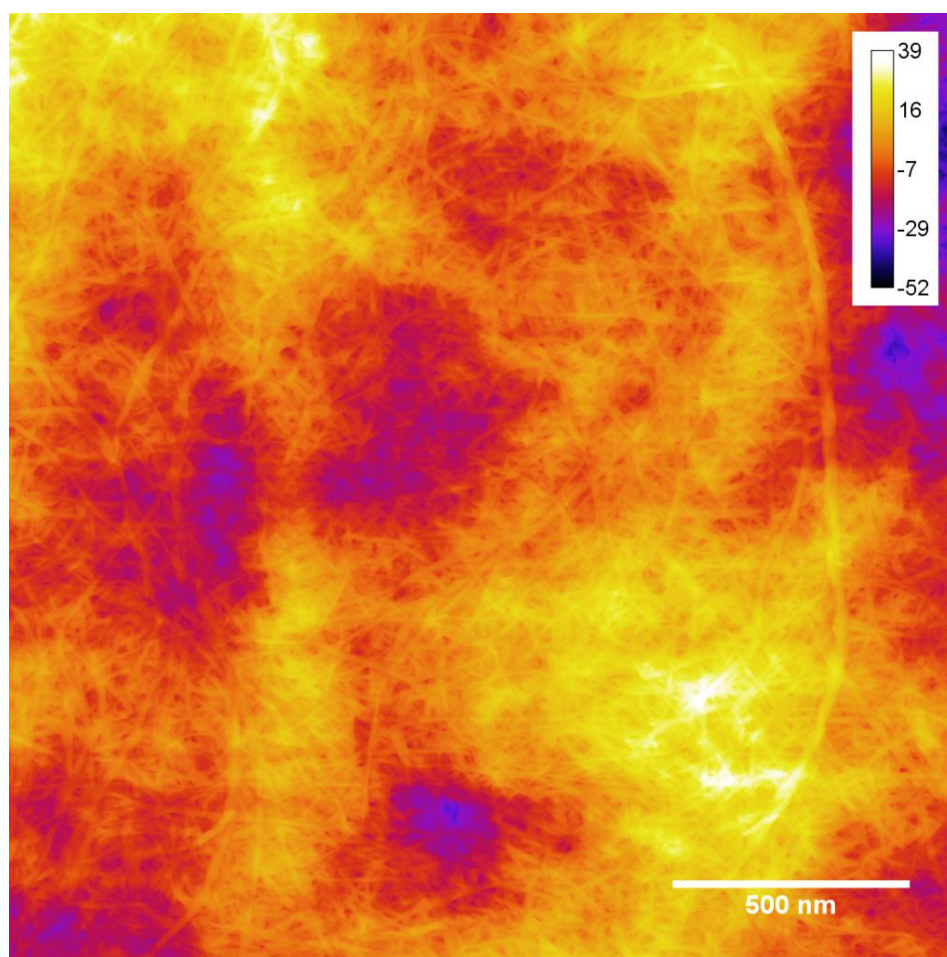


Figure 3.9.2: Topographic image (2000 nm \times 2000 nm) of the surface of a film of dried MFC without crosslinkers, captured by atomic force microscopy, ScanAsyst Auto in air.

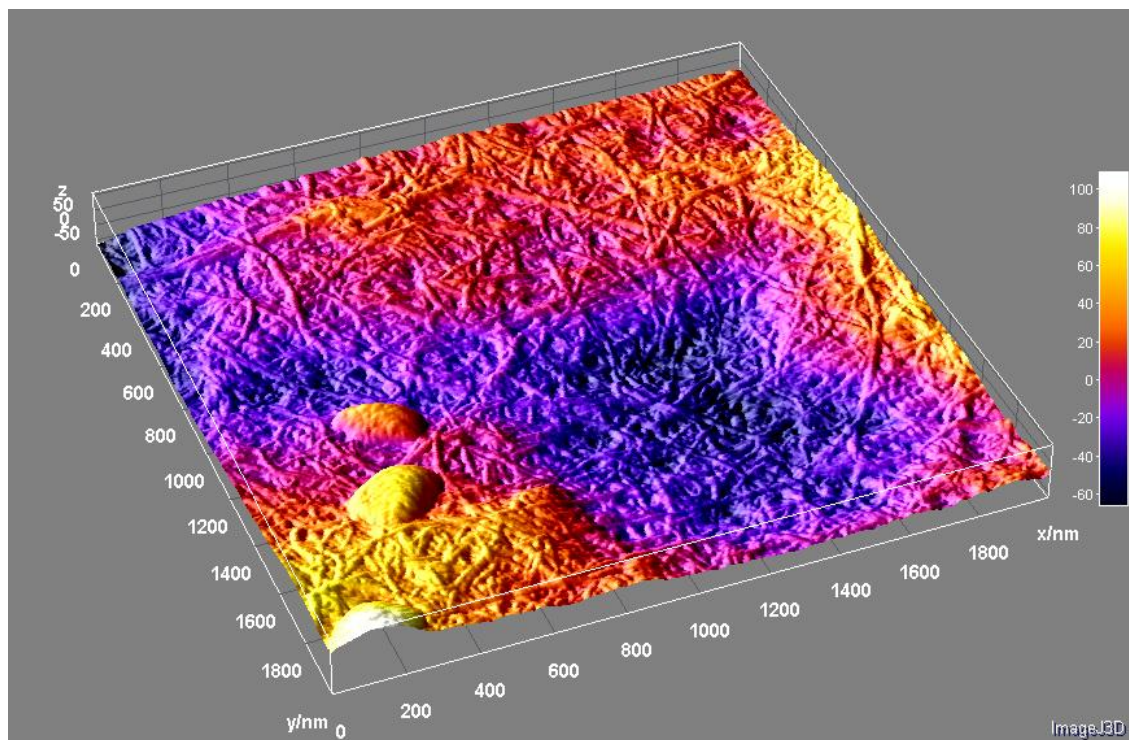


Figure 3.9.3: 3D rendition of a topographic image (2000 nm × 2000 nm) of the surface of a film of dried MFC with a large amount of HMDA (6.09 mmol/g MFC), captured by atomic force microscopy, ScanAsyst Auto in air. The same image can be observed in the figure below.

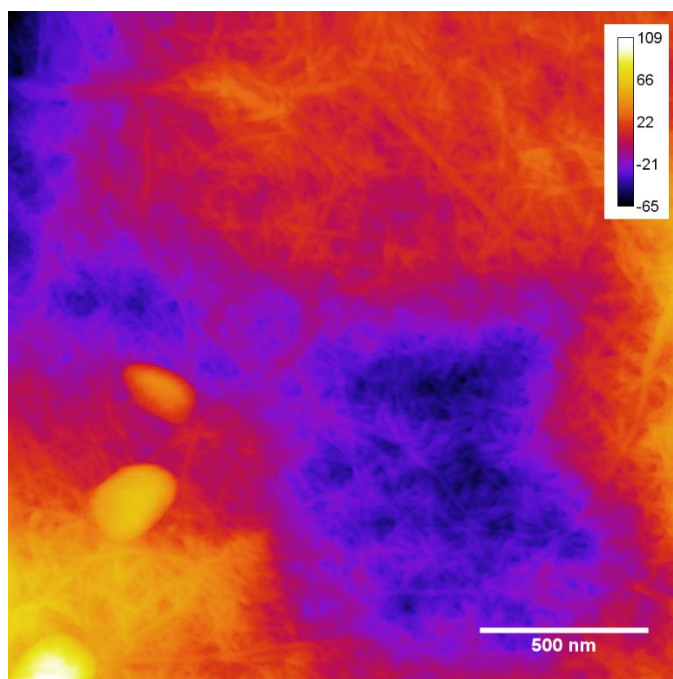


Figure 3.9.4: Topographic image (2000 nm × 2000 nm) of the surface of a film of dried MFC with a large amount of HMDA (6.09 mmol/g MFC), captured by atomic force microscopy, ScanAsyst Auto in air.

3.10 SEM images of MFC films

Coating the surface of the film with 15 nm gold ensured a good signal and disallowed large charge accumulations in the samples. Since the coating layer was more than four times thicker than the theoretical size of the elementary fibrils, these could unfortunately not be properly imaged, even though the theoretical resolution of the S(T)EM was more than adequate for these structures to be observed. The small height variations of the films also made it difficult to obtain proper contrast in SE mode. Residual fibers could be imaged, but increasing the resolution revealed mostly the grains of the coating gold layer, as seen in Figure 3.10.1. Low resolution images also revealed that the surfaces of the films with high amounts of crosslinkers were covered with particles, as seen in Figure 3.10.2. High resolution images revealed the highly crystalline nature of these particles, as seen in Figure 3.10.3

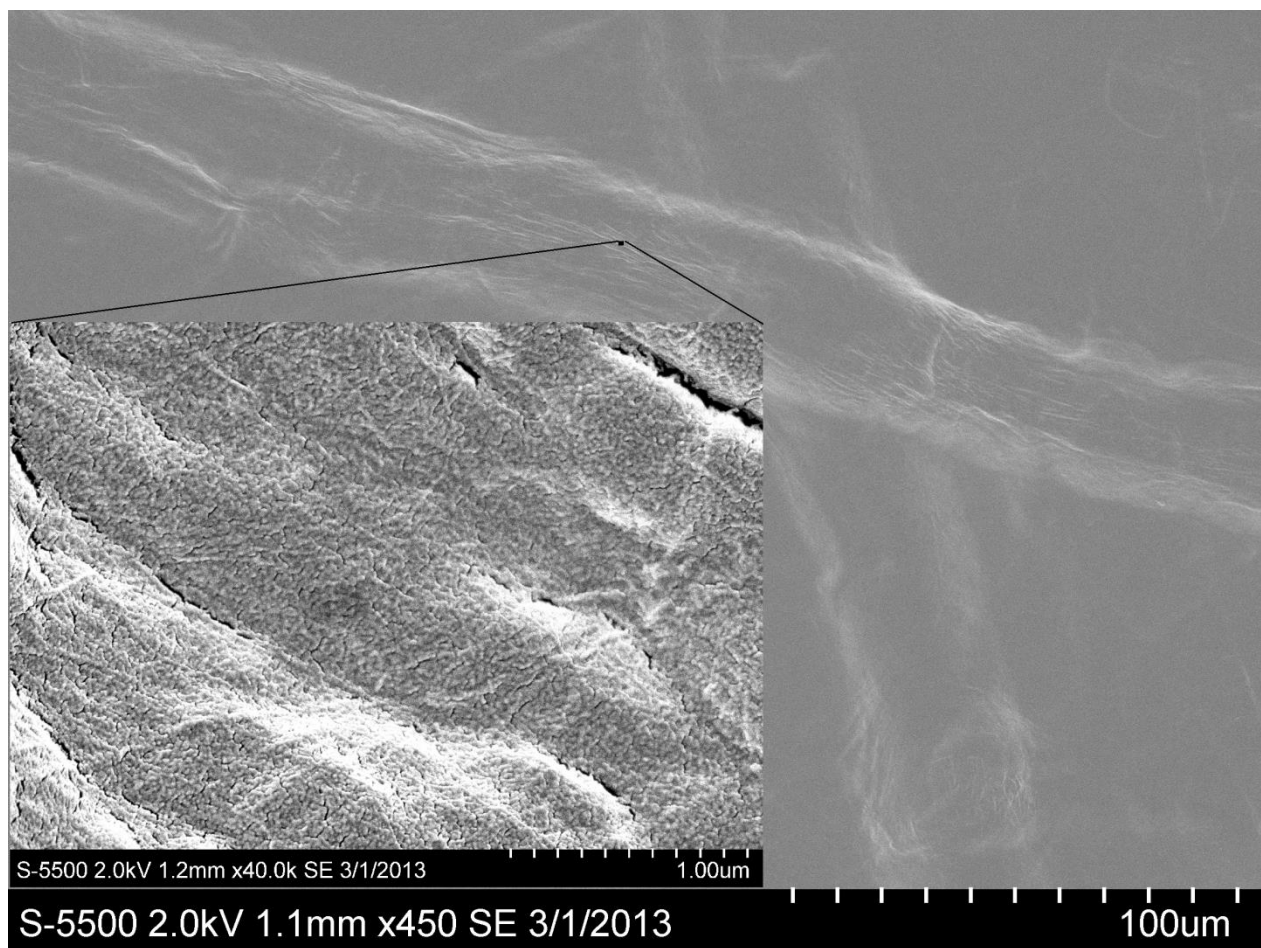


Figure 3.10.1: SEM image of the surface of a dried MFC film coated with 15 nm gold. Residual fibers were present in the film. Increasing the resolution mostly revealed the grains of the coating gold layer.

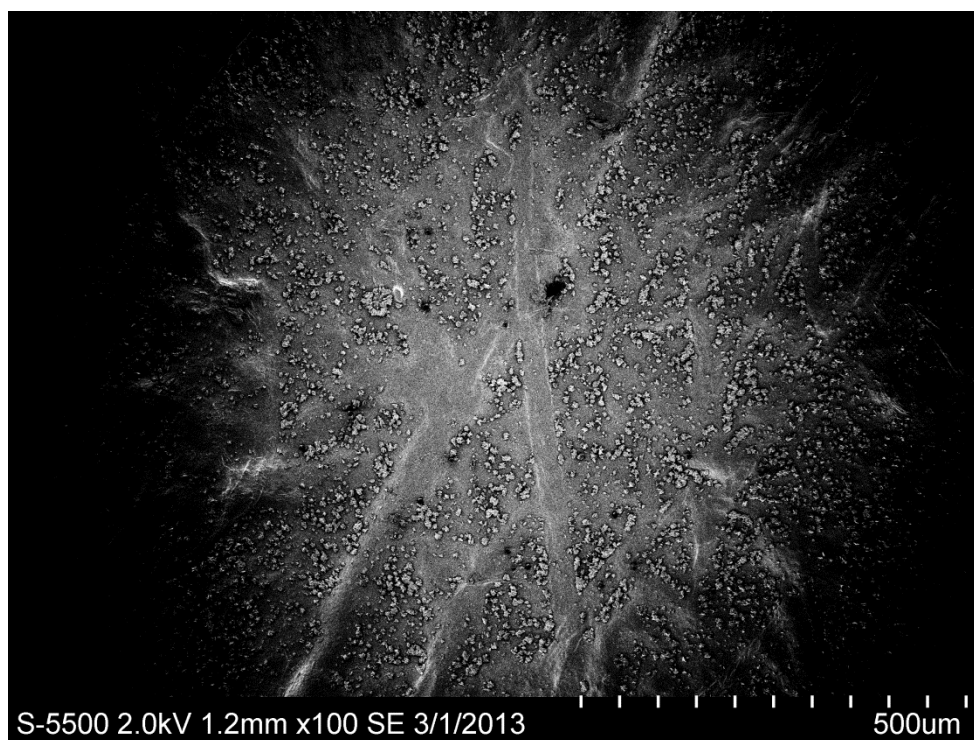


Figure 3.10.2: Low resolution SEM image of the surface of a dried MFC film with high amount of HMDA (6.09 mmol/g MFC). Notice the particles covering the surface.

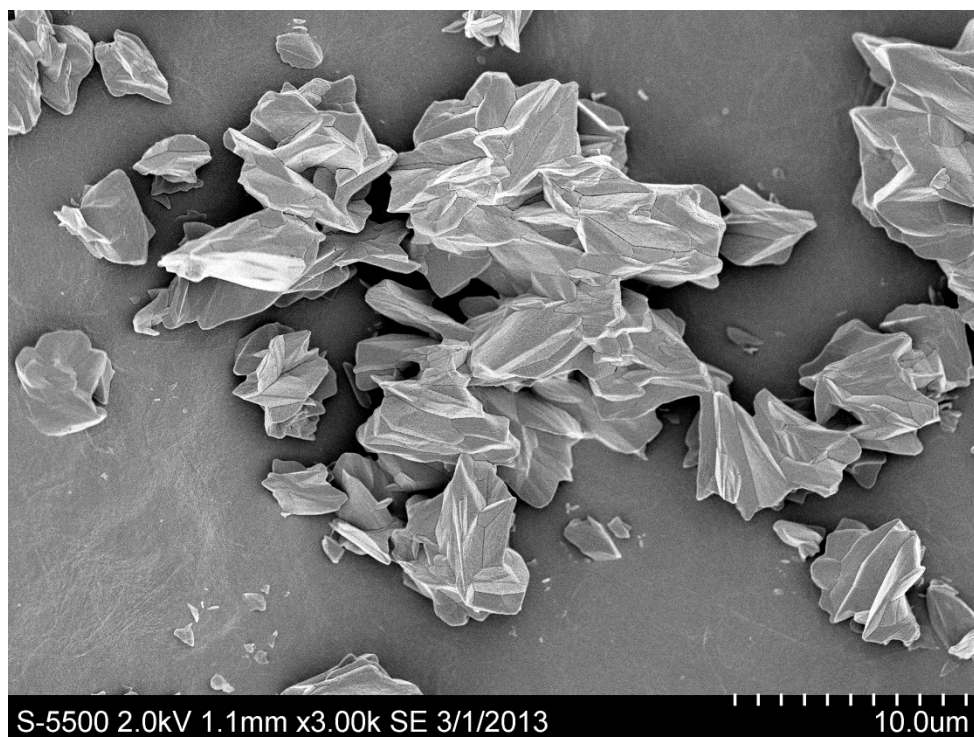


Figure 3.10.3: High resolution SEM image of the surface of a dried MFC film with high amount of HMDA (6.09 mmol/g MFC). Notice the crystalline structure of the particles.

4 Discussion

4.1 Aldehyde and carboxylate content

4.1.1 Conductometric titration

As seen in Section 3.1, the carboxylate contents were reproducible with relatively small standard deviations within all the different parallels. This is in accordance with earlier reports on the conductive titration method; it yields very reproducible carboxylate values for MFC and NCC [42, 43]. The method is quite cumbersome and sensitive to errors introduced by the operator, suggesting that an automated analysis of the results (especially choice of data points for the linear regressions and calculations of the intercepts) could be beneficial. The main problem with using this method for finding aldehyde content is that the calculation is based on a small difference between two data sets (regular and sodium chlorite oxidized MFC) with inherent variations, which are transferred to the final result. Due to the propagation of errors, rather small variations in the carboxylate contents thus yielded larger variation in the aldehyde content (CV = 29.3 % for the first parallel and 23.4% for the second parallel.)

4.1.2 Surface carboxylate and aldehyde content

According to Okita et al. the crystal sizes of the Cellulose I crystalline parts of a nanofibril from softwood are $C_1 = 3.5$ nm and $C_2 = 4.1$ nm, yielding an average crystal size of $C_A = 3.8$ nm [21]. Assuming that every second surface monomer is facing into the crystal, Equation (4.1.1) can be used to calculate the relative number (mol/mol of total anhydroglucose units in cellulose) of exposed C6 surface groups on the crystalline parts of an elementary nanofibril:

$$n = \frac{C_A / 0.61 + C_A / 0.53}{(C_A / 0.61 + 1)(C_A / 0.53 + 1)} \quad (4.1.1).$$

The numerical values 0.61 and 0.53 are the d -spacings of the Cellulose I crystal structure, as seen in Figure 4.1.1. Equation (4.1.1) yields 22.7% as the amount of anhydroglucose units with the C6 groups exposed on the surface of nanofibrils from softwood.

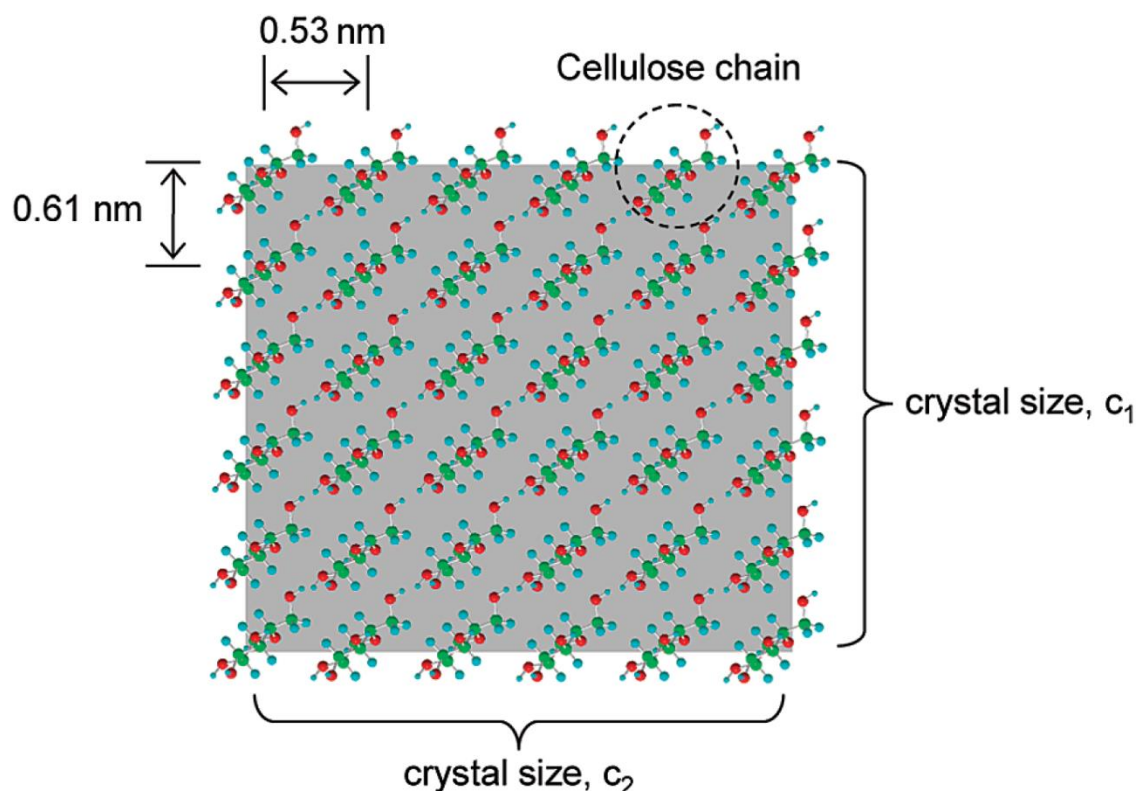


Figure 4.1.1: Schematic model of the cross section of the Cellulose I crystalline part of an elementary cellulose nanofibril. (Adapted from [21].)

The second conductometric titration parallel was comprised of more replicates and ten times more data points than the first parallel, so it is a plausible assumption that this was more accurate than the first parallel. Hence the total amount of oxidized groups (DO) was 16.7%; i.e. 13.5% carboxylate groups and 3.1% aldehyde groups. Dividing these values by 22.7% yields that 59.5% of the total surface C6 groups were oxidized to carboxylate, and 13.7% were oxidized to aldehyde. Assuming that the aldehyde groups were uniformly distributed over the surface of the elementary nanofibrils (which they probably were not), there were approximately nine C6 surface groups (hydroxyl or carboxylate) between each aldehyde group. In addition, there were also two hydroxyl groups between each C6 group, as can be seen in Figure 1.4.3. The calculated aldehyde content is a reasonable value when compared to reported values from the literature (0.25 mmol/g MFC when TEMPO-oxidized with 3.8 mmol NaClO/g cellulose; see Table 1.5.1). Although the total DO to aldehyde (3.13%) is a relative small value, the argument above shows that the surface aldehyde coverage was large enough (13.7%) that it is reasonable to assume that crosslinks between these could have formed and thus affected the elasticity of the gels.

4.2 On the nature of MFC gels

The observed behavior of the MFC suspensions and the values measured by dynamic measurements, were coherent with and in the same range as similar measurements performed by Paakko et al. on enzymatically pre-treated MFC [10]. On the other hand, Saito et al. reported the formation of low concentration (0.10% – 0.80%) cellulose nanofibril hydrogels with storage moduli almost an order of magnitude higher than strong agarose hydrogels [58]. This was obtained simply by decreasing the pH from eight to two in suspensions of cellulose nanofibrils, where the surface groups of the fibrils had been completely converted to carboxylate groups by TEMPO-mediated oxidation followed by oxidation with sodium chlorite. The reported G' value of 0.80% cellulose nanofibrils by Saito et al. was approximately 30 kPa, more than 200 times higher than the G' values measured in this project at the same concentration of MFC.

4.2.1 Concentration dependence

According to Saito et al., the plateau storage modulus, G'_p , of a semiflexible fiber network with fiber concentration c follows the simple relation seen in Equation (4.2.1):

$$G'_p = Ac^\alpha \quad (4.2.1),$$

where A is a constant related to the properties of the individual fibers and the power α indicates the dependence on the fiber concentration [58]. Plotting the G' values from the VLR for the three concentrations in Section 3.3.1 as a function of concentration and using power law regression in Microsoft Excel 2010 yields $A = 6 \times 10^8$ and $\alpha = 3.1581$, with $R^2 = 0.9957$. Paakko et al. found that the concentration was dependent on a power of approximately three [10]. Saito et al. reported $\alpha = 2.5$ for the cellulose nanofibril hydrogels, and stated that the power value was related to the network structure of the gels [58]. A numerical value for A was not stated, only that it was unprecedentedly high, but it must be much higher than the value found in this project due to the higher G' values reported by Saito et al. This suggests that the fibrils used in the hydrogels produced by Saito et al. had very high elastic moduli and aspect ratios, even more so than the nanofibrils used in this project. A possible explanation for this could be milder mechanical treatment during homogenization by these authors. This shows the importance of

keeping the structure of the nanofibrils as intact as possible, if the goal is to produce strong hydrogels.

4.2.2 Cox-Merz rule and nature of interactions

The frequency sweeps shows that the MFC used in this project formed a stable gel network for a frequency range from 0.01 – 10 Hz, i.e. for observation times from 0.1 – 100 seconds. This suggest that the forces linking the nanofibrils together had average relaxation times longer than 100 seconds, but it cannot be used to deduce the exact nature of these interactions. The viscosity measurements show that the MFC showed pseudoplastic (shear thinning) behavior when subjected to an increasing shear rate or angular frequency. This can be explained by the alignment of the nanofibrils with the flow of the suspension at larger shear rates. The sample did not directly follow the empirical Cox-Merz rule, although the dynamic and steady state viscosities could be made to approximately overlap by introducing a factor α , the size of which differed depending on the concentration (data not shown). A departure from the Cox-Merz rule usually suggests that long-range interactions are present in the network, and that the intermolecular interactions are enthalpic rather than purely topological entanglements [59]. The dynamic viscosity was measured at non-disruptive strains within the VLR, while the steady state viscosity was measured at increasing, disruptive strains. The presence of more stable connections than pure entanglements, which were disrupted at the steady state but kept intact at the oscillating measurements, would explain the lower steady state viscosity values.

4.2.3 Dependence on pH

The decreased storage modulus and viscosity when adding HMDA were probably due to increased electrostatic repulsion between the C6 carboxylate groups. Both amine groups on HMDA are basic, with pK_a values of 11.86 and 10.76, according to the Wolfram Alpha database [60]. The pH measurements (see Section 3.5) revealed that even after successful crosslinking into gels, the pH of the gels was basic. Since the carboxylate groups have pK_a values around 3 – 4 [58], increasing the pH to basic levels by adding the HMDA solution most likely led to the deprotonation of more carboxylate groups, increasing the electrostatic repulsion between the nanofibrils. The most likely stabilizing forces in the MFC suspension were topological entanglements (which almost certainly were present due to the large aspect ratio of the

nanofibrils) and hydrogen bonds between non-oxidized hydroxyl groups. Even if all the C6 hydroxyl groups had been oxidized into carboxylate, there are two more hydroxyl groups facing out of the nanofibril between each C6 group, as can be seen in Figure 1.4.3. When unprotonated carboxylate groups were in proximity of each other, the repulsive force between these would counteract the attractive hydrogen bonds between the surface hydroxyl groups. Decreasing the pH to two as done by Saito et al., should thus protonate the carboxylate groups and remove the repulsive interactions between the fibrils [58]. The vast surface area of the nanofibrils in a fully fibrillated material would yield a huge number of hydrogen bonds, which could account for the large storage modulus values reported by Saito et al.

4.3 Crosslinking

4.3.1 Ionic or covalent crosslinks

The diamine crosslinkers may have contributed to the increased elasticity by two different interactions; forming Schiff bases with the aldehyde groups and by attractive ionic interactions with negatively charged carboxylate groups. The measured pH values in the gels suggest that both amine groups were protonated and thus positively charged ($\text{pH} < \text{pK}_a$ values), and that the carboxylate groups were deprotonated (basic $\text{pH} > \text{pK}_a$) and thus negatively charged. This suggests that some part of the increased elasticity may have been due to ionic attractive interactions between amine groups on the crosslinkers and carboxylate groups on separate nanofibrils. For such ionic crosslinks to contribute to an increase in elasticity, the added contribution would have to be larger than the decrease in elasticity due to the deprotonation and subsequent repulsive interactions between the carboxylate groups upon addition of the basic diamines.

The (qualitatively observed) correlation between color change and Young's modulus suggest that at least some of the strengthening interactions were of covalent nature. The hypothesis that the color change was caused by Schiff bases is supported by literature, as Schiff bases are well known for giving rise to colors, often in the yellow-brown range of the spectrum [61]. Adding 2-picoline-borane yielded approximately equal Young's moduli for equal concentrations of HMDA (see Figure 3.4.5), but no significant change in color compared to MFC without

crosslinkers. Since 2-picoline-borane have been shown to reduce Schiff-bases to amine linkages, it is reasonable to assume that at least part of the observed increase in elasticity is due to covalent bonds between diamines and aldehydes [27, 28]. A simple method to investigate the contribution from such covalent bonds would be to oxidize all remaining aldehyde groups to carboxylate with sodium chlorite, and see if any gelling still would occur upon addition of crosslinkers. For simplicity, the subsections below are based on the assumption that the main contribution to the increased elasticity was the formation of Schiff bases, although the arguments are valid if the interaction were of an attractive ionic nature instead.

4.3.2 Crosslinker length and concentration

There were several factors that contributed to the increased elastic modulus (both Young's modulus and shear storage modulus) observed in this project. For a successful crosslinking to occur, the diamine crosslinker must be in a position to form attractive interactions between both its amine groups and the surface of the nanofibrils. If only one amine group is attached to the nanofibrils, the crosslinker will not contribute to the elasticity of the network. Thus all factors increasing the probability for attachments of both amine groups will increase the elasticity.

Crosslinker length seems to be an important factor, as seen in Figure 3.4.3. The crosslinker chain is comprised of single C-C bonds, and since each of these are free to rotate, a longer chain will be more flexible than a shorter chain. The longer and more flexible chain of HMDA possibly increased the probability for the second amine group to reach an aldehyde group on a separate nanofibril after the successful Schiff base formation of the first amine group. This was also supported by the observation that melamine did not seem to form enough crosslinks to yield any qualitatively observable differences in viscosity, possibly due to the lower flexibility, higher bulk volume, and more steric hindrance of the triamine.

Crosslinker concentration was the other main factor that was investigated in this project. As Figure 3.4.3 and Figure 3.4.5 shows, as long as the time at 80° C did not vary with more than a few hours, crosslinker concentration (in addition to crosslinker length) was the main factor correlating with Young's modulus. Higher crosslinker concentration, at least up to a saturation

point, should increase the probability for an amine to come in proximity to an aldehyde and subsequently forming a Schiff base. For the MFC used in this project, this concentration seemed to be somewhere between 6.12×10^{-1} mmol/g MFC 3.05 mmol/g MFC. Assuming the aldehyde concentration of 0.181 mmol/g MFC was correct, this corresponded to a ratio between amine and aldehyde approximately in the range of 6.8 – 33.7.

In the samples with much surplus crosslinkers, the laser profilometry images and SEM images suggest that these may have crystallized, at least upon drying the crosslinked MFC. This is especially noticeable in the films, as seen in the laser profilometry image in Figure 3.8.3. These particles might also explain the increase seen in Figure 3.8.1 in Sq-values at the higher crosslinker concentrations. The SEM images of the films in Section 3.10 show that the particles covering the film had a fairly similar size and crystalline structure, implying that these probably not were regular dust particles. The SEM images of the freeze fried gels were more ambiguous, but especially the gels with high concentrations of EDA seemed to contain similar particles. One of the main reasons for calculating the surface roughness of the films was to investigate whether the possible presence of crosslinks would make the films smoother or rougher by bonding the nanofibrils closer together. Such concentration dependence should probably have been more pronounced in the AFM images, which focused on the nanofibril topography, than in the LP images, which focused on the microfibril topography. The opposite was observed, and a possible explanation for the concentration dependence of the LP images has already been discussed. In the AFM images, no significant trend could be observed, as the variations in each data set and thus the standard deviations were larger than the variations between the different concentrations. Dividing the values into wavelengths yielded somewhat better correlation, but not enough to yield convincing results. This reveals one of the major drawbacks for using AFM for quantitative investigations; due to the image capturing process being so time consuming (> 20 minutes/image for high quality images), it is difficult to achieve large enough data sets to obtain statistically relevant results.

4.3.3 Time dependence

Before adding the crosslinkers, all aldehyde groups should be available for crosslinking, and as more and more Schiff bases are formed, the free crosslinkers must travel further through the

gel matrix to reach an available aldehyde group. Figure 3.3.4 and Figure 3.3.5 shows that there was a rapid increase in the storage moduli before reaching plateau values. The reason for such plateaus may have been that no more aldehyde groups were available for Schiff base formation. The time-lapsed measurements shown in Figure 3.4.4 shows that the cast gels possibly had not reached a similar saturation point at the time of the measurements in Figure 3.4.3 and Figure 3.4.5. The Young's moduli values were thus probably measured on gels not yet at their full strength. Inserting the plateau storage modulus (≈ 1375 Pa) from Figure 3.3.5 into the Poisson relationship (see Section 1.7.1), and assuming an incompressible, ideal material ($\mu = 0.5$) yields a theoretical Young's modulus of approximately 4.1 kPa for the gels with 0.80% MFC and 3.05 mmol HMDA/g MFC. Since only one replicate was obtained using the rheometer, this value is not nearly statistically significant, but it hints that the plateau Young's modulus for the cast gels possibly was < 4.1 kPa. Using the plateau storage modulus from Figure 3.3.5 and Young's moduli from the three different parallels of H50 cast gels, approximate values for Poisson's ratio μ can be calculated. The two first parallels, which were measured after approximately 18.5 hours, yields $\mu \approx 0.17$. The third parallel, measured after approximately 23.5 hours, yields $\mu \approx 0.25$. Both these values are within the interval $-1 \leq \mu \leq 0.5$.

One of the main differences between the gelling process of the cast cylindrical gels and the samples gelling in the rheometer was the constant, small strain oscillation in the rheometer. A plausible explanation for the faster gelling in the rheometer could be that the oscillating strains, which were too small to disrupt the structure of the gels, actually relocated the crosslinkers faster than simple diffusion would do, thereby increasing the gelling rate. A fairly straightforward way of investigating this using the rheometer could be to add the MFC to the rheometer after stirring in the crosslinkers, and heat the sample for some time before initiating the measurement and thus the oscillations. If it was to be found that the small strain oscillations increased the gelling rate, the next step could be to investigate whether adding small vibrations to the gel casting process, e.g. by ultrasound, could increase the rate of gelling when using casting molds.

4.3.4 Temperature dependence

The qualitative observation was that the gels needed higher temperatures to occur; the pre-film solutions did not gel in the petri dishes before being put in a heating cabinet, and the 0.25% MFC gels in the test tubes did not gel until being put in a water bath. However, the small strain oscillation in the rheometer at a constant temperature of 20° C shown in Figure 3.3.6 suggest that some gelling may have occurred in the samples even at approximate room temperatures. This was somewhat contradicted by the behavior of a similar gel shown in Figure 3.3.7, where the storage modulus did not show a similar increase after the crosslinked structure had been disrupted by large strains above the VLR. The literature is ambiguous on the need for higher temperatures for Schiff base formation; Han et al. reported best effect at 80° C [23]. Bartos and Pesez reported Schiff base formation at room temperature [61]. A plausible explanation for the increased gelling rate at higher temperatures could be the larger fluctuations (increased diffusion coefficient) of the crosslinkers at higher temperatures, according to the universal Einstein relation [62]. Larger fluctuations and higher diffusion rate would increase the probability for the amine groups to come in proximity of aldehyde groups in a shorter time period.

4.4 Residual fibers

The estimated amount of residual fibers from the FiberMaster were 7.57% (1SD = 0.28%). The lower resolution limit for the FiberMaster system is 6 $\mu\text{m}/\text{pixel}$, as mentioned in Section 2.12, meaning that the estimation of 7.57% only accounts for fibers and poorly fibrillated fibrils with diameters in the μm -range. Since the FiberMaster did not detect fibrils with a smaller diameter than its resolution limit, this value is an underestimation. The presence of residual fibers is also clearly visible in the LP and SEM images. The size distribution of the nano- and microfibrils was probably continuous, with the highest peak at the lowest fibril diameters. This is because there were a much higher number of the smallest diameter nanofibrils than of the larger, not completely fibrillated nano- and microfibrils. As shown in Figure 4.4.1, the films seemed to be comprised of a large number of approximately equally sized small nanofibrils, and some larger fibrils which seem to be comprised of a large number of aggregated, non-fibrillated nanofibrils. Note that these larger fibrils were probably still too small to be detected by the FiberMaster.

Even if the residual fiber estimate is an underestimation, this ratio is a mass percentage. The surface area ratio of the residual fibers would have been miniscule compared to the surface area ratio from the smallest nanofibrils, due to the sheer number of these. The elastic properties of the gels are dependent on the continuous network of fibrils, which again is dependent on interactions between the fibril surfaces. Hence almost all the elasticity of the gels should have been due to the contribution from the smallest fibrils.

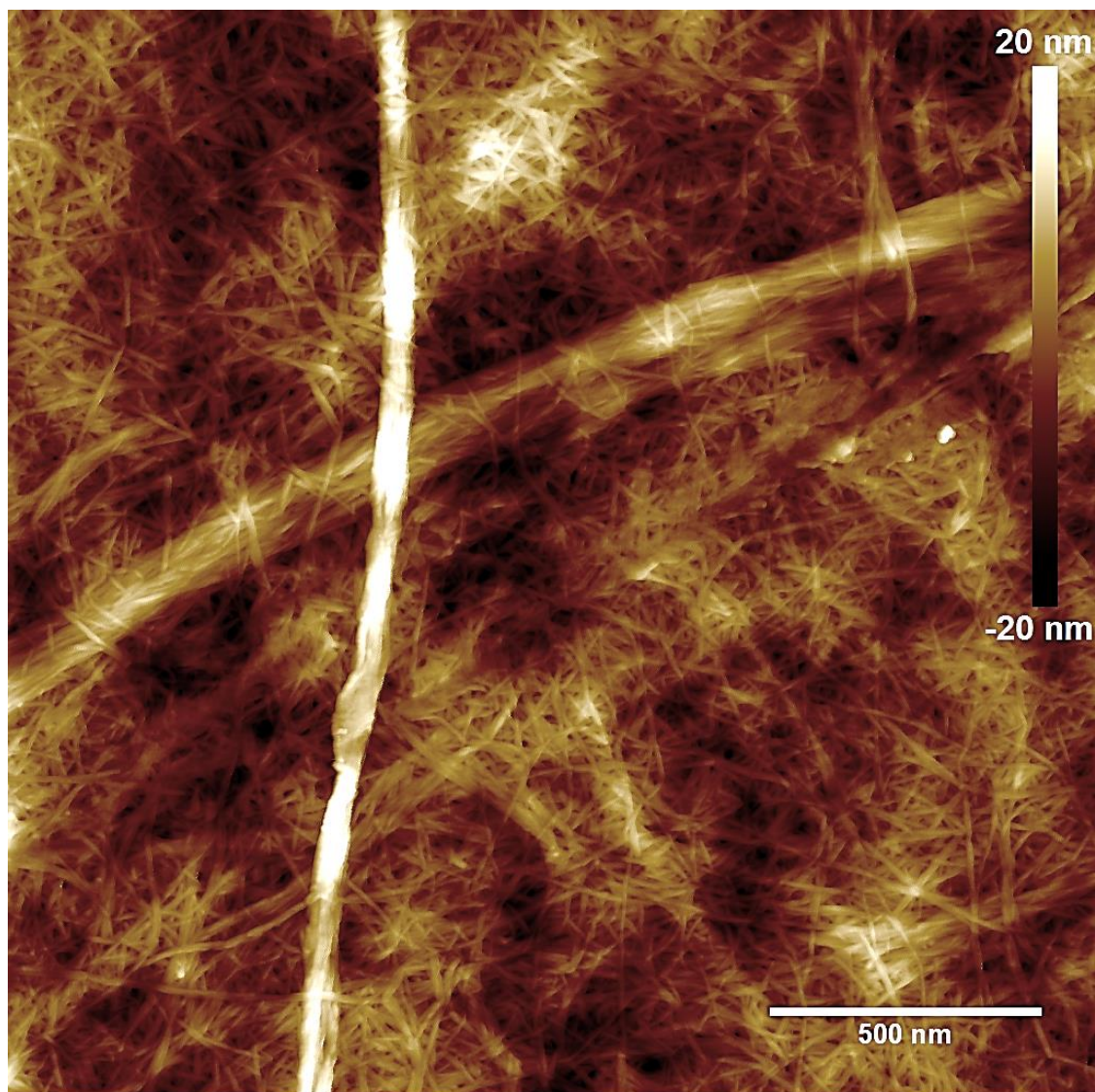


Figure 4.4.1: Topographic image (2000 nm × 2000 nm) of the surface of a film of dried MFC with a small amount of EDA (6.14×10^{-2} mmol/g MFC), captured by atomic force microscopy, ScanAsyst Auto in air. The image have been processed using a 3rd order flatten function in the NanoScope Analysis Software (v.1.40, Bruker Corporation), and the sharpness and brightness of the image have been increased, to focus on the topography of the smallest nanofibrils.

4.5 Biomedical applications

4.5.1 Controlling elastic modulus

Comparing the Young's moduli measured in this project with the elastic moduli exhibited by solid tissues in the body (see Figure 1.6.1) suggest that the crosslinked MFC gels show approximately the same elasticity as brain tissue, which is one of the softest types of solid tissue found in the body [34]. To mimic harder tissues such as muscle or cartilage, the elastic moduli of the MFC gels would have to be increased much more than values achieved in this project. The results from Saito et al. suggest that it should be possible to reach the necessary elastic moduli using TEMPO-oxidized nanofibrils [58]. As mentioned in Section 4.2.3, the pH measurements in this project shows that the pH in the gels was basic and that the carboxylate groups probably weakened the gels by electrostatic repulsion, assuming that this repulsion is not totally opposed by possible electrostatic attraction by the diamines. Hence, a possible method for increasing the elasticity of the gels could be to decrease the pH after the Schiff base formation reaches saturation. According to Saito et al. the strengthening of the gels after the pH was lowered was not very reversible when increasing the pH again [58]. As seen in Figure 3.4.3, there is probably nothing to gain by further increasing the crosslinker concentration. It is possible that using even longer crosslinkers than HMDA, e.g. dodecamethylenediamine, would further increase the elastic moduli of the gels. Another option could be to increase the concentration of MFC.

4.5.2 Removing surplus crosslinkers

A very important issue that must be resolved before gels such as these could be used for biomedical applications is the removal of surplus crosslinkers. The increase in pH when immersing the gels in water suggests that surplus crosslinkers diffuse out of the gels. A possible explanation for the subsequent decrease in pH over time might be that some of the free crosslinkers diffuse back into the gel again and attach to previously inaccessible aldehyde groups. A possible washing procedure could involve simply immersing the gels in water and letting the surplus crosslinker diffuse out of the gels, replacing the water and repeating the procedure until no change in pH can be measured.

4.5.3 Toxicity

HMDA is generally moderately toxic by most routes of administration, with oral LD₅₀ values ranging from 750 – 1500 mg/kg for rats [63]. It is extremely irritating to skin and eyes, but it shows limited systemic damage, and is quickly absorbed and metabolized in rats. It is approved for several uses in polymers for food or skin contact applications, i.e. not in a free form but linked with larger structures [63]. This suggests that HMDA is less harmful when covalently linked into the MFC network. Even though cellulose fibers have been used for many years without any harmful effects, the cytotoxicity of the nanofibrils with their much smaller proportions has to be examined as well. Alexandrescu et al. showed that cellulose nanofibril structures produced from TEMPO-oxidized softwood and hardwood pulp fibers did not exert any acute toxic phenomena on 3T3 fibroblast mouse cells [4]. Samples crosslinked with polyethyleneimine (PEI) did however show a significant reduction in cell viability. PEI is a much longer molecule than the short crosslinkers used in this project, but the cytotoxicity of the crosslinked nanofibrils is an important issue that must be investigated further before these gels could be used for biomedical applications.

4.5.4 Covalent vs. weaker interactions

Saito et al. managed to produce much stronger gels than the gels produced in this project, without introducing any covalent crosslinks [58]. This shows that even though a gel is only held together by weak interactions such as topological entanglements and hydrogen bonds, the sheer number of these in a nanofibril network can produce very strong gels. The main advantage with covalent crosslinks is thus not necessarily the strength of the interactions, but the stability. As mentioned in Section 1.6 the attractive interactions in a physical gel are reversible, meaning they can be disrupted by changes in physical conditions such as ionic strength, pH, temperature, application of stress, or addition of specific solutes (depending on the type of interaction.) In theory, the Schiff bases are reversible in water, although no such reversibility was observed in this project. The gels were remarkably stable in water, and had to be stirred violently for > 10 minutes to be dissolved for the pH measurements shown in Figure 3.5.2. This can be observed in Figure 4.5.1, which shows a gel with 6.12×10^{-1} mmol HMDA/g MFC during and after approximately five minutes of violent stirring. To further stabilize the

covalent links by reducing them to amine linkages, 2-picoline-borane seems to be a suitable and non-toxic reduction agent. This stability even at water content > 99% make the gels produced in this project interesting materials for biomedical applications.

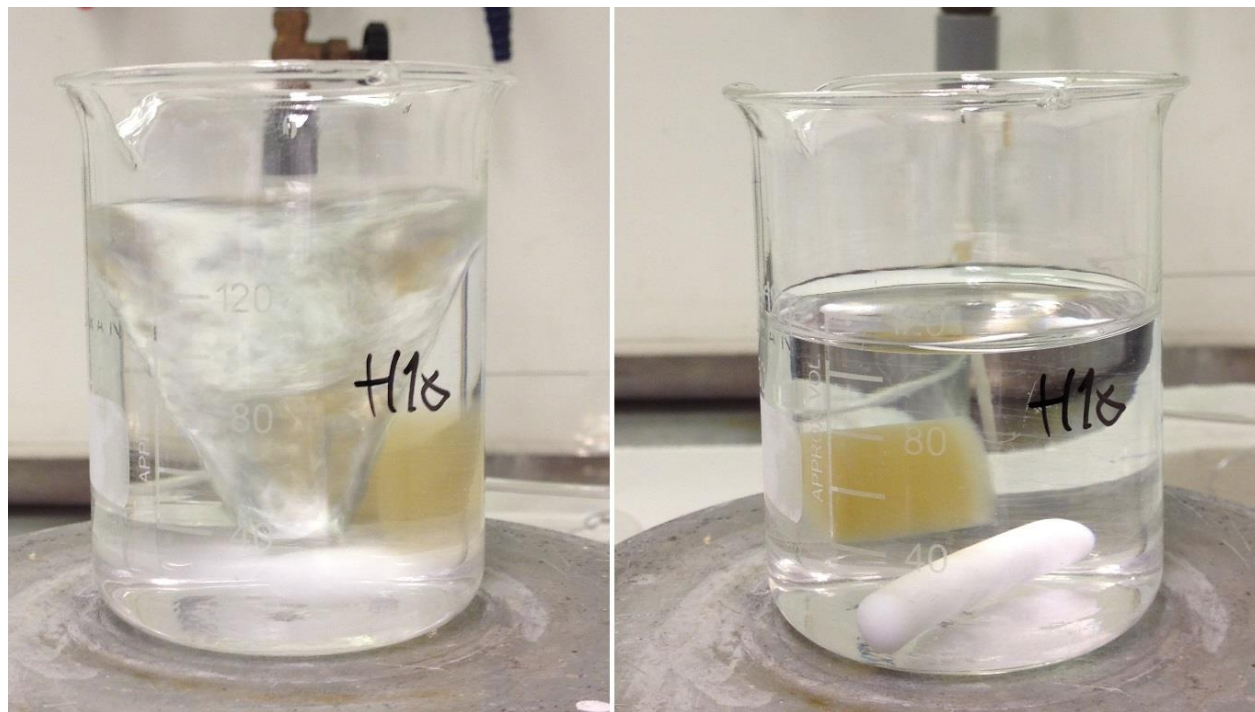


Figure 4.5.1: Gel with 6.12×10^{-1} mmol HMDA/g MFC, during violent stirring (left) and after approximately five minutes of stirring (right).

4.5.5 Water absorbance

The measured moisture content and water absorption values of the freeze-dried gels (see Section 3.6) show that the gels can reabsorb water almost to the same moisture content as before they were dried. That the values were slightly lower may have been a result of lesser water absorbance by the denser sheet-like structure. Also notice that the water reabsorbance seems to be lower in the stronger gels. A possible explanation for this could be that the nanofibrils were more densely packed in the stronger gels, due to more crosslinks.

5 Conclusion

The main goal of this project was to investigate whether the elastic properties of MFC suspensions pre-treated by TEMPO-mediated oxidation could be controlled by inducing crosslinks with small di- or triamines between the nanofibrils. Using conductometric titration, the total carboxylate and aldehyde content in the MFC was measured as 0.810 mmol/g MFC and 0.181 mmol/g MFC, respectively. It was calculated that this corresponded to 59.5% of the surface C6 groups on the nanofibrils being oxidized to carboxylate, and 13.7% to aldehyde.

The viscoelastic properties of the MFC were investigated by dynamic measurements. The MFC showed a viscoelastic response (i.e. the VLR) for strains approximately < 0.04 , and gel-like behavior ($G' > G''$, δ constant and $< 45^\circ$) for frequencies from 0.01 – 10 Hz. The storage modulus for 0.80% MFC was approximately 125 Pa, and the storage modulus showed a power law dependence on concentration with a power of approximately three. Viscosity measurements showed that the MFC showed pseudoplastic (shear-thinning) behavior, probably due to alignment of the fibrils at higher shear rates. The viscosity did not follow the Cox-Merz rule, with the dynamic viscosity being approximately ten times higher than the steady state viscosity when $\omega = \dot{\gamma}$. This may be explained by a large number of hydrogen bonds between the nanofibrils.

Upon addition of basic HMDA without heating the sample, both viscosity and storage modulus decreased. A probable explanation for this is that the basic diamine increased deprotonation of the carboxylate groups in the nanofibrils, thus increasing electrostatic repulsion. When the temperature was increased to 80° C, the storage modulus increased rapidly to a plateau of approximately 1375 Pa in a sample with 0.80% MFC and 3.05 mmol HMDA/g MFC, suggesting gelling of the sample.

Small, cylindrical gels were successfully cast at a concentration of 0.80% MFC with different concentrations of HMDA and EDA. Young's modulus was measured by longitudinal compression, and correlated well with increasing crosslinker concentrations before reaching plateau values at approximately thirty times more amine than aldehyde. The gels with HMDA were almost twice as strong as the gels with EDA. Young's modulus was largest (approximately 3220 Pa) at HMDA concentrations of 3.05 mmol/g MFC. There was a clear color change from the grey color of the

regular MFC to a yellow-brown color, qualitatively correlating with both crosslinker concentration and measured Young's modulus, as the gels were heated for approximately 20 hours at 80° C. This color change was attributed to the presence of Schiff base covalent links between amine and aldehyde. When the non-toxic reduction agent 2-picoline-borane was added to the gels prior to heating, no color change was visible, but the gels reached almost equal Young's moduli.

Some of the cast gels were freeze-dried, and revealed a sheet-like pore structure under SEM imaging. The freeze dried gels showed remarkable water absorption values of approximately 8000% for pure MFC gels and 4000% for gels with HMDA.

Films were also prepared with only MFC and with concentrations of crosslinkers equal to those in the cast gels. These were imaged with laser profilometry and atomic force microscopy, and the images were analyzed for a correlation between surface roughness and crosslinker concentration. No significant correlation was observed in the AFM images, but the LP images showed a higher surface roughness at the highest crosslinker concentrations. This was attributed to crystallization of surplus crosslinkers. The crystalline nature of these particles was confirmed by high resolution SEM.

For further studies, it is important to keep either heating time or crosslinker concentration constant, as this project shows that both factors contribute to the final strength of the gels. It would also be interesting to investigate whether the Schiff base formation would occur at a significant level at lower temperatures than 80° C, and if the gelling time could be decreased by adding small vibrations, e.g. ultrasound, to the system. If this gel system is to be used for biomedical applications, the cytotoxicity of the crosslinked gels must be investigated and a method for removing surplus crosslinkers must be contrived. To increase the strength of the gels more than what was achieved in this project one could try to use longer crosslinkers, e.g. dodecamethylenediamine. Other possible methods that could be investigated is increasing the concentration of MFC, or decreasing the pH, thus protonating the carboxylate groups and decrease interfibril repulsion.

References

1. Stine Grihamar, I.H., Linn Engesvik, Eirik Winsnes, Andreas Fosse, *295 mister jobben - Södra Cell Tofte legges ned*, in *e24* Updated: 20.03.2013 14:37: <http://e24.no/naeringsliv/sodra-cell-tofte-legges-ned/20348489>.
2. *Nanoheal*. Updated: 2013-05-30.
3. Klemm, D., et al., *Nanocelluloses as Innovative Polymers in Research and Application*, in *Polysaccharides II*, D. Klemm, Editor. 2006, Springer Berlin Heidelberg. p. 49-96.
4. Alexandrescu, L., et al., *Cytotoxicity tests of cellulose nanofibril-based structures*. Cellulose, 2013: p. 1-11.
5. Klemm, D., et al., *Nanocelluloses: A New Family of Nature-Based Materials*. Angewandte Chemie International Edition, 2011. **50**(24): p. 5438-5466.
6. Saito, T., et al., *Homogeneous Suspensions of Individualized Microfibrils from TEMPO-Catalyzed Oxidation of Native Cellulose*. Biomacromolecules, 2006. **7**(6): p. 1687-1691.
7. Isogai, A., T. Saito, and H. Fukuzumi, *TEMPO-oxidized cellulose nanofibers*. Nanoscale, 2010. **3**(1): p. 71-85.
8. Brown, R.M., *Cellulose structure and biosynthesis: What is in store for the 21st century?* Journal of Polymer Science Part A: Polymer Chemistry, 2004. **42**(3): p. 487-495.
9. Siró, I. and D. Plackett, *Microfibrillated cellulose and new nanocomposite materials: a review*. Cellulose, 2010. **17**(3): p. 459-494.
10. Paakko, M., et al., *Enzymatic hydrolysis combined with mechanical shearing and high-pressure homogenization for nanoscale cellulose fibrils and strong gels*. Biomacromolecules, 2007. **8**(6): p. 1934-1941.
11. Christensen, B.E., *Compendium in TBT4135 Biopolymers*, 2011, NTNU: Trondheim, Norway.
12. Weinkamer, R. and P. Fratzl, *Mechanical adaptation of biological materials — The examples of bone and wood*. Materials Science and Engineering: C, 2011. **31**(6): p. 1164-1173.
13. Rånby, B., *Aqueous colloidal solutions of cellulose micelles*. Acta Chem Scand, 1949. **3**(5): p. 649-650.
14. Herrick, F.W., et al., *Microfibrillated cellulose: morphology and accessibility*. J. Appl. Polym. Sci. Appl. Polym. Symp., 1983. **37**: p. 797-813.
15. Turbak, A.F., F.W. Snyder, and K.R. Sandberg, *Microfibrillated cellulose, a new cellulose product: properties, uses, and commercial potential*. J. Appl. Polym. Sci. Appl. Polym. Symp., 1983. **37**: p. 815-827.
16. 27687:2008, I.T., *Nanotechnologies — Terminology and definitions for nano-objects — Nanoparticle, nanofibre and nanoplate*, 2008: <https://www.iso.org/obp/ui/#iso:std:iso:ts:27687:ed-1:v1:en:term:2.2>.
17. Chinga-Carrasco, G., *Cellulose fibres, nanofibrils and microfibrils: The morphological sequence of MFC components from a plant physiology and fibre technology point of view*. Nanoscale Research Letters, 2011. **6**(1): p. 417.
18. Eriksen, O., K. Syverud, and O. Gregersen, *The use of microfibrillated cellulose produced from kraft pulp as strength enhancer in TMP paper*. Nordic Pulp and Paper Research Journal, 2008. **23**(3): p. 299.

19. Iwamoto, S., A.N. Nakagaito, and H. Yano, *Nano-fibrillation of pulp fibers for the processing of transparent nanocomposites*. Applied Physics A, 2007. **89**(2): p. 461-466.
20. Saito, T., et al., *Cellulose Nanofibers Prepared by TEMPO-Mediated Oxidation of Native Cellulose*. Biomacromolecules, 2007. **8**(8): p. 2485-2491.
21. Okita, Y., T. Saito, and A. Isogai, *Entire Surface Oxidation of Various Cellulose Microfibrils by TEMPO-Mediated Oxidation*. Biomacromolecules, 2010. **11**(6): p. 1696-1700.
22. Saito, T. and A. Isogai, *Introduction of aldehyde groups on surfaces of native cellulose fibers by TEMPO-mediated oxidation*. Colloids and Surfaces A: Physicochemical and Engineering Aspects, 2006. **289**(1-3): p. 219-225.
23. Han, S., M. Lee, and B.K. Kim, *Crosslinking reactions of oxidized cellulose fiber. I. Reactions between dialdehyde cellulose and multifunctional amines on lyocell fabric*. Journal of Applied Polymer Science, 2010. **117**(2): p. 682-690.
24. Syverud, K., et al., *A comparative study of Eucalyptus and Pinus radiata pulp fibres as raw materials for production of cellulose nanofibrils*. Carbohydrate Polymers, 2011. **84**(3): p. 1033-1038.
25. Syverud, K., et al., *Cross-linking cellulose nanofibrils for potential elastic cryo-structured gels*. Nanoscale Research Letters, 2011. **6**(1): p. 626.
26. Hermanson, G.T., *Chapter 3 - Zero-Length Crosslinkers*, in *Bioconjugate Techniques (Second Edition)*. 2008, Academic Press: New York. p. 213-233.
27. Ruhaak, L.R., et al., *2-Picoline-borane: A non-toxic reducing agent for oligosaccharide labeling by reductive amination*. PROTEOMICS, 2010. **10**(12): p. 2330-2336.
28. Sato, S., et al., *One-pot reductive amination of aldehydes and ketones with α -picoline-borane in methanol, in water, and in neat conditions*. Tetrahedron, 2004. **60**(36): p. 7899-7906.
29. Hoffman, A.S., *Hydrogels for Biomedical Applications*. Annals of the New York Academy of Sciences, 2001. **944**(1): p. 62-73.
30. Seliktar, D., *Designing Cell-Compatible Hydrogels for Biomedical Applications*. Science, 2012. **336**(6085): p. 1124-1128.
31. Lee, K.Y. and D.J. Mooney, *Hydrogels for Tissue Engineering*. Chemical Reviews, 2001. **101**(7): p. 1869-1880.
32. Saha, K., et al., *Designing synthetic materials to control stem cell phenotype*. Current Opinion in Chemical Biology, 2007. **11**(4): p. 381-387.
33. Reilly, G.C. and A.J. Engler, *Intrinsic extracellular matrix properties regulate stem cell differentiation*. Journal of Biomechanics, 2010. **43**(1): p. 55-62.
34. Engler, A.J., et al., *Matrix Elasticity Directs Stem Cell Lineage Specification*. Cell, 2006. **126**(4): p. 677-689.
35. Huang, S. and D.E. Ingber, *Cell tension, matrix mechanics, and cancer development*. Cancer Cell, 2005. **8**(3): p. 175-176.
36. McClements, D.J., *Chapter Eight - Emulsion rheology*, in *Food Emulsions: Principles, Practices, and Techniques, Second Edition*. 2004, CRC Press.
37. Tschoegl, N.W., W. Knauss, and I. Emri, *Poisson's Ratio in Linear Viscoelasticity – A Critical Review*. Mechanics of Time-Dependent Materials, 2002. **6**(1): p. 3-51.
38. Draget, K.I., *Lecture slides in TFY 4525 Bipolymer Materials - Introduction to rheology*, 2012, NTNU: Trondheim, Norway.

39. Smidsrød, O.M., Størker T. , *Chapter 14 - Semi-dilute and concentrated solutions, polymer networks and gels, phase behaviour of polymer mixtures*, in *Biopolymer Chemistry*, L. Postmyr, Editor. 2008, Tapir Academic Press: Trondheim, Norway. p. 355-385.
40. Cox, W.P. and E.H. Merz, *Correlation of dynamic and steady flow viscosities*. Journal of Polymer Science, 1958. **28**(118): p. 619-622.
41. Goodwin, J.W.H., Roy W., *Chaper 6 - Nonlinear responses*, in *Rheology for Chemists - An Introduction, 2nd Edition*. 2008, The Royal Society of Chemistry (RSC Publishing): Cambridge UK. p. 198.
42. da Silva Perez, D., S. Montanari, and M.R. Vignon, *TEMPO-Mediated Oxidation of Cellulose III*. Biomacromolecules, 2003. **4**(5): p. 1417-1425.
43. Habibi, Y., H. Chanzy, and M. Vignon, *TEMPO-mediated surface oxidation of cellulose whiskers*. Cellulose, 2006. **13**(6): p. 679-687.
44. Chinga-Carrasco, G., *Optical methods for the quantification of the fibrillation degree of bleached MFC materials*. Micron, 2013. **48**(0): p. 42-48.
45. Hirn, U. and W. Bauer, *A review of image analysis based methods to evaluate fiber properties*. Lenzinger Berichte, 2006. **86**: p. 96-105.
46. Chinga, G., et al., *Quantification of the 3D microstructure of SC surfaces*. Journal of Microscopy, 2007. **227**(3): p. 254-265.
47. Wiora, G., *File:Laserprofilometer EN.svg*, 2006: Wikimedia Commons: <http://commons.wikimedia.org/>.
48. Binnig, G., et al., *Atomic resolution with atomic force microscope*. Surface Science, 1987. **189–190**(0): p. 1-6.
49. Binnig, G., C.F. Quate, and C. Gerber, *Atomic Force Microscope*. Physical Review Letters, 1986. **56**(9): p. 930-933.
50. Marti, O., B. Drake, and P.K. Hansma, *Atomic Force Microscopy of Liquid-Covered Surfaces - Atomic Resolution Images*. Applied Physics Letters, 1987. **51**(7): p. 484-486.
51. Chen, C.J., *Piezoelectric scanner*, in *Introduction to Scanning Tunneling Microscopy*. 1993, Oxford University Press, Inc.: New York, United States of America. p. 213-235.
52. Meyer, E., *Atomic force microscopy*. Progress in Surface Science, 1992. **41**(1): p. 3-49.
53. Meyer, G. and N.M. Amer, *Novel Optical Approach to Atomic Force Microscopy*. Applied Physics Letters, 1988. **53**(12): p. 1045-1047.
54. Zhong, Q., et al., *FRACTURED POLYMER SILICA FIBER SURFACE STUDIED BY TAPPING MODE ATOMIC-FORCE MICROSCOPY*. Surface Science, 1993. **290**(1-2): p. L688-L692.
55. Bede Pittenger, N.E., Chanmin Su, *Quantitative Mechanical Property Mapping at the Nanoscale with PeakForce QNM*. Application Note Veeco Instruments Inc., 2010: p. 1-12.
56. FEI, *An introduction to electron microscopy*, 2010, FEI: <http://www.fei.com/uploadedFiles/Documents/Content/Introduction to EM booklet July 10.pdf>.
57. Saha, N., et al., *Polymeric biomaterial based hydrogels for biomedical applications*. Journal of Biomaterials and nanobiotechnology, 2011. **2**(1): p. 85-90.
58. Saito, T., et al., *Self-aligned integration of native cellulose nanofibrils towards producing diverse bulk materials*. Soft Matter, 2011. **7**(19): p. 8804-8809.

59. Chronakis, I.S. and P. Alexandridis, *Rheological properties of oppositely charged polyelectrolyte-surfactant mixtures: Effect of polymer molecular weight and surfactant architecture*. *Macromolecules*, 2001. **34**(14): p. 5005-5018.
60. *Wolfram Alpha - Computational knowledge engine*, 2013, Wolfram Alpha LLC: <http://www.wolframalpha.com/>.
61. Bartos, J. and M. Pesez, *Colorimetric and fluorimetric determination of aldehydes and ketones*. *Pure Appl Chem*, 1979. **51**: p. 1803-1814.
62. Nelson, P., *Chapter 4 - Random walks, friction and diffusion*, in *Biological Physics - Energy, Information, Life*. 2008, W.H. Freeman and Company: New York, NY, United States of America. p. 108-122.
63. Kennedy, G.L., *Toxicity of Hexamethylenediamine (HMDA)*. *Drug and Chemical Toxicology*, 2005. **28**(1): p. 15-33.

List of Appendices

Appendix A: Conductometric titration	- 1 -
A1: Procedure for calculating carboxylate and aldehyde concentration and DO	- 1 -
A2: Individual results from each replicate	- 3 -
Appendix B: Dynamic measurements	- 4 -
Appendix C: Longitudinal deformation	- 7 -
C1: Behavior during deformation	- 7 -
C2: Numerical values for Young's moduli	- 10 -
Appendix D: SEM images of freeze-dried gels	- 13 -
Appendix E: Representative laser profilometry images	- 20 -
Appendix F: Representative atomic force microscopy images	- 23 -
Appendix G: Numerical water absorption values	- 27 -

Appendix A: Conductometric titration

A1: Procedure for calculating carboxylate and aldehyde concentration and DO

The measured conductivity was plotted as a function of volume of added NaOH using Microsoft Excel 2010. The Tiamo® Titration Software calculated the gradient of the change in conductivity, and the data points for which the gradient was approximately constant (negative, zero and positive) were used for linear regression. The two intercepts for the linear regression expressions were calculated, and the difference between the intercepts yielded the added volume of sodium hydroxide where the conductivity was approximately constant, V_{OH} .

The amount of charged groups per unit mass, n_q , is usually given in mmol/g unit mass. The concentration of the added base, C_{OH} , is known. Using a strong base of monovalent constituents, such as sodium hydroxide, each molar unit of added base yields an equal amount of hydroxide ions. Assuming that each hydroxide ion neutralizes one proton from the carboxylate groups, V_{OH} yields the relative molar amount of carboxylate groups, n_a . Knowing the total mass of cellulose in the sample, w , n_q can be calculated by Equation A.1:

$$n_q = \frac{n_a}{w} = \frac{C_{OH}V_{OH}}{w} \quad (\text{A.1}).$$

Degree of oxidation, DO , is the number of subunits where the C6 hydroxy groups have been oxidized into carboxylate groups, n_a , divided by the total number of subunits, as defined by Equation A.2:

$$DO \equiv \frac{n_a}{n_a + n_g} \quad (\text{A.2}),$$

where n_g is the number of non-oxidized anhydroglucose subunits. Assuming that the total mass of cellulose, w , only is comprised of oxidized carboxylate or non-oxidized anhydroglucose subunits, n_g can be calculated by Equation A.3,

$$n_g = \frac{w - n_a M_a}{M_g} \quad (\text{A.3}),$$

where M_a and M_g are the molecular weights of the two subunits. n_a is known as $C_{OH}V_{OH}$ from Equation A.1. Inserting n_g and n_a into Equation A.2 yields

$$DO = \frac{C_{OH}V_{OH}M_g}{w - C_{OH}V_{OH}(M_a - M_g)} \quad (A.4).$$

Equation 2.3.4 is also described by Da Silva Perez et al. and Habibi et al [42, 43]. M_g is given as 162 g/mol, while $(M_a - M_g)$ is given as 36 g/mol, which according to Habibi et al. corresponds to the difference in molecular weight between an anhydroglucose unit and the sodium salt of a glucuronic acid moiety [43]. More precisely, since the molecular formula of cellulose is $(C_6H_{10}O_5)_n$, M_g becomes 162.141 g/mol. The molecular formula of polyglucuronic acid is $(C_6H_7O_6^-)_n$, yielding a value of 175.116 g/mol for one glucuronic acid moiety, and 198.106 g/mol for its sodium salt. Using the sodium salt as the value for M_a yields a $(M_a - M_g)$ value of 35.965 g/mol.

The average carboxylate content and DO with standard deviations (SD) were calculated for the two parallels. The first parallel contained two replicates, while the second contained three replicates. Assuming all aldehyde groups had been oxidized to carboxylate by sodium chlorite, the aldehyde content and DO was calculated by subtracting the average carboxylate content in the regular MFC from the average carboxylate content in the sodium chlorite oxidized MFC. Due to propagation of errors, the standard deviation of the aldehyde content, SD_a , become much larger than the standard deviations of the carboxylate averages. SD_a was hence calculated by Equation (A.5):

$$SD_a = \sqrt{SD_{c1}^2 + SD_{c2}^2} \quad (A.5),$$

where SD_{c1} and SD_{c2} are the standard deviations of the average carboxylate content of the regular MFC and the sodium chlorite oxidized MFC, respectively.

A2: Individual results from each replicate

Table A.1: Linear regression expressions for the decreasing, constant and increasing regions, as well as the two intercepts between these, of each conductometric titration replicate from the first parallel.

First Parallel	Decreasing	Constant	Increasing	IC1	IC2
MFC oxidized with sodium chlorite, before centrifugation					
1. replicate	$y = -0.0499x + 0.6226$	$y = 0.0092x + 0.2349$	$y = 0.0295x - 0.1247$	6.56	17.71
2. replicate	$y = -0.0500x + 0.6183$	$y = 0.0093x + 0.2339$	$y = 0.0295x - 0.1166$	6.48	17.35
3. replicate	$y = -0.0493x + 0.6030$	$y = 0.0093x + 0.2292$	$y = 0.0295x - 0.1212$	6.38	17.35
MFC oxidized with sodium chlorite, after centrifugation					
1. replicate	$y = -0.0534x + 0.6134$	$y = 0.0036x + 0.2207$	$y = 0.0296x - 0.0315$	6.89	9.70
2. replicate	$y = -0.0532x + 0.6002$	$y = 0.0019x + 0.2314$	$y = 0.0296x - 0.0300$	6.69	9.44
MFC					
1. replicate	$y = -0.0533x + 0.6223$	$y = 0.0018x + 0.2661$	$y = 0.0320x + 0.0035$	6.46	8.70
2. replicate	$y = -0.0510x + 0.6988$	$y = 0.0021x + 0.2839$	$y = 0.0302x - 0.0036$	7.81	10.23

Table A.2: Calculated carboxylate and aldehyde concentrations as well as degree of oxidation (DO) for each conductometric titration replicate from the first parallel.

First parallel	1. replicate	2. replicate	3. replicate
MFC oxidized with sodium chlorite, before centrifugation			
Carboxylate groups [mmol/g MFC]	4.318	4.348	4.387
Degree of oxidation, DO	82.9 %	83.6 %	84.5 %
MFC oxidized with sodium chlorite, after centrifugation			
Carboxylate groups [mmol/g MFC]	1.124	1.088	n/a
Degree of oxidation, DO	19.0 %	18.4 %	n/a
MFC			
Carboxylate groups [mmol/g MFC]	0.9067	0.9668	n/a
Degree of oxidation, DO	15.2 %	16.2 %	n/a

Table A.3: Linear regression expressions for the decreasing, constant and increasing regions, as well as the two intercepts between these, of each conductometric titration replicate from the second parallel.

Second Parallel	Decreasing	Constant	Increasing	IC1	IC2
MFC oxidized with sodium chlorite					
1. replicate	$y = -0.0523x + 0.4986$	$y = 0.0026x + 0.2028$	$y = 0.0326x - 0.0307$	5.39	7.78
2. replicate	$y = -0.0533x + 0.5643$	$y = 0.0027x + 0.2157$	$y = 0.0326x - 0.0452$	6.23	8.73
3. replicate	$y = -0.0541x + 0.5474$	$y = 0.0024x + 0.2138$	$y = 0.0325x - 0.0405$	5.90	8.45
MFC					
1. replicate	$y = -0.0533x + 0.6121$	$y = -0.0004x + 0.2800$	$y = 0.0319x + 0.0113$	6.28	8.32
2. replicate	$y = -0.0533x + 0.6007$	$y = 0.0002x + 0.2731$	$y = 0.0319x + 0.0173$	6.12	8.07
3. replicate	$y = -0.0539x + 0.6788$	$y = -0.0003x + 0.2979$	$y = 0.0313x + 0.0071$	7.11	9.20

Table A.4: Calculated carboxylate and aldehyde concentrations as well as degree of oxidation (DO) for each conductometric titration replicate from the second parallel.

Second parallel	1. replicate	2. replicate	3. replicate
MFC oxidized with sodium chlorite			
Carboxylate groups [mmol/g MFC]	0.959	0.999	1.016
Degree of oxidation, DO	16.1 %	16.8 %	17.1 %
MFC			
Carboxylate groups [mmol/g MFC]	0.815	0.778	0.838
Degree of oxidation, DO	13.6 %	13.0 %	14.0 %

Appendix B: Dynamic measurements

Figure B.1 show the power law regression of the average storage moduli from within the VLR, given in Section 3.3.1, as a function of MFC concentration. Figures B.2 – B.4 show the investigation of the viscoelastic properties of two replicates of 0.80% MFC with 3.05 mmol HMDA/g MFC, performed by subsequently running a temperature sweep (to induce crosslinking), frequency sweep, and amplitude sweep on each of the replicates.

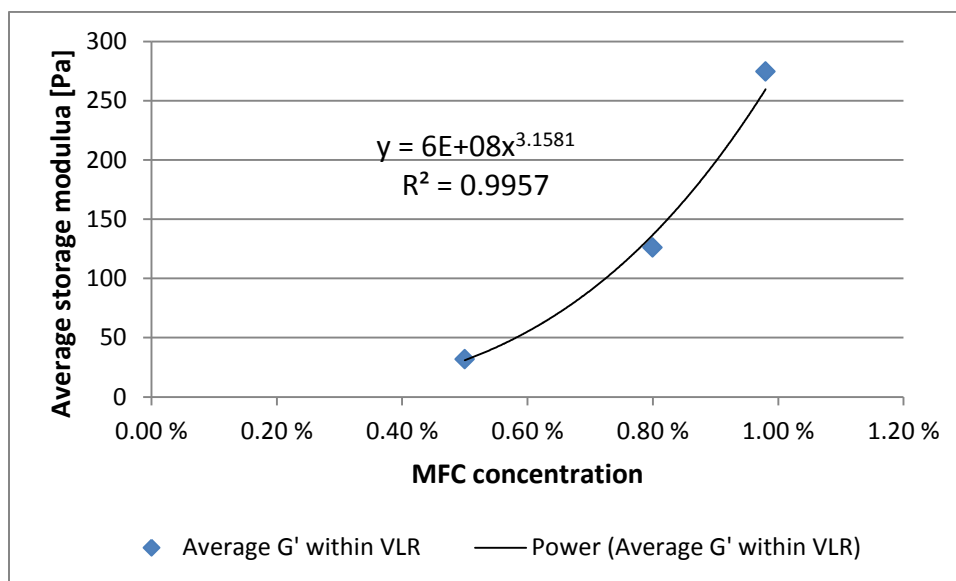


Figure B.1: Power law regression of the average storage modulus from within the VLR as a function of MFC concentration.

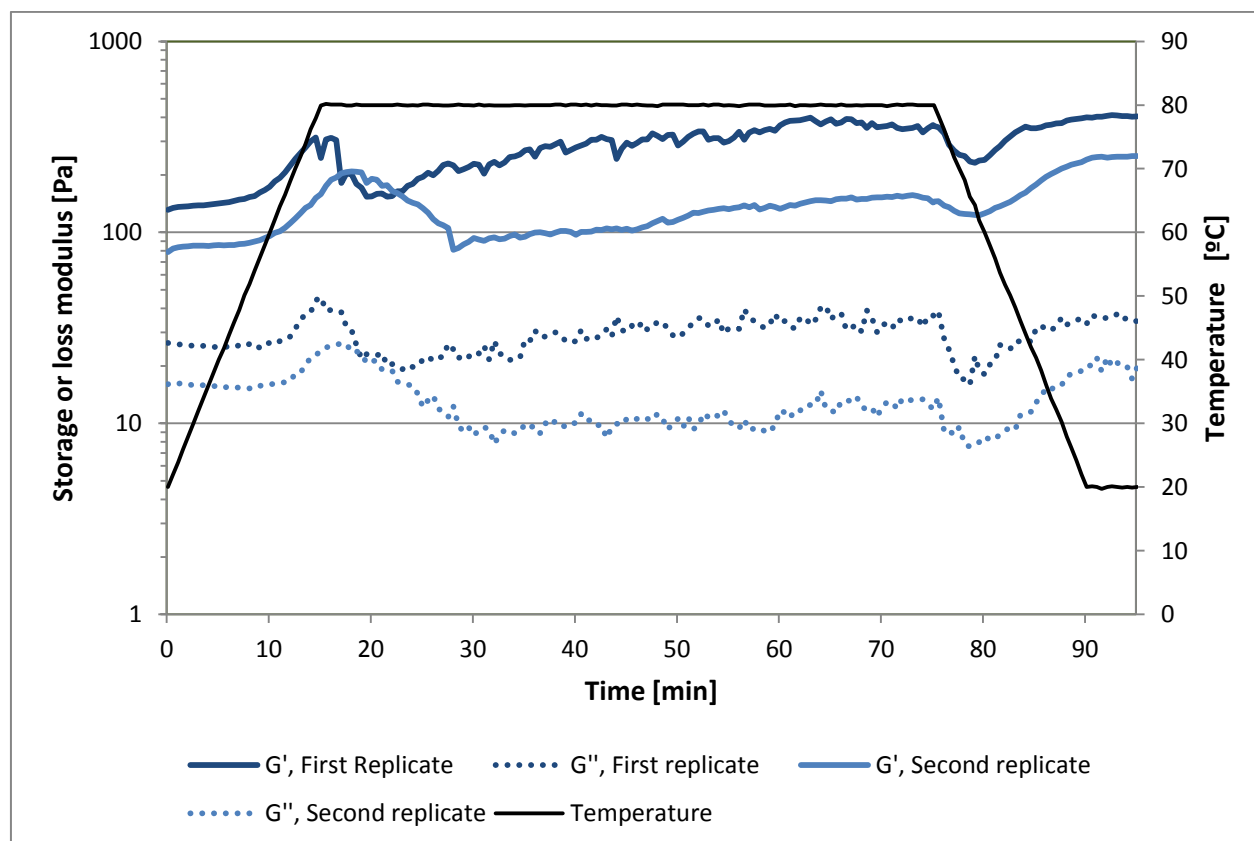


Figure B.2: Temperature sweeps, 20 – 80 – 20 °C (± 4 °C/min), constant 80° C for one hour, measured on two replicates of 0.80% MFC with HMDA (3.05 mmol/g MFC). The frequency and strain was held constant at 1 Hz and 0.01, respectively. Notice the breaks hindering the storage modulus from reaching the plateau values observed in Figure 3.3.5.

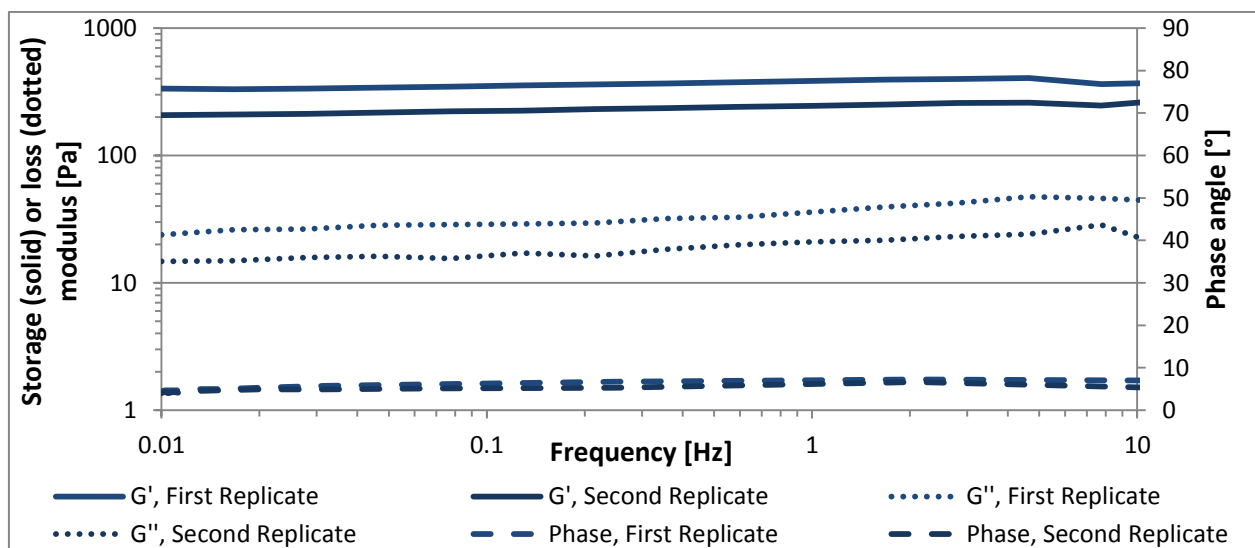


Figure B.3: Frequency sweeps measured on two replicates of 0.80% MFC with HMDA (3.05 mmol/g MFC). The temperature and strain was held constant at 20° C and 0.01, respectively. Both replicates showed gel-like behavior for the whole frequency range (i.e. $G' > G''$, δ constant).

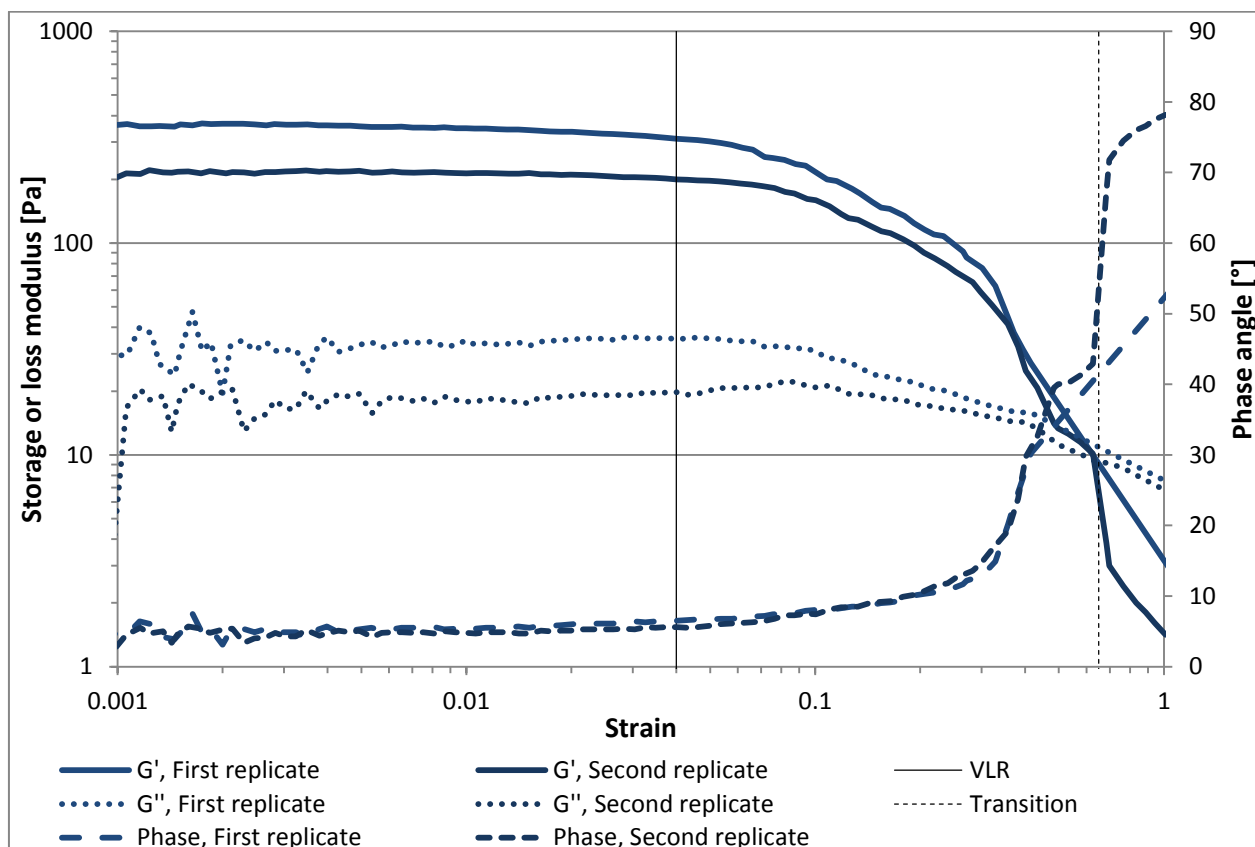


Figure B.4: Amplitude sweep measured on two replicates of 0.80% MFC with HMDA (3.05 mmol/g MFC). The temperature and frequency was held constant at 20° C and 1Hz, respectively. The storage and loss moduli were approximately constant (i.e. yielding the VLR) for strains ≤ 0.04 . The stippled line shows the transition from primarily gel-like behavior to viscous behavior.

Appendix C: Longitudinal deformation

C1: Behavior during deformation

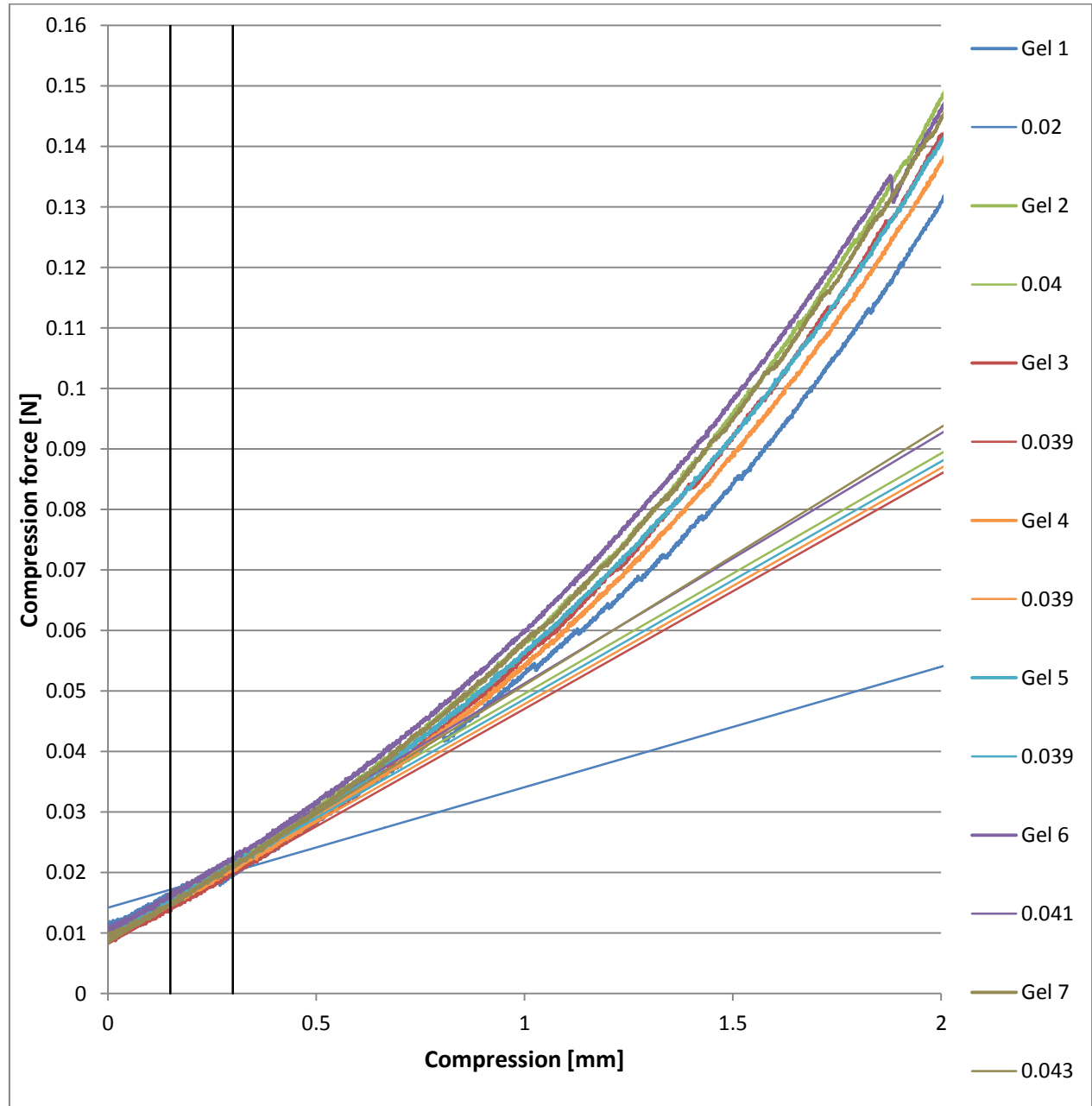


Figure C.1: Force-compression curves for two gels with HMDA (3.05 mmol/g MFC) obtained by longitudinal compression with a texture analyzer. The numbers in the legend are the gradients of the linear regression lines for the individual curves, which were obtained for compression between 0.15 – 0.30 mm. The curves were recorded after an initial trigger force of 1 g was reached. The gels only showed ideal (i.e. linear) elastic behavior for very small strains (<0.5 mm). The smaller gradient of the dark blue curve was due to a small break in the linear zone, not visible in this plot.



Figure C.2: Longitudinal compression (8 mm compression after a trigger force of 1 g was reached) of one gel with HMDA (3.05 mmol/g MFC). The compression is recorded in one of the curves in Figure C.4.

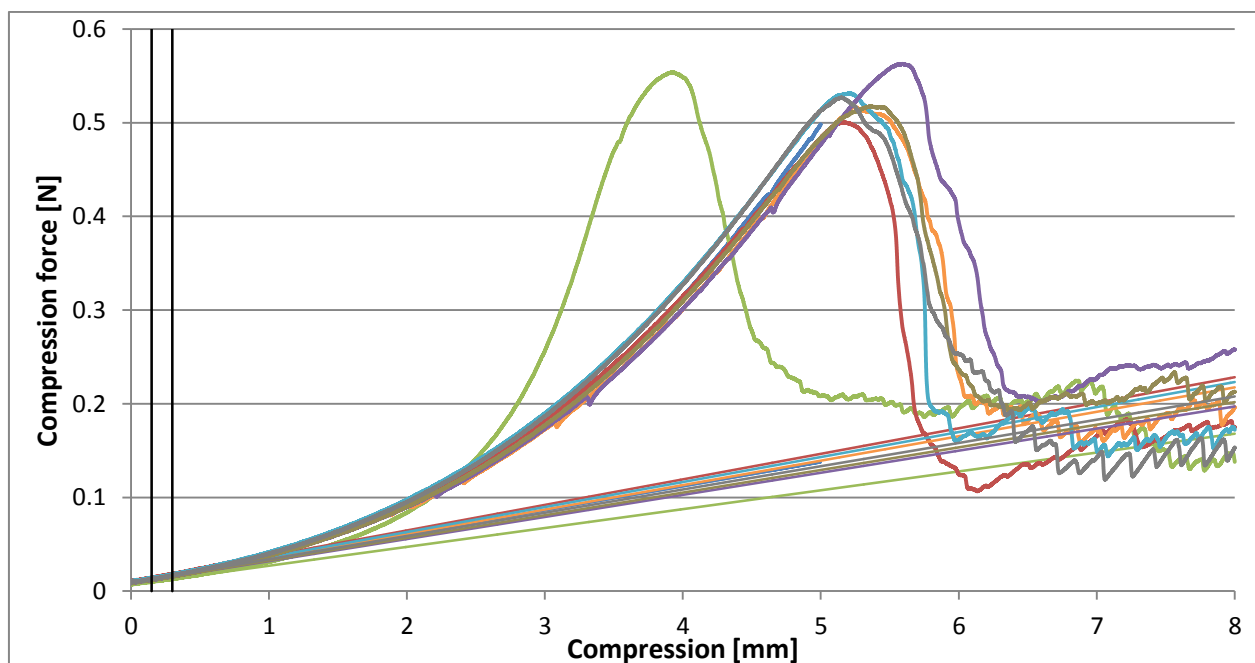


Figure C.3: Force-compression curves for gels with EDA (3.04 mmol/g MFC), with linear regression lines derived from 0.15 – 0.30 mm compression. Note the one curve with a much steeper gradient (light green). This gel was first compressed 5 mm without breaking, and the compression was thereafter increased to 8 mm and measured on the same gel. The lower gradient and shorter compression length at break suggests that this decreased the elasticity of the gel. The force at break did not seem to be affected.

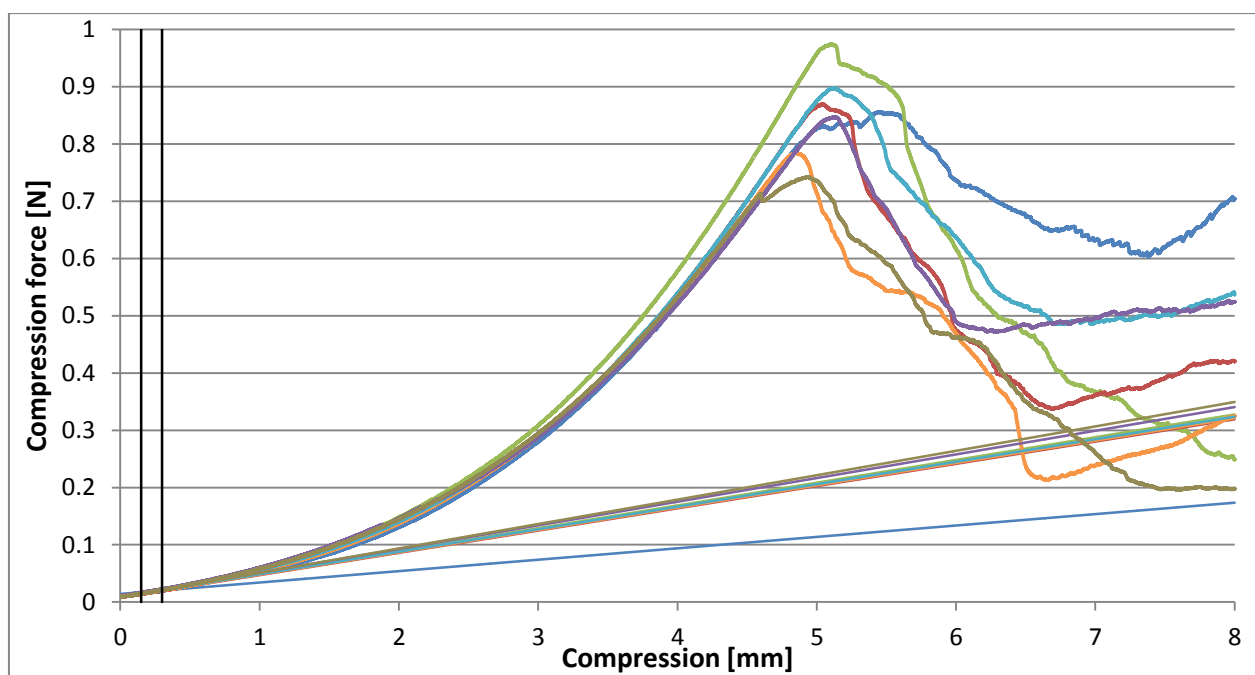


Figure C.4: Force-compression curves for gels with HMDA (3.05 mmol/g MFC), with linear regression lines derived from 0.15 – 0.30 mm compression. The initial 2 mm compression can be seen in Figure C.1.

C2: Numerical values for Young's moduli

The gradient [N/mm → N/m] was obtained separately for each gel using linear regression on the data points between 15 – 30 mm of the force vs. compression curves. The contact area A between the gel and the probe was calculated using the equation for the area of a circle;

$$A = \pi \left(\frac{d}{2} \right)^2 \quad (\text{C.1}),$$

where d is the measured diameter of the gels. Young's modulus E [kPa = kN/m²] was calculated separately for each gel using the equation:

$$E = \frac{F}{\Delta l} \times \frac{l}{A} \quad (\text{C.2}),$$

where $(F/\Delta l)$ is the gradient, and l is the measured initial height of the gels. The average Young's moduli and standard deviations were subsequently calculated for each concentration parallel.

Table C.1: Sample codes, crosslinker concentration for each sample, amine:aldehyde ratio (based on second conductometric titration parallel; aldehyde concentration: 0.181 mmol/g MFC) and total time in heating cabinet for the cast gels with 0.80% MFC.

Sample code	Amount crosslinker [mmol/g MFC]	Ratio amine:aldehyde [mol:mol]	Total time in heating cabinet at 80°C
H1	6.08E-02	0.67	16:40:00
H2.5	1.52E-01	1.68	19:50:00
H5	3.04E-01	3.36	19:50:00
H10	6.12E-01	6.76	17:55:00
H50	3.05E+00	33.65	18:40:00
H100	6.09E+00	67.31	16:40:00
H1 + 2picbor	6.08E-02	0.67	17:55:00
H2.5 + 2picbor	1.52E-01	1.68	19:50:00
H5 + 2picbor	3.04E-01	3.36	20:30:00
H10 + 2picbor	6.12E-01	6.76	17:55:00
H50 + 2picbor	3.05E+00	33.65	18:40:00
H100 + 2picbor	6.09E+00	67.31	16:40:00
E1	6.14E-02	0.68	16:50:00
E2.5	1.52E-01	1.67	20:30:00
E5	3.04E-01	3.36	16:50:00
E10	6.09E-01	6.73	20:30:00
E50	3.04E+00	33.61	16:50:00
E100	6.08E+00	67.22	18:20:00
H50 Longer Compression	3.05E+00	33.65	18:20:00
E50 Longer Compression	3.04E+00	33.61	18:20:00

Table C.2: Average, standard deviation (SD), and coefficient of variation (CV) values for the gradients of 15 – 30 mm compression of the force vs. compression curves of the gels cast with 0.80% MFC and varying crosslinker concentration, as well as the time-lapsed gels. Some gels were omitted from the average values due to damages or air bubbles in the gels affecting the gradients. The same number of gels applies for Table C.3 and C.4.

Sample code	Gradient of linear area [N/m]			Number of gels
	Average	SD	CV	
H1	22.29	2.29	10 %	7
H2.5	28.29	1.89	7 %	7
H5	34.71	1.98	6 %	7
H10	35.43	1.27	4 %	7
H50	41.00	2.45	6 %	5
H100	40.29	2.21	5 %	7
H1 + 2picbor	18.17	0.75	4 %	6
H2.5 + 2picbor	24.57	2.07	8 %	7
H5 + 2picbor	30.86	2.41	8 %	7
H10 + 2picbor	39.43	1.72	4 %	7
H50 + 2picbor	38.71	1.38	4 %	7
H100 + 2picbor	36.86	0.90	2 %	7
E1	22.86	1.57	7 %	7
E2.5	23.43	1.62	7 %	7
E5	23.14	0.69	3 %	7
E10	24.43	1.62	7 %	7
E50	25.14	1.68	7 %	7
E100	26.00	1.10	4 %	6
H50 Longer Compression	40.17	1.60	4 %	6
E50 Longer Compression	25.57	1.27	5 %	7
H50_1h	20.20	1.48	7 %	5
H50_3h	24.20	1.92	8 %	5
H50_5h	28.40	1.14	4 %	5
H50_8h	32.00	2.35	7 %	5
H50_24h	44.50	1.29	3 %	4

Table C.3: Average (AVG), standard deviation (SD), and coefficient of variation (CV) values for the height and diameters (measured with digital caliper), and calculated Young's moduli of the gels cast with 0.80% MFC and varying crosslinker concentration.

Sample code	Measured height [mm]			Measured diameter [mm]			Young's Modulus, E [kPa]		
	AVG	SD	CV	AVG	SD	CV	AVG	SD	CV
H1	14.55	0.37	3 %	18.56	0.17	1 %	1.195	0.097	8 %
H2.5	16.61	0.29	2 %	17.51	0.20	1 %	1.950	0.118	6 %
H5	16.90	0.09	1 %	16.96	0.17	1 %	2.599	0.184	7 %
H10	17.15	0.25	1 %	16.73	0.16	1 %	2.765	0.120	4 %
H50	17.81	0.33	2 %	17.00	0.00	0 %	3.218	0.219	7 %
H100	16.95	0.40	2 %	16.54	0.29	2 %	3.178	0.186	6 %
H1 + 2picbor	14.47	0.37	3 %	18.31	0.33	2 %	1.001	0.073	7 %
H2.5 + 2picbor	15.69	0.27	2 %	17.64	0.24	1 %	1.577	0.141	9 %
H5 + 2picbor	17.11	0.14	1 %	16.83	0.09	1 %	2.372	0.187	8 %
H10 + 2picbor	17.64	0.19	1 %	16.94	0.12	1 %	3.087	0.137	4 %
H50 + 2picbor	16.90	0.37	2 %	17.00	0.00	0 %	2.883	0.121	4 %
H100 + 2picbor	16.56	0.21	1 %	16.52	0.14	1 %	2.847	0.089	3 %
E1	14.08	0.46	3 %	17.86	0.28	2 %	1.284	0.093	7 %
E2.5	15.36	0.48	3 %	17.32	0.09	1 %	1.527	0.098	6 %
E5	15.43	0.17	1 %	17.16	0.11	1 %	1.544	0.060	4 %
E10	16.31	0.21	1 %	17.05	0.18	1 %	1.745	0.135	8 %
E50	16.03	0.17	1 %	16.99	0.08	0 %	1.779	0.127	7 %
E100	16.69	0.17	1 %	16.97	0.08	0 %	1.918	0.092	5 %
H50 Longer Compression	17.42	0.39	2 %	16.62	0.16	1 %	3.228	0.154	5 %
E50 Longer Compression	16.35	0.20	1 %	17.06	0.06	0 %	1.829	0.100	5 %

Table C.4: Average (AVG), standard deviation (SD), and coefficient of variation (CV) values for the height and diameters (measured with digital caliper), and calculated Young's moduli of the gels cast with 0.80% MFC and 3.05 mmol HMDA/g MFC, taken out after different times in the heating cabinet.

Sample code	Time at 80°C	Measured height [mm]			Measured diameter [mm]			Young's Modulus, E [kPa]		
		AVG	SD	CV	AVG	SD	CV	AVG	SD	CV
H50_1h	01:05:00	15.19	0.15	1 %	16.39	0.45	3 %	1.453	0.088	6 %
H50_3h	03:05:00	16.60	0.48	3 %	16.96	0.09	1 %	1.780	0.176	10 %
H50_5h	05:10:00	16.85	0.21	1 %	17.00	0.12	1 %	2.107	0.079	4 %
H50_8h	08:20:00	16.57	0.87	5 %	16.92	0.19	1 %	2.353	0.071	3 %
H50_24h	23:40:00	16.93	0.20	1 %	16.71	0.05	0 %	3.436	0.143	4 %

Appendix D: SEM images of freeze-dried gels

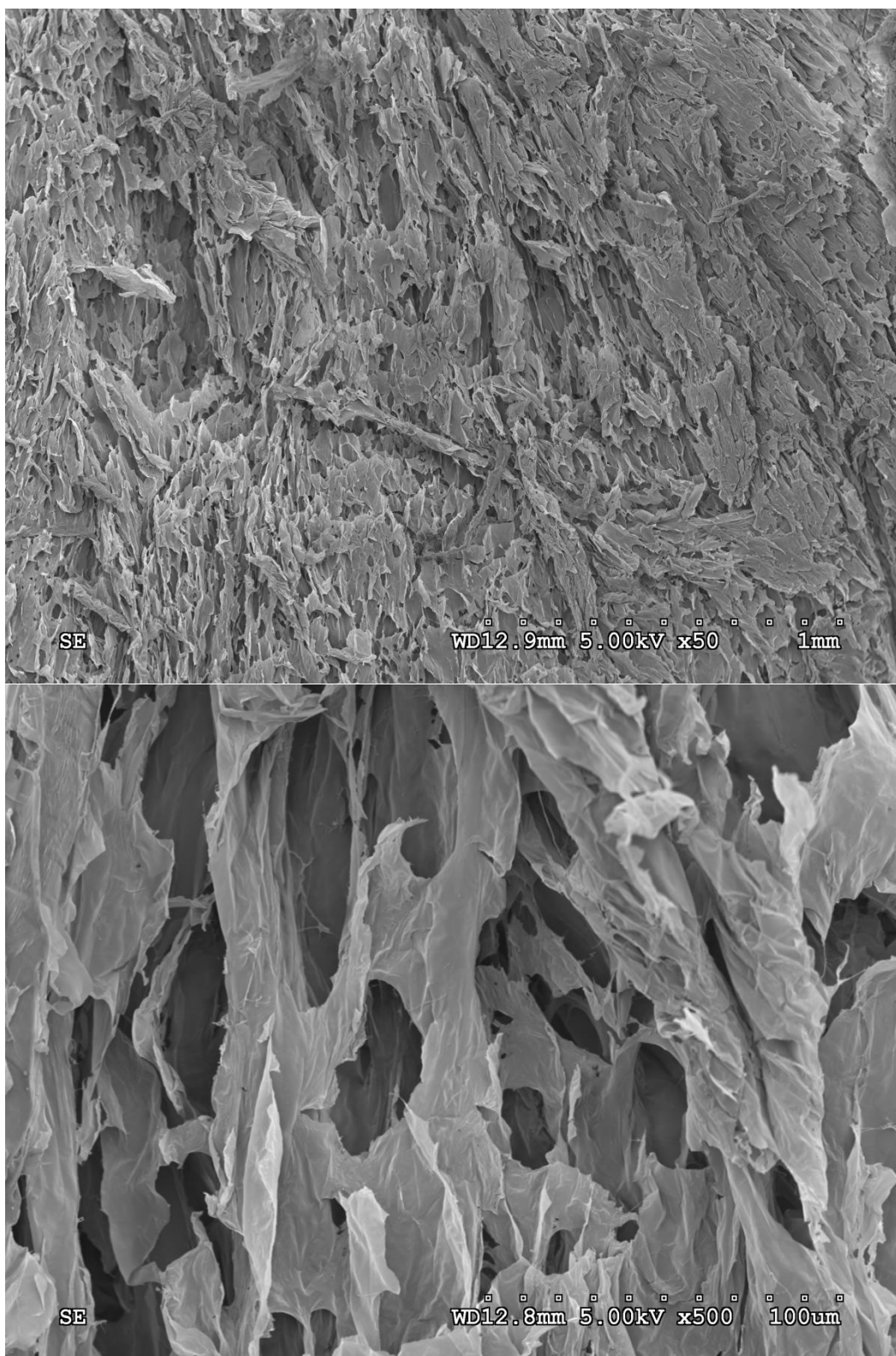


Figure D.1: Cross-section of a freeze-dried MFC gel without crosslinkers.

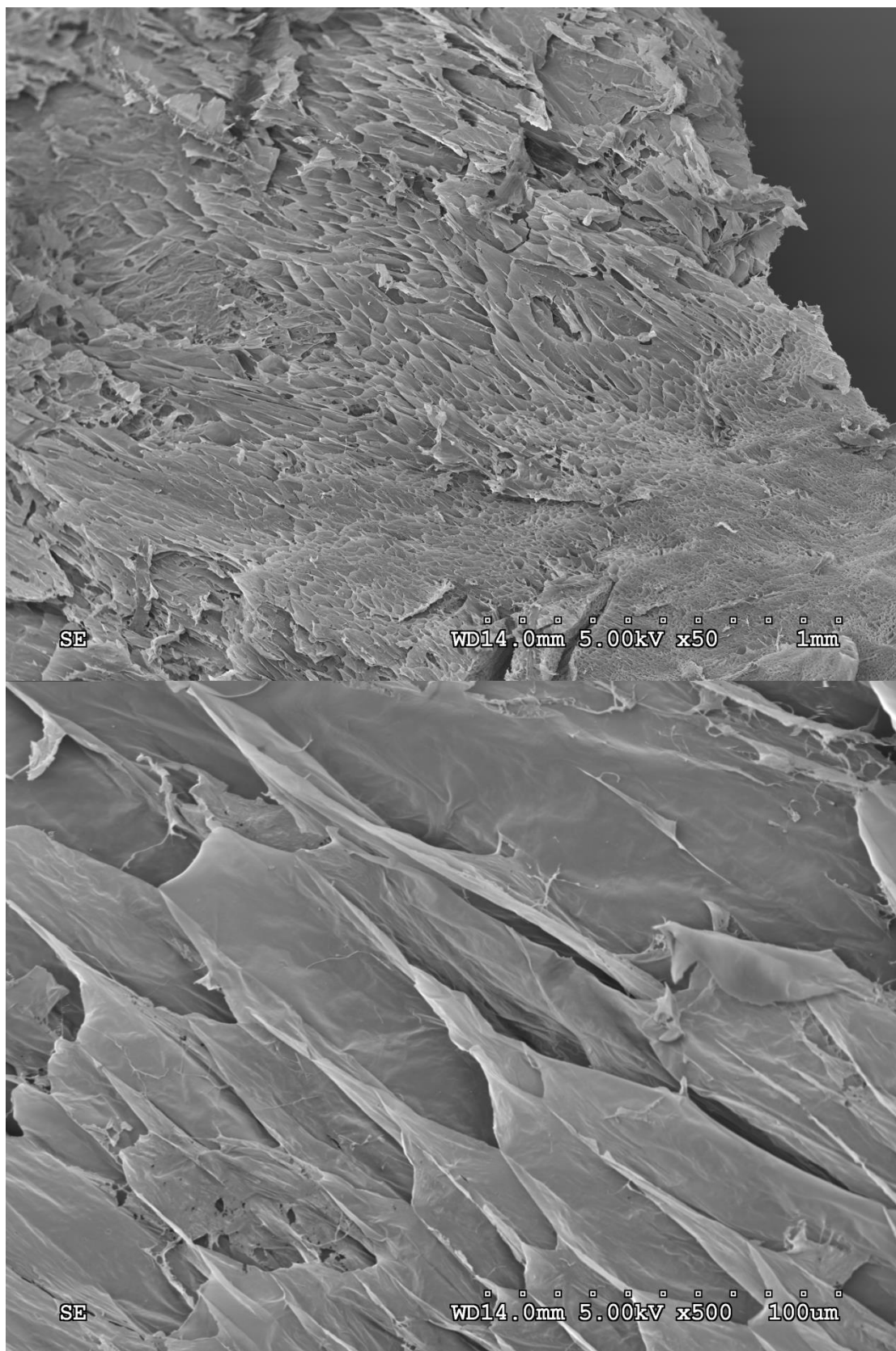


Figure D.2: Cross-section of a freeze-dried gel with 6.14×10^{-2} mmol EDA/g MFC.

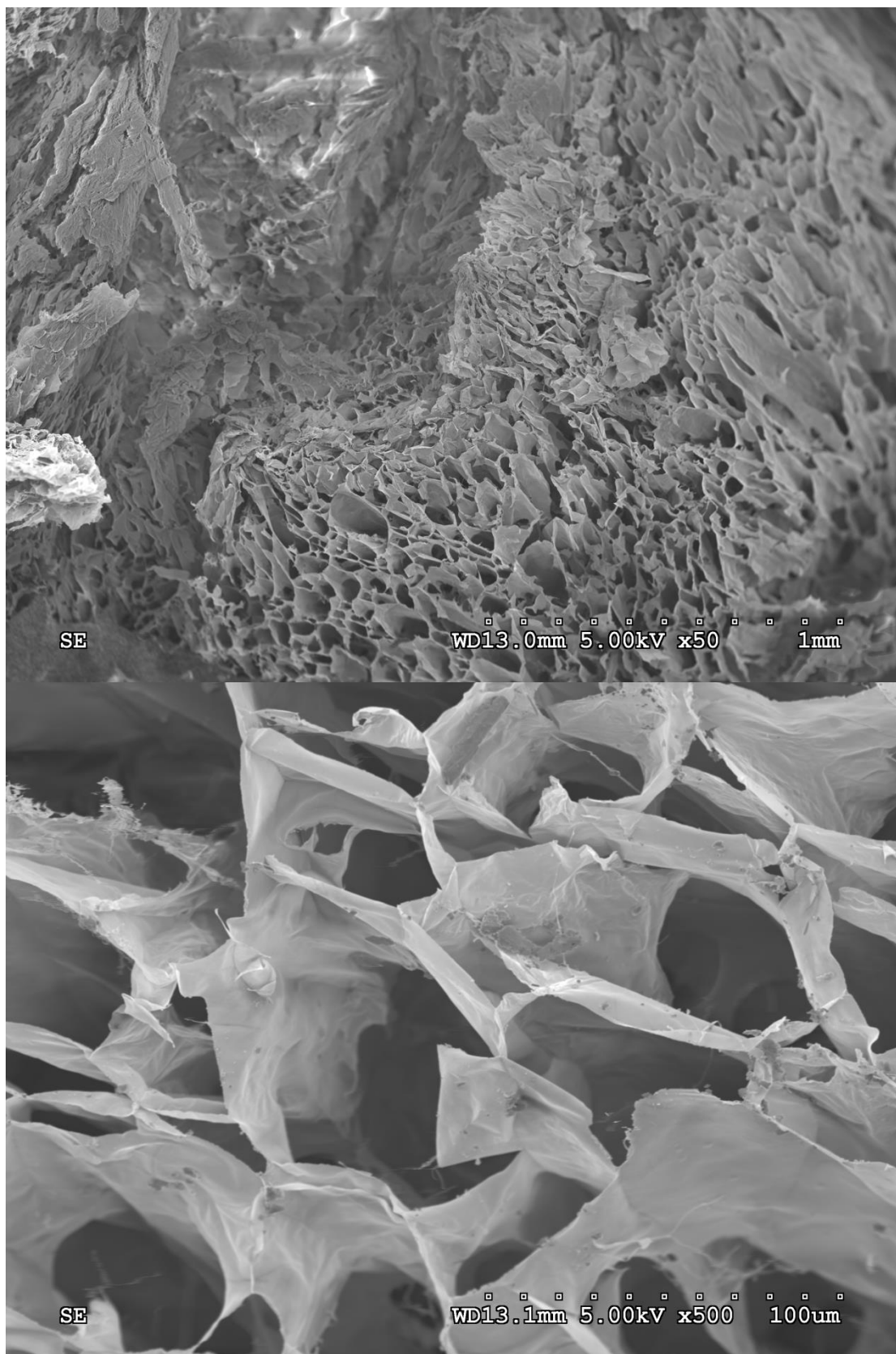


Figure D.3: Cross-section of a freeze-dried gel with 6.08×10^{-2} mmol HMDA/g MFC.

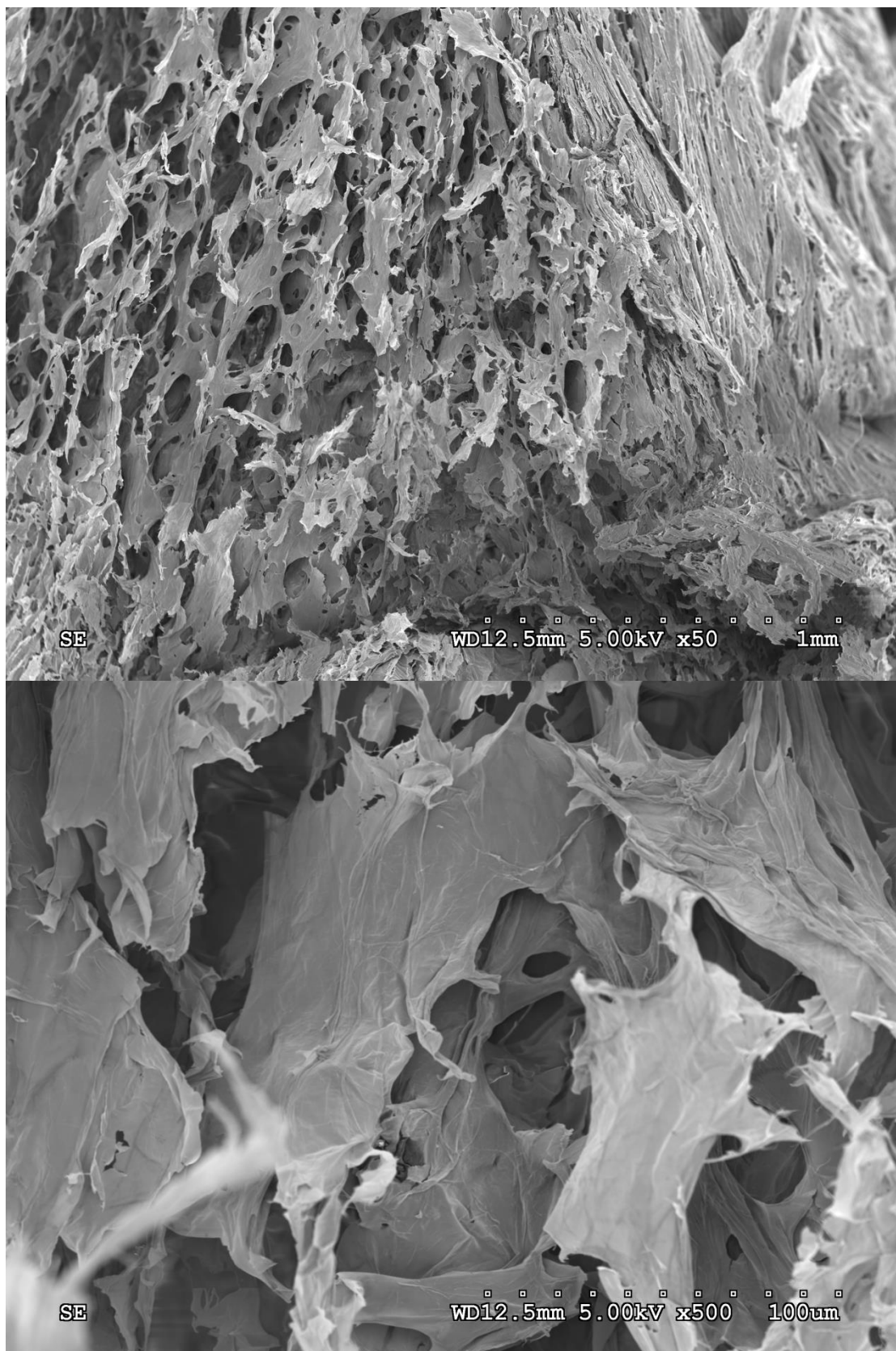


Figure D.4: Cross-section of a freeze-dried gel with 3.04 mmol EDA/g MFC.

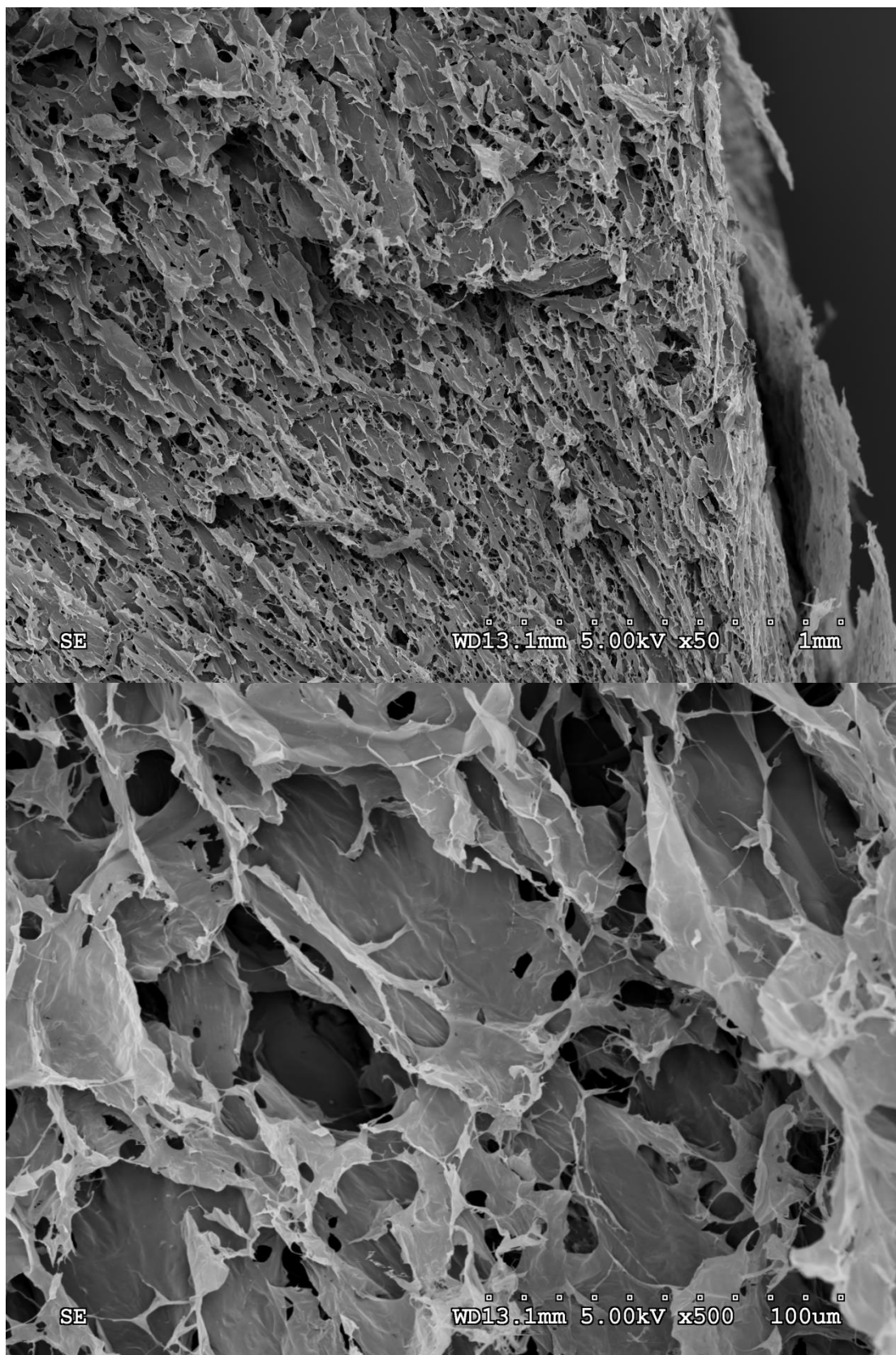


Figure D.5: Cross-section of a freeze-dried gel with 3.05 mmol HMDA/g MFC.

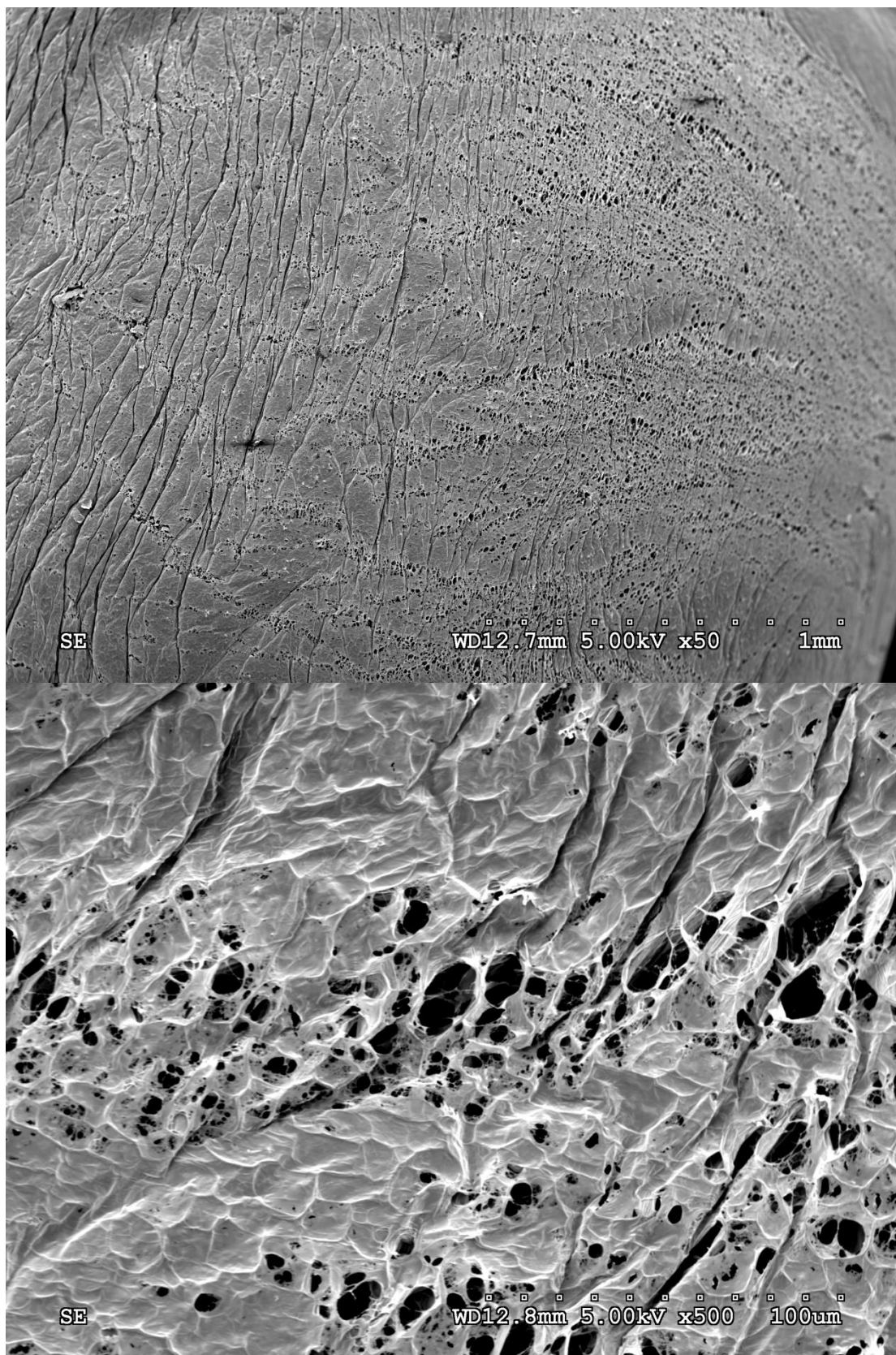


Figure D.6: Surface of a freeze-dried gel with 6.14×10^{-2} mmol EDA/g MFC.

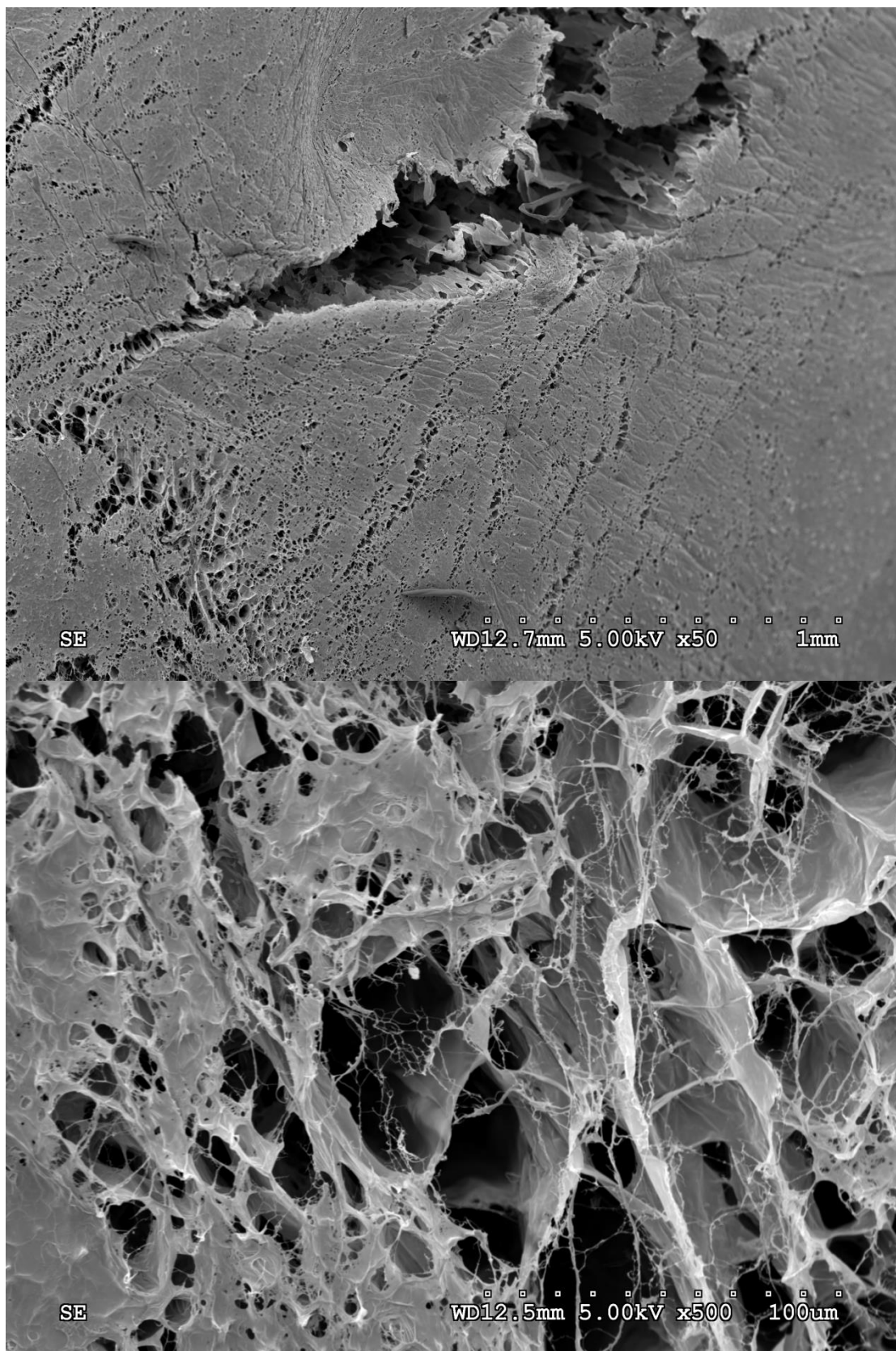


Figure D.7: Surface of a freeze-dried gel with 6.08×10^{-2} mmol HMDA/g MFC.

Appendix E: Representative laser profilometry images

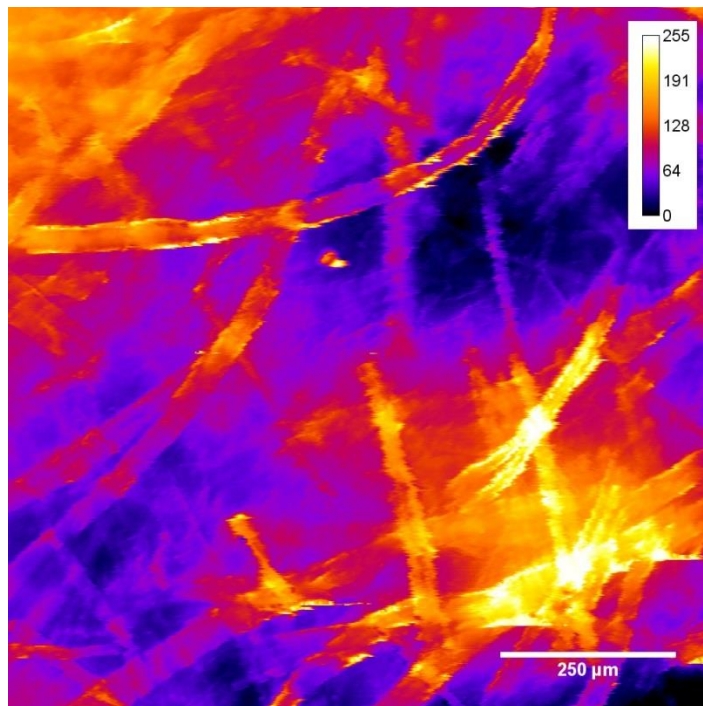


Figure E.1: Representative (Sq-value closet to average) topographic image (1 mm × 1mm) of the surface of a film of dried MFC with no crosslinkers, captured by laser profilometer.

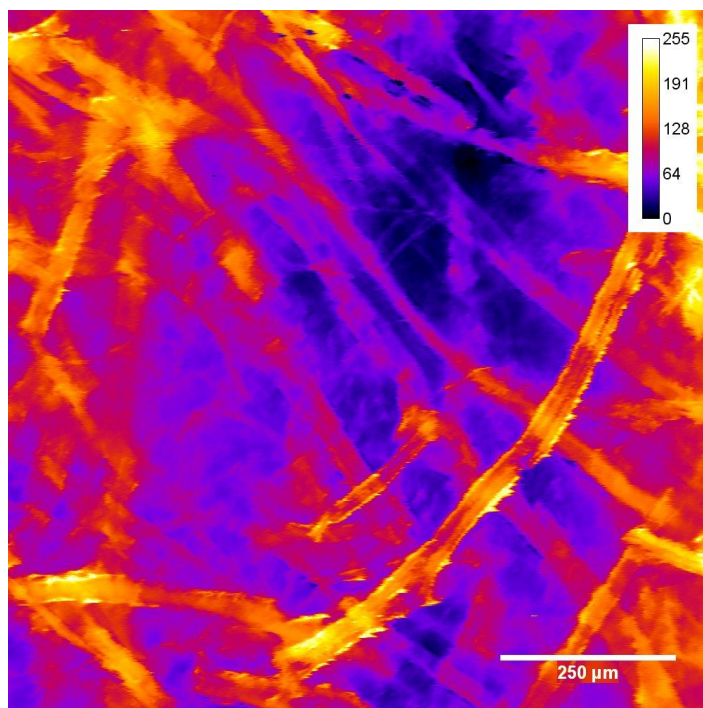


Figure E.2: Representative (Sq-value closet to average) topographic image (1 mm × 1mm) of the surface of a film of dried MFC with 3.04×10⁻¹ mmol HMDA/g MFC, captured by laser profilometer.

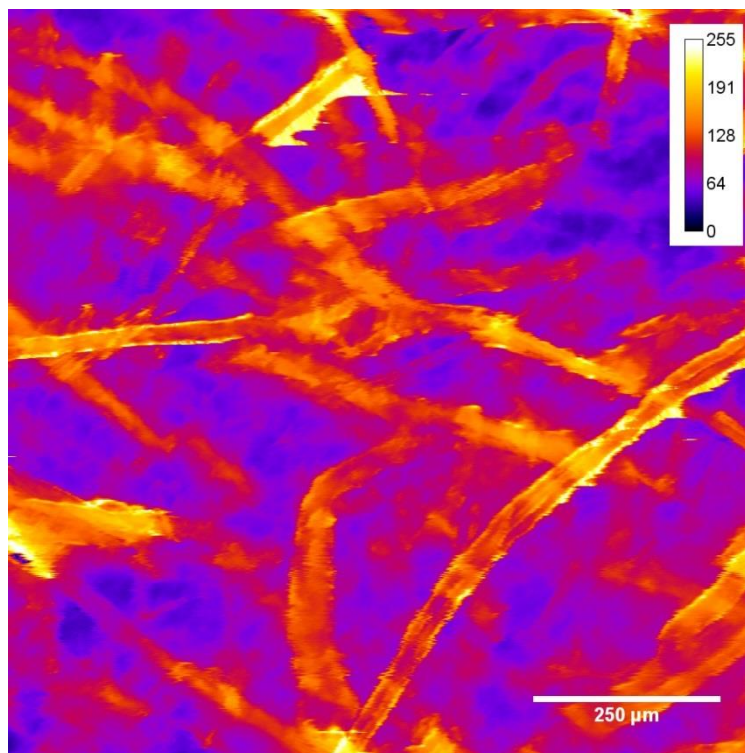


Figure E.3: Representative (Sq-value closet to average) topographic image (1 mm × 1mm) of the surface of a film of dried MFC with 6.12×10^{-1} mmol HMDA/g MFC, captured by laser profilometer.

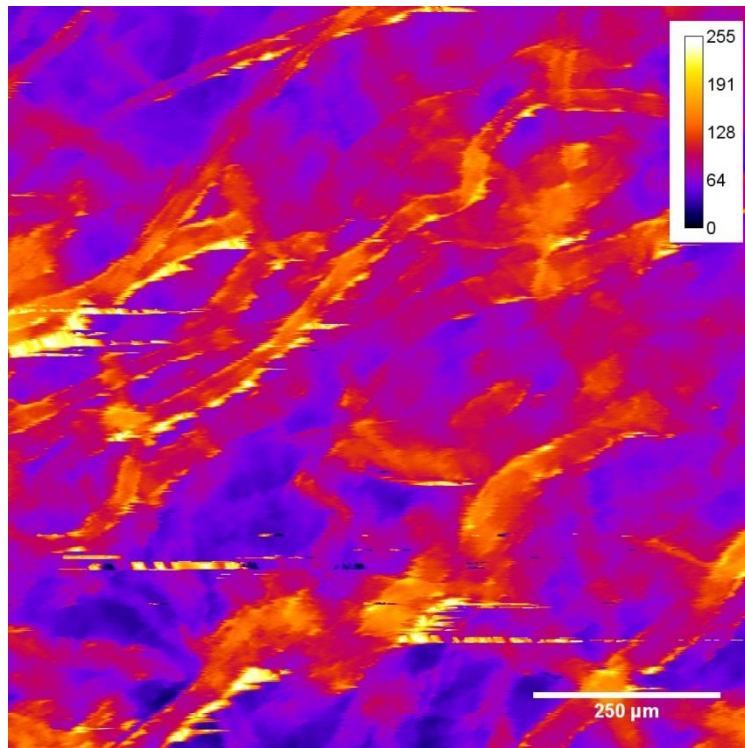


Figure E.4: Representative (Sq-value closet to average) topographic image (1 mm × 1mm) of the surface of a film of dried MFC with 3.05 mmol HMDA/g MFC, captured by laser profilometer.

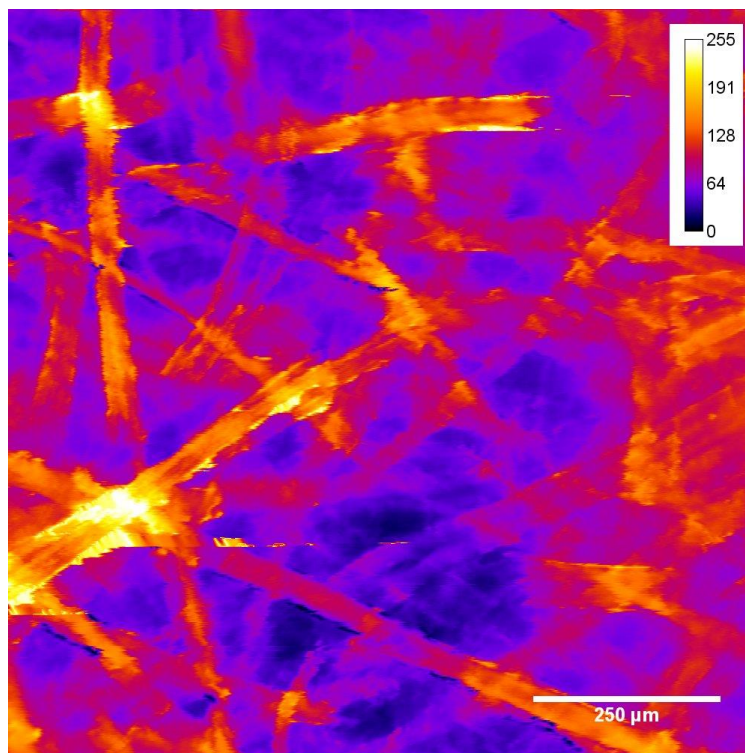


Figure E.5: Representative (Sq-value closet to average) topographic image (1 mm × 1mm) of the surface of a film of dried MFC with 6.14×10^{-2} mmol EDA/g MFC, captured by laser profilometer.

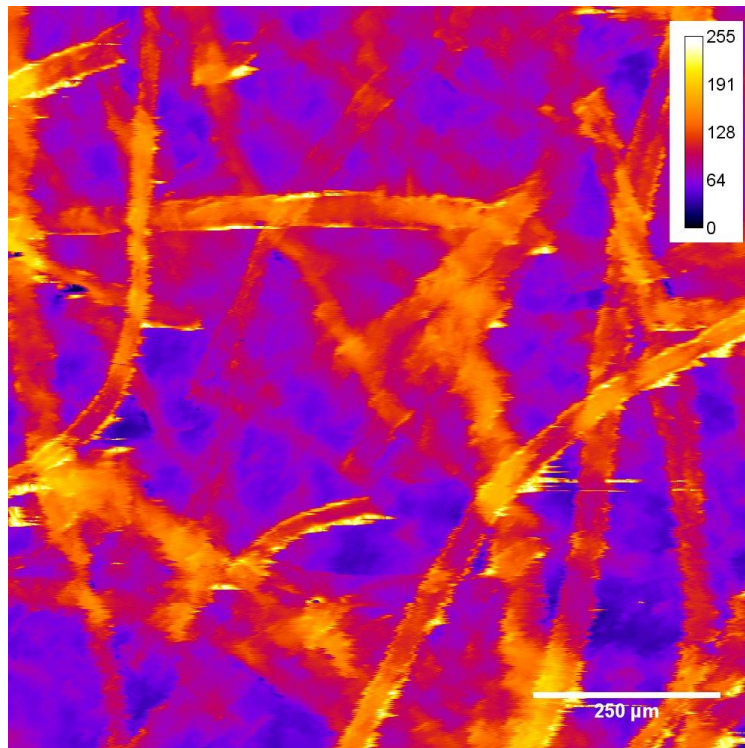


Figure E.6: Representative (Sq-value closet to average) topographic image (1 mm × 1mm) of the surface of a film of dried MFC with 6.08 mmol EDA/g MFC, captured by laser profilometer.

Appendix F: Representative atomic force microscopy images

Representative (i.e. with S_q values closest to the unfiltered S_q average values) three-dimensional (3D) renditions of topographic images captured by AFM can be seen in Figures F.1 – F.7. One such AFM image has a resolution of 2000×2000 nm and the image size of the captured images is 1024×1024 pixels. Since the laser profilometry images in Figures E.1 – E.6 has a resolution of 1000×1000 μm and a captured image size of 1000×1000 pixels, an area of only four pixels of the LP images equal the whole area of the AFM images. The representative image for the films with highest HMDA concentrations is shown in Figure 3.9.3.

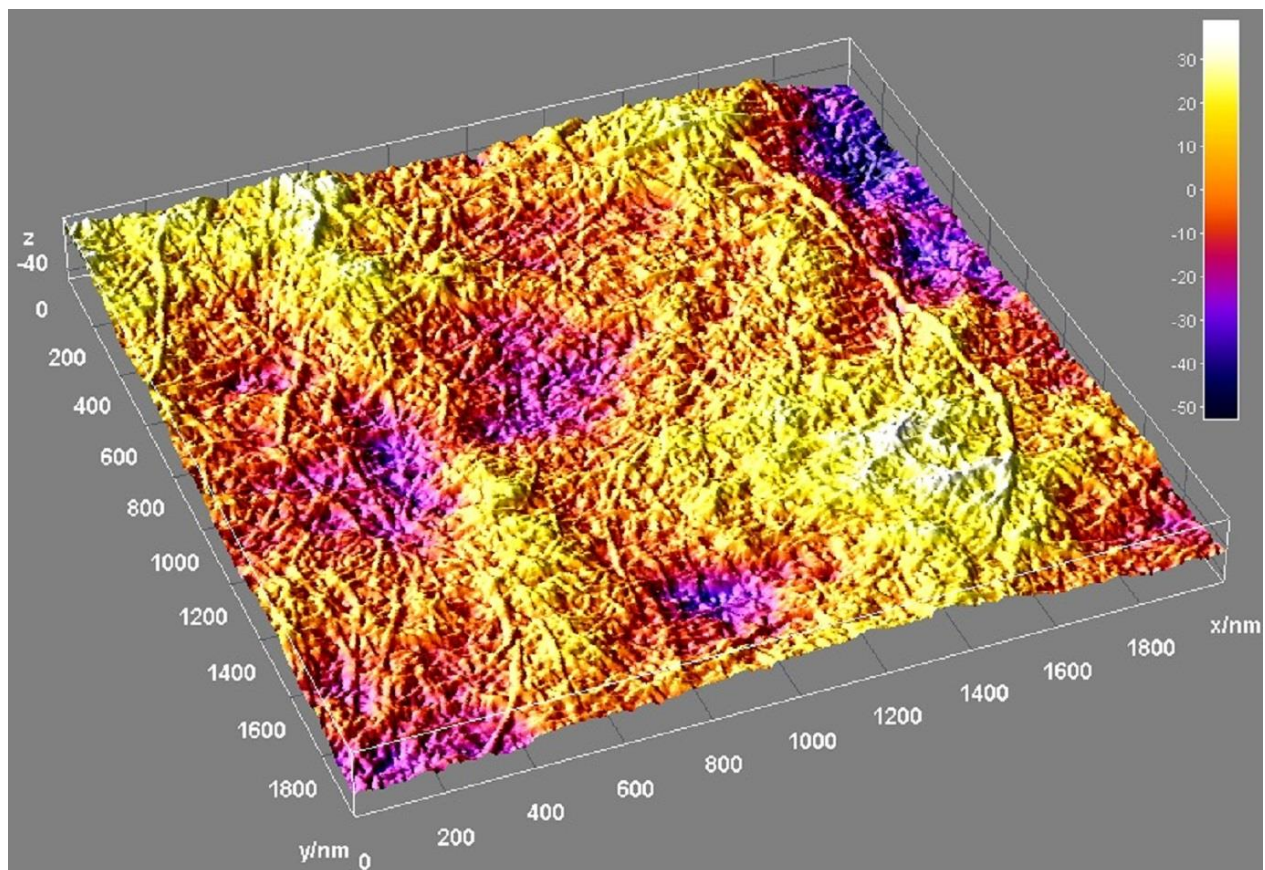


Figure F.1: 3D rendition of a topographic image ($2000 \text{ nm} \times 2000 \text{ nm}$) of the surface of a film of dried MFC with no crosslinkers, captured by atomic force microscopy, ScanAsyst Auto in air. The same image can be observed in Figure 3.9.2.

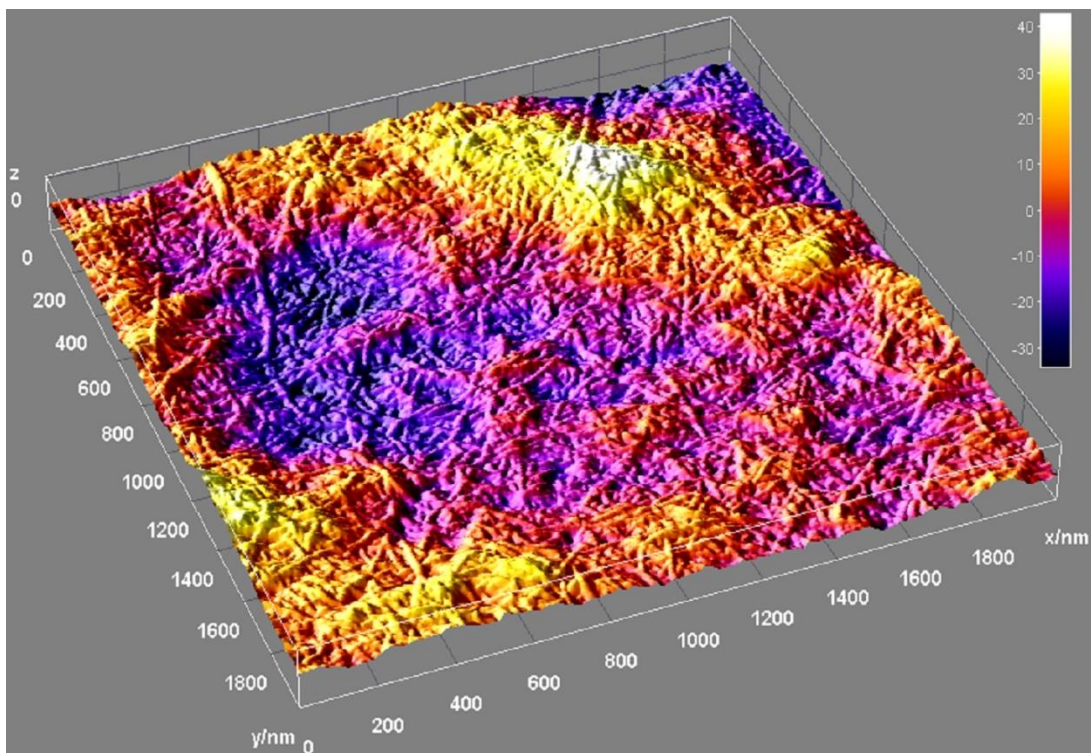


Figure F.2: 3D rendition of a topographic image (2000 nm × 2000 nm) of the surface of a film of dried MFC with HMDA (6.08×10^{-2} mmol/g MFC), captured by atomic force microscopy, ScanAsyst Auto in air.

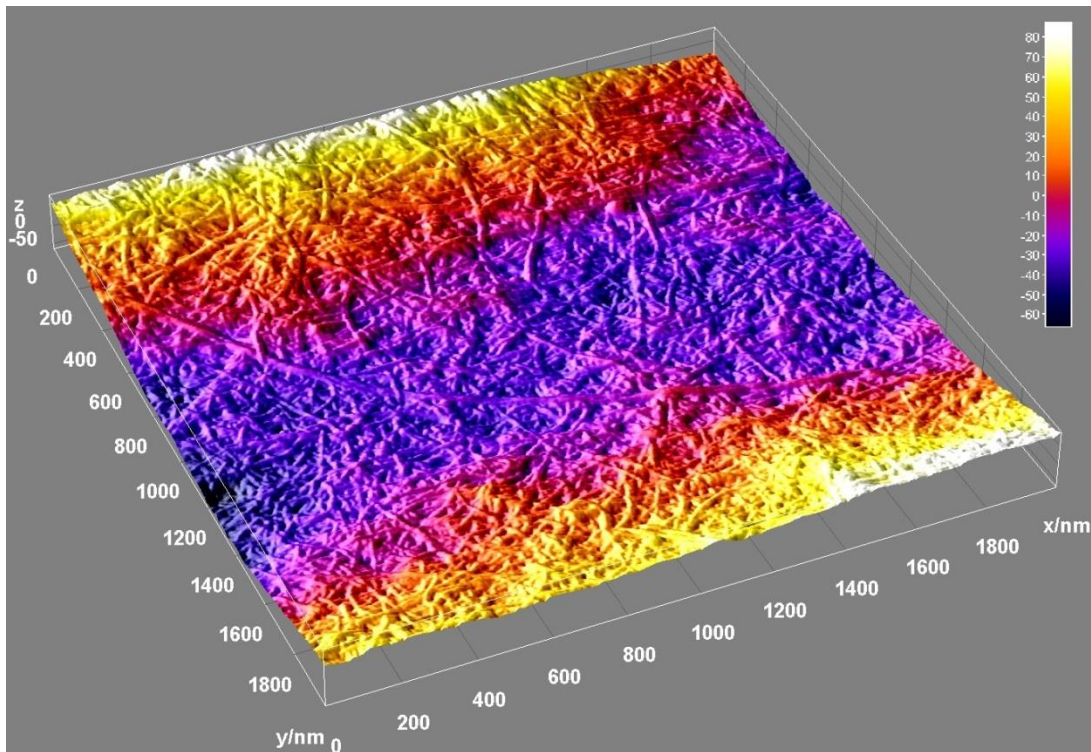


Figure F.3: 3D rendition of a topographic image (2000 nm × 2000 nm) of the surface of a film of dried MFC with HMDA (3.04×10^{-1} mmol/g MFC), captured by atomic force microscopy, ScanAsyst Auto in air.

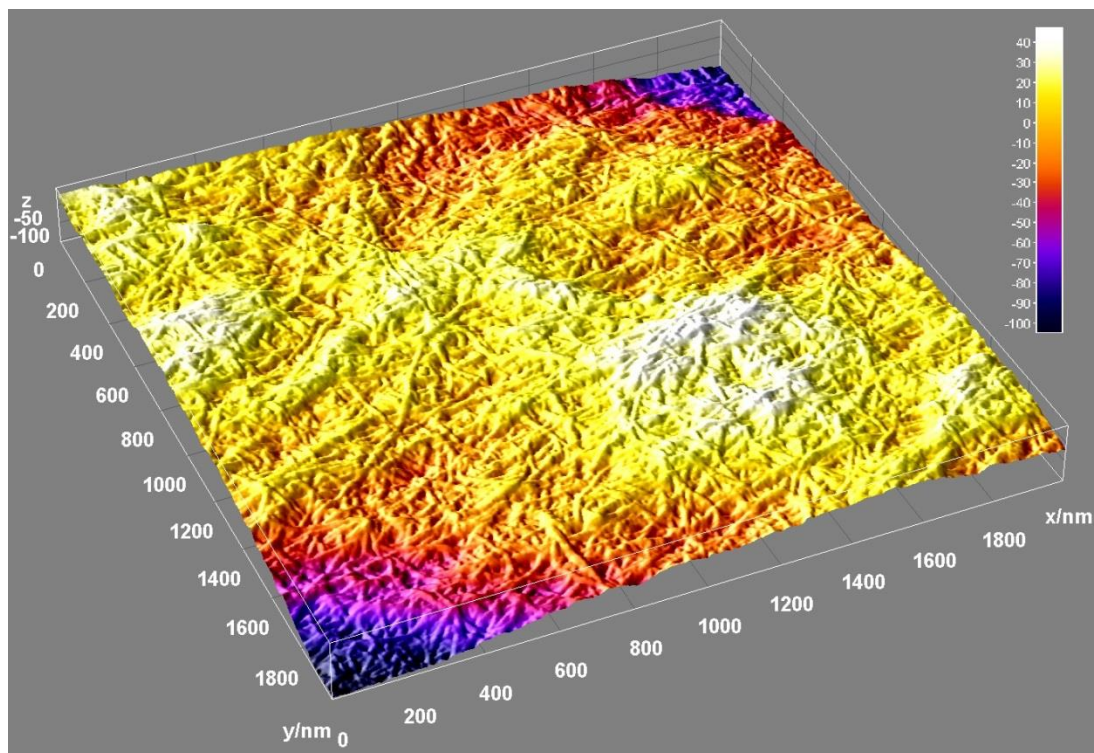


Figure F.4: 3D rendition of a topographic image (2000 nm × 2000 nm) of the surface of a film of dried MFC with HMDA (6.12×10^{-1} mmol/g MFC), captured by atomic force microscopy, ScanAsyst Auto in air.

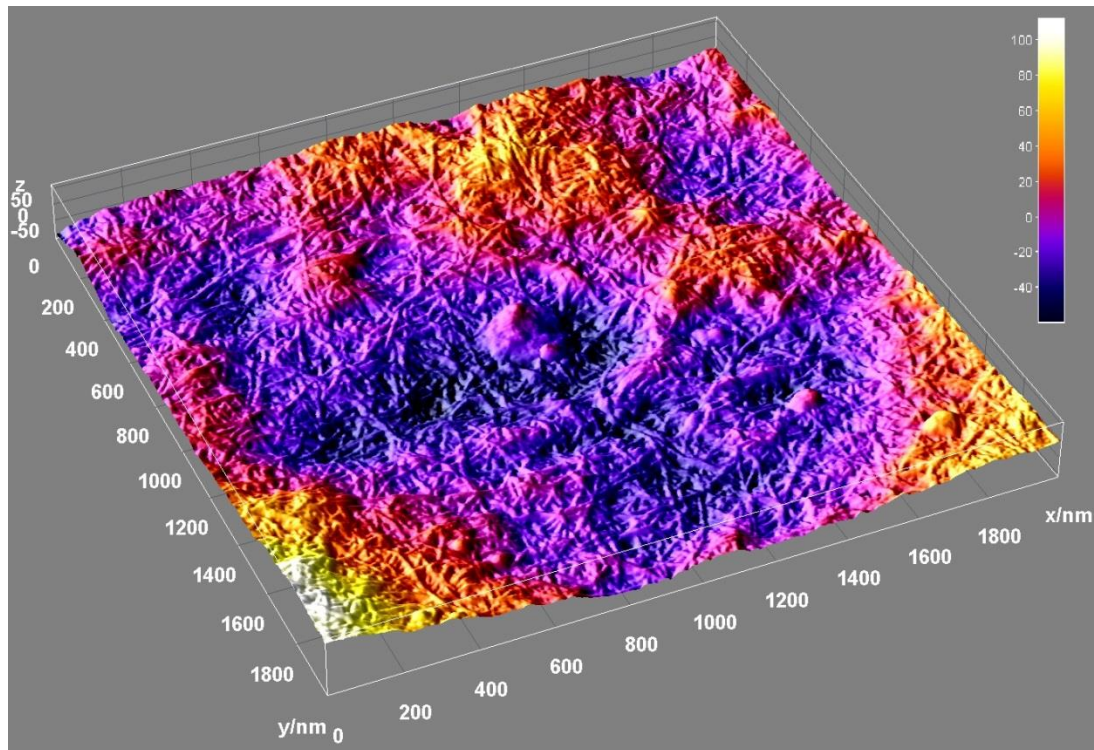


Figure F.5: 3D rendition of a topographic image (2000 nm × 2000 nm) of the surface of a film of dried MFC with HMDA (3.05 mmol/g MFC), captured by atomic force microscopy, ScanAsyst Auto in air.

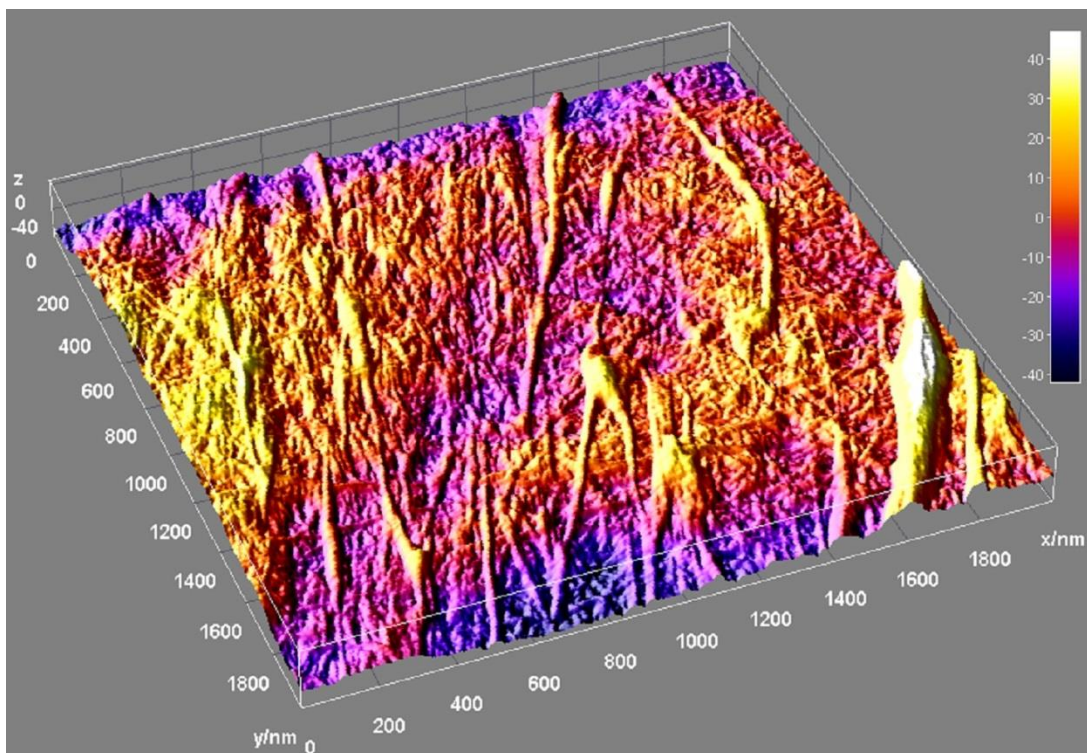


Figure F.6: 3D rendition of a topographic image (2000 nm × 2000 nm) of the surface of a film of dried MFC with EDA (6.14×10^{-2} mmol/g MFC), captured by atomic force microscopy, ScanAsyst Auto in air.

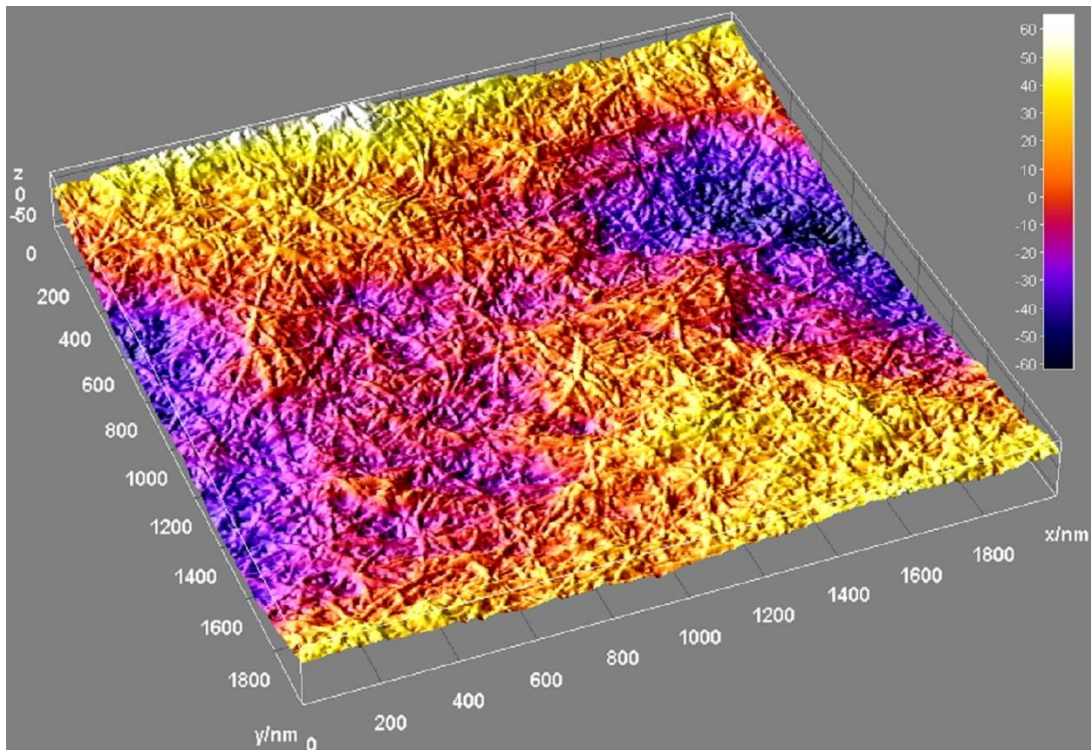


Figure F.7: 3D rendition of a topographic image (2000 nm × 2000 nm) of the surface of a film of dried MFC with EDA (3.04 mmol/g MFC), captured by atomic force microscopy, ScanAsyst Auto in air.

Appendix G: Numerical water absorption values

Table G.1: Numerical values for the weighed mass of the dried hydrogels prior ($t = 0$) and after the absorbance of water for the three first replicates of the E50, H50 and MFC freeze-dried gels. The moisture content (MC) and water absorption (Abs) were calculated from the dry mass of the samples at $t = 0$ and the wet mass of the sample by the equations found in Section 2.15.

First	E50			H50			MFC		
Time [min]	Mass [g]	MC [%]	Abs [%]	Mass [g]	MC [%]	Abs [%]	Mass [g]	MC [%]	Abs [%]
0	0.0427	0.00	0.00	0.0462	0.00	0.00	0.0406	0.00	0.00
15	2.1254	97.99	4877.52	1.7933	97.42	3781.60	3.076	98.68	7476.35
51	2.1044	97.97	4828.34	1.7482	97.36	3683.98	3.2322	98.74	7861.08
81	2.1353	98.00	4900.70	1.797	97.43	3789.61	3.3689	98.79	8197.78
138	1.9975	97.86	4577.99	1.7075	97.29	3595.89	3.4577	98.83	8416.50
183	2.0126	97.88	4613.35	1.5863	97.09	3333.55	3.532	98.85	8599.51

Table G.1: Numerical values for the weighed mass of the dried hydrogels prior ($t = 0$) and after the absorbance of water for the three second replicates of the E50, H50 and MFC freeze-dried gels. The moisture content (MC) and water absorption (Abs) were calculated from the dry mass of the samples at $t = 0$ and the wet mass of the sample by the equations found in Section 2.15.

Second	E50			H50			MFC		
Time [min]	Mass [g]	MC [%]	Abs [%]	Mass [g]	MC [%]	Abs [%]	Mass [g]	MC [%]	Abs [%]
0	0.0395	0.00	0.00	0.0461	0.00	0.00	0.0433	0.00	0.00
2	1.5812	97.50	3903.04	1.8938	97.57	4008.03	2.1381	97.97	4837.88
16	1.6465	97.60	4068.35	1.8530	97.51	3919.52	2.6024	98.34	5910.16
46	1.6778	97.65	4147.59	1.8506	97.51	3914.32	2.6531	98.37	6027.25
*46	1.6533	97.61	4085.57	1.7804	97.41	3762.04	2.6261	98.35	5964.90

*This last measurement was done after touching the surface for approximately 2 seconds using a filter paper, to investigate (roughly) how large margin of error was added when removing surplus water.